Investigating Novel Optical Fibres for More Advanced Distributed Optical Fibre Sensing

Malak Mohamed Hossameldeen Omar Mohamed GALAL

"I am among those who think that science has great beauty. A scientist in his laboratory is not only a technician: he is also a child placed before natural phenomena which impress him like a fairy tale."

— Marie Curie

To my one and only Khalid and my beloved family ♡

Acknowledgements

I would like to begin my acknowledgements by wholeheartedly thanking my thesis supervisor and mentor Prof. Luc Thévenaz for giving me the opportunity to conduct my PhD studies in his laboratory Group for Fibre Optics (GFO). It has definitely been an absolute pleasure working at GFO. Luc is very knowledgeable and I am very lucky to have had the chance to be his student and learn so much from him. He has always been an encouraging and a very patient mentor, who always appreciated spending quality time with his team. We have spent amazing times hiking, skiing, eating fondue and raclette, and explored hidden gems in Switzerland thanks to Luc. I am very thankful to him for making my PhD experience a memorable one.

Beside my appreciation to my advisor, I would also like to show my gratitude to the members of my thesis defence jury: the president of my jury Prof. Christophe Moser, and the experts of my jury Prof. Miguel González-Herráez, Prof. Radan Slavik, and Prof. Camille-Sophie Brès for kindly accepting to evaluate my thesis and for the time they devoted to review it.

The lab members of GFO were not merely my work colleagues, but they were and will always be very dear friends of mine. The time we spent together, whether at work or in external activities is indeed unforgettable. I would like to sincerely thank all the group members I met during my time at GFO: Tiago Neves, Zhisheng Yang, Fan Yang, Can Yao, Desmond Chow, Xu Cheng, Maria Isabel Alvarez, Ana Gabriela Correa, and all visiting scientists. A big thank you goes to our amazing lab secretary Svetlana Mashkina, who always helped me practice my French. I would also like to thank my colleagues from our neighbouring laboratory, Photonic Systems Laboratory (PHOSL) headed by Prof. Camille-Sophie Brès, for being great friends and for always being so kind in exchanging equipment with our laboratory.

Special thanks goes to the colleagues who were the closest to me during my time at GFO: Suneetha Sebastian, Li Zhang, Simon Zaslawski, Flavien Gyger, and Yuting Yang. Without their continuous help and support, my PhD experience wouldn't have been the same, and I am truly appreciative of having such wonderful people as my colleagues and dear friends. I learned a lot from their absolute kindness and selflessness. I am specifically grateful for working with Suneetha who helped me in every step in the way towards my degree.

I would like to also thank Simon's beautiful wife Aya Accogli for being a great friend and for teaching me how to ski. Very special thanks goes to my friends Helena Miljkovic and Wayne Yang for our fun and cheerful outings together and our awesome board game nights.

Reaching this stage of my life would have never been easy without the utmost support and care of my dear family and friends. I would like to deeply thank my dearest childhood friends Hana Shaltout and Christina Bibawi for being absolutely amazing friends and for always having my back. I would also like to express how grateful I am for having my husband's beautiful family and would like to thank them for their sheer kindness and their utmost care and support. My deepest gratitude and appreciation goes to my beloved parents and my awesome brothers along with their beautiful families. Only because I was lucky enough to have them all in my life, was I able to achieve my dreams and even go beyond what I have dreamed of.

Finally, I would like to express my utmost gratitude to my sweetheart and husband, Khalid Ibrahim, who has been totally and utterly supportive of me! I am extremely thankful for having him by my side at all times lifting me up every time I fall. My journey would have undoubtedly been way more difficult if it weren't for his unconditional love, care and support.

Lausanne, 25 May 2022   Malak Galal

Abstract

The ever-growing need for distributed optical fibre sensors (DOFS) in numerous fields and applications demands continuous research towards the advancement of the existing sensing systems. The convenience in the field of DOFS lies in the several degrees of freedom that it offers, such as the scattering mechanism, the interrogation technique, the medium for propagation, and the sensing fibre itself. Even though a vast amount of research is oriented towards the fabrication of novel fibres, in many cases the real benefit of such fibres is not really exploited. Therefore, in this thesis, we use and characterise multiple novel optical fibres with the aim of harnessing their full potential by understanding their ultimate strengths and limitations. To that effect, we perform efficient distributed optical fibre sensing by investigating different scattering mechanisms in different scattering media by means of several interrogation techniques. The thesis is divided into two groups of chapters depending on the type of scattering mechanism and medium.

In the first group of chapters, we work on the investigation of the most prominent scattering mechanism in silica-core single-mode optical fibres (SMFs), namely Rayleigh scattering. We interrogate a novel reflection-enhanced fibre (REF) based on fibre Bragg gratings using one of the most widely-utilised interrogation techniques for Rayleigh scattering, which is phase-sensitive optical time-domain reflectometry (φ-OTDR). So far, no theoretical expression has been presented to relate the most crucial parameters of Rayleigh-based sensing systems. We, therefore, develop a model, as a figure-of-merit for Rayleigh-based systems, addressing this concern, and we confirm it with experimental results. By performing a distributed temperature measurement as a form of comparison between the REF and an SMF, we yield a 6× lower experimental uncertainty for the REF when compared to the SMF, and this lower uncertainty is directly attributed to the 6× higher signal-to-noise ratio that the REF offers. The model as well as the guidelines for utilising REFs to maximum effect will aid the scientific community in better understanding Rayleigh-based sensing systems and employing them more efficiently.

The focus then shifts to the most prominent scattering mechanism in a gaseous medium of high density (at 1 atm for instance), namely Brillouin scattering. The analysis is carried out using several novel hollow-core optical fibres particularly anti-resonant fibres (HC-ARFs) which we fill with gas. We demonstrate for the first time to the best of our knowledge a Brillouin gain measurement in gas-filled HC-ARFs and highlight the square dependence of the

Brillouin gain on the gas pressure. We perform a comparison between three hollow-core fibres of different dimensions which we fill with two different gases, and we indicate the trade-offs in terms of Brillouin gain coefficients, gas filling times as well as gas pressure limitations. Additionally, we conduct for the first time to our knowledge a distributed temperature measurement using a gas-filled hollow-core conjoined-tube anti-resonant fibre (HC-CAF) and show a higher sensitivity to temperature change which is about 2× greater than the sensitivity of conventional silica fibres. The results indicate the great potential of gas-filled hollow-core fibres and pave the way for researchers to employ them as promising candidates for lasing, sensing and imaging applications.

iv

Résumé

La besoin toujours croissant de capteurs répartis à fibres optiques (CRFO) dans de nombreux domaines et applications implique que les systèmes de mesures existants soient constamment améliorés. Les différents paramètres techniques des CRFO, à savoir le mécanisme de diffusion, le milieu de propagation, la technique de mesure et la fibre elle-même sont autant de degrés de liberté qui rendent cette technologie polyvalente et attractive. Bien qu'un effort de recherche considérable soit investi dans la fabrication de fibres optiques innovantes, les avantages apportés par ces dernières ne sont pas toujours complètement exploités. Cette thèse est dédiée à l'utilisation et la caractérisation de diverses fibres optiques spéciales afin de déterminer leur potentiel mais aussi leurs limitations. Pour ce faire, nous effectuons un panel de mesures réparties, basées sur différents mécanismes de diffusion, dans plusieurs milieux de propagation et en utilisant différentes techniques d'interrogation. Cette thèse est divisée en deux parties, dépendamment du type de mécanisme de diffusion utilisé et du milieu de propagation employé.

La première partie est dédiée à l'étude du mécanisme de diffusion dominant dans les fibres monomodes en verre de silice (SMF), à savoir la diffusion Rayleigh. Nous mesurons une nouvelle fibre à réflexion augmentée (REF) grâce à l'inscription de réseaux de Bragg par réflectométrie optique sensible à la phase (φ-OTDR), une des techniques d'interrogations les plus répandues pour mesurer la diffusion Rayleigh. À ce jour, aucun modèle théorique permettant de relier les différents paramètres caractéristiques des système de mesure Rayleigh n'avait été présenté. Nous établissons donc de manière analytique, puis confirmé expérimentalement, un facteur de mérite pour les CRFO à diffusion Rayleigh. En réalisant une mesure répartie de température entre une SMF et une REF, nous pouvons établir une incertitude de mesure six fois inférieure pour la REF que pour la SMF, une réduction directement attribuée au rapport signal sur bruit six fois plus élevé dans la REF. Ce modèle ainsi que l'établissement de lignes directrices permettant d'exploiter les REF au maximum de leur potentiel profiteront certainement à la communauté scientifique dans la compréhension et l'optimisation des CRFO à diffusion Rayleigh.

Nous étudions ensuite le mécanisme de diffusion dominant dans les milieux gazeux à haute densité, à savoir la diffusion Brillouin. L'analyse est conduite dans plusieurs fibres à cœur creux que nous remplissons de gaz, notamment des fibres anti-résonantes (HC-ARFs). Nous démontrons, pour la première fois à notre connaissance, la mesure du gain Brillouin dans

une HC-ARF remplie de gaz, et soulignons également la dépendance quadratique du gain Brillouin en fonction de la pression du gaz. Nous comparons trois fibres à cœurs creux de dimensions différentes, remplies avec deux types de gaz, ce qui nous permet d'établir une série de compromis entre le coefficient de gain Brillouin, le temps de remplissage du gaz ainsi que la pression du gaz. De plus nous effectuons, pour la première fois à notre connaissance, une mesure de température répartie dans une fibre à cœur creux et tubes conjoints remplie de gaz, et démontrons une sensibilité à la température environ deux fois supérieure à celle d'une fibre conventionnelle en silice. Ces résultats démontrent le fort potentiel des fibres à cœur creux remplies de gaz pour diverses applications, tel que les lasers, les capteurs réparties et les applications d'imagerie.

Mots clés : Diffusion Rayleigh, fibres à réflexion renforcée, diffusion Brillouin, fibres à cœur creux remplies de gaz, mesure répartie de température

Contents

List of Figures

List of Tables

1 Introduction

Fibre optics: two simple words representing a breakthrough technology that has drastically changed the world ever since it was brought to existence in the last century [1, 2]. Almost everyone worldwide knows about optical fibre cables and how they have transformed data transmission and communications [3] and elevated them to a whole new level. A few decades back, it wouldn't have crossed anyone's mind that nowadays we will be in an extremely advanced internet era where we will be seamlessly communicating with each other across the globe; it is an absolute miracle indeed!

What is even more fascinating about optical fibres is the fact that they are not solely used for fibre-optic communications, but they interestingly act as a nervous system and sense a myriad of parameters (e.g. temperature, strain, etc.) in our surroundings [4]. This means that all optical fibres already installed for data communications all-over the world can also be adjusted to be used as distributed sensors and to give us localised information about their surroundings. A group of researchers at Google was able to utilise the traffic data of one of the global submarine cables to measure pressure and strain alterations, which enabled them to detect earthquakes and ocean waves called swells generated by storms [5]. Distributed optical fibre sensing is undoubtedly a powerful technology for the early detection and prevention of disastrous incidents.

The working principle of distributed optical fibre sensors relies simply on analysing the universal back-scattered light signal from the fibre; a signal which is inevitably present in all kinds of fibres. Detecting such back-scattering can be achieved utilising a wide range of advanced interrogation techniques. Depending on the type of application, the interrogation technique is selected and altered according to the need. Another degree of freedom when it comes to fibre sensing is the choice of optical fibre. There is a large variety of different optical fibres, and researchers are always seeking for more inventions and more developments in that regard. With the emerging technologies for optical fibre fabrication, a large-scale research is headed towards that direction.

This dissertation is a comprehensive study on the most prominent spontaneous light scattering

mechanisms present in different dielectric media of state-of-the-art optical fibres with the ultimate goal of employing them for efficient distributed temperature sensing. The choice of the scattering mechanism, the type of the optical fibre, along with the kind of the interrogation technique presented in this thesis solely depends on the specificity of the application. The work carried out in this thesis is divided into two large groups of chapters depending on which type of dielectric medium is chosen to investigate the corresponding most-prominent light scattering mechanism.

In the first group of chapters, consisting of chapters 3, 4 and 5, the focus is on investigating Rayleigh back-scattering from one of the novel silica-based single-mode optical fibres (SMFs). Such novel SMFs are commonly referred to as reflection-enhanced fibre (REF), as the principle of such fibres is to increase the backreflected signal. This type of fibres is based on adding one more step in the fabrication process when compared to the conventional SMF, namely imprinting fibre Bragg gratings inside the fibre. Rigorous investigation of this novel fibre has led to the development of a crucial relationship linking the fundamental system parameters of a Rayleigh-based distributed sensor that can be used as a figure-of-merit to evaluate the overall performance of such sensors. Using optimised experimental system parameters and benefiting from the enhanced backreflected signal of the REF, we showed a fully-distributed temperature measurement exhibiting sub-mK temperature uncertainty (~6× smaller than conventional silica fibres) with a metric spatial resolution.

Chapter 3 covers the realisation of a numerical spatio-temporal model developed to compare the most widely-utilised types of Bragg gratings. With the model we identify the most suitable types of gratings for distributed fibre sensing with backreflected signals significantly higher than the Rayleigh scattering floor.

Chapter 4 deals with the use of a backreflection-enhanced fibre along with a standard SMF for comparison, to present an analytical as well as a numerical theoretical model that relates the most vital parameters of Rayleigh-based sensing systems.

Chapter 5 presents a fully-distributed temperature measurement using the REF showing sub-mK temperature uncertainty with a metric spatial resolution. The experimental results were corroborated by the theoretical model presented in Chapter 4.

In the second group of chapters, consisting of chapters 6 and 7, we explore Brillouin light scattering from novel hollow-core anti-resonant optical fibres (HC-ARFs) filled with different gases at different pressures. Such novel fibres found their way in when the propagation loss of their counterparts, namely the hollow-core photonic-crystal bandgap fibres (HC-PCF) reached saturation [6] and could not be improved any further. Recent HC-ARFs, on the other hand, showed a loss as low as 0.174 dB/km in both C and L band [7] along with a wide transparent window. HC-PCF, nonetheless, have proven themselves to be suitable candidates for the investigation of light-matter interaction, non-linearity research which is useful for optical sensing, optical signal processing, high power lasers, etc. In spite of HC-ARFs combining the best of the two worlds (i.e. exhibiting the same advantages of HC-PCFs and having very

low propagation loss), the optical non-linearity of such fibres when filled with gas and their capabilities to be used for optical sensing have not been investigated before and are yet to be discovered. To that effect, we present for the first time a Brillouin gain measurement using such kind of fibres as well as an experimental demonstration of an efficient distributed temperature sensor. The proven square dependency of the Brillouin gain of the gas with its pressure, along with the choice of gas and the type of interrogation technique have helped achieving very accurate, highly sensitive and high spatial resolution strain insensitive temperature measurement with HC-ARFs having total loss comparable with standard silica fibres. The results indicate that this novel technology can be regarded as a competitive solution when compared to already-existent platforms in terms complexity and versatility.

Chapter 6 explains, through numerical simulation, the effectiveness of the coupling between the fundamental optical mode and the generated acoustic modes in a gaseous medium. With the information about the acousto-optic overlap, a theoretical estimation of the Brillouin gain is achieved.

Chapter 7 presents an experimental demonstration of the Brillouin gain measurement in HC-ARFs and shows how HC-ARFs can be utilised to perform highly-accurate fully-distributed temperature measurement with a high temperature sensitivity and a rather simple experimental setup.

2 Background and fundamentals

In this chapter we study the background and fundamental features of distributed optical fibre sensing (DOFS); a technology that is indeed of stupendous development and that has been intensively employed over the past 50 years. When we say "optical", we immediately find ourselves landing at the core of light theory or more precisely electromagnetic theory, namely the Maxwell's formalism. This is where we begin and from where we delve into the deeper understanding of wave propagation —a topic that lies at the centre of literally everything when dealing with optical fibres. We further discuss the different types of scatterings that may affect a propagating light wave whether in solid or gaseous media. Some fundamental thermodynamics will be also studied to form a strong basis before analysing scatterings in gases. A final section is then dedicated to provide insightful aspects related to the different types of interrogation systems required to perform distributed optical fibre sensing.

2.1 Maxwell's equations

A long time back, in the 19th century to be exact, James Clerk Maxwell presented the first version of the relationships of electricity and magnetism grouped together into the well-known set of equations nowadays referred to as Maxwell's equations. Before the realisation of Maxwell's equations, the theory of light was regarded as a separate topic not belonging to the classical electromagnetic phenomena. However, when the connection was established, it was immediately clear that thanks to Maxwell's equations, which are at the heart of all theoretical principles of optics, our deep and elaborate understanding of light is shaped. The general

formulation of the equations is presented as follows [8–11]:

$$\overrightarrow{\nabla} \times \overrightarrow{E} = -\frac{\partial \overrightarrow{B}}{\partial t} \qquad \text{Faraday's Law} \qquad (2.1)$$

$$\overrightarrow{\nabla} \times \overrightarrow{H} = \frac{\partial \overrightarrow{D}}{\partial t} + \overrightarrow{J} \qquad \text{Ampère's Law} \qquad (2.2)$$

$$\overrightarrow{\nabla} \cdot \overrightarrow{D} = \rho \qquad \text{Gauss' Law} \qquad (2.3)$$

$$\overrightarrow{\nabla} \cdot \overrightarrow{B} = 0 \qquad \text{Gauss' Magnetism Law} \qquad (2.4)$$

where $\overrightarrow{E}$ and $\overrightarrow{H}$ are the electric field and the magnetic field, respectively, and they represent the two components of the electromagnetic field. The charge density ρ denotes the free charges per volume and the current density $\overrightarrow{J}$ describes the motion of charge density. $\overrightarrow{D}$ and $\overrightarrow{B}$ are the electric flux density and the magnetic flux density, respectively, and can be elaborated by the following constitutive relations:

$$\overrightarrow{D} = \epsilon_0 \overrightarrow{E} + \overrightarrow{P} \qquad (2.5)$$

$$\overrightarrow{B} = \mu_0 \overrightarrow{H} + \overrightarrow{M} \qquad (2.6)$$

where ϵ_0 is the electric permittivity in vacuum, $\overrightarrow{P}$ is the induced electric polarisation field, μ_0 is the magnetic permeability in vacuum, and $\overrightarrow{M}$ is the magnetisation field.

2.1.1 Wave equation

By performing substitutions and simplifications to equations (2.1)-(2.6), we find ourselves reaching the fundamental expression which governs light wave propagation in a medium, namely [12]:

$$\overrightarrow{\nabla}^2 \overrightarrow{E} - \frac{1}{c^2} \frac{\partial^2 \overrightarrow{E}}{\partial t^2} = \mu_0 \frac{\partial \overrightarrow{J}}{\partial t^2} + \mu_0 \frac{\partial^2 \overrightarrow{P}}{\partial t^2} - \frac{1}{\epsilon_0} \nabla(\nabla \cdot \overrightarrow{P}) \qquad (2.7)$$

where $c = \frac{1}{\sqrt{\epsilon_0 \mu_0}} \approx 3 \times 10^8$ m/s is the speed of light in vacuum. Eq. 2.7 when equated to zero, gives us the familiar wave equation in vacuum:

$$\overrightarrow{\nabla}^2 \overrightarrow{E} - \frac{1}{c^2} \frac{\partial^2 \overrightarrow{E}}{\partial t^2} = 0 \qquad (2.8)$$

However, when dealing with light propagation in a medium, we have to consider the effect of the source terms found on the right-hand side of Eq. 2.7 because at least one of those terms will be non-zero. The first term on the right-hand side can be of interest when dealing with propagation of light in a plasma for example. The second term presents dipole oscillations taking place when light propagates through a non-conductive isotropic material such as glass. In this case, the polarisation field is generated along the electric field and is proportional to it

as follow:

$$\overrightarrow{P} = \epsilon_0 \chi \overrightarrow{E} \tag{2.9}$$

where χ is the electric susceptibility. However, in the last term on the right-hand side of Eq. 2.7 which accounts for light propagation through anisotropic media like crystals for instance, the polarisation field may not necessarily be along a direction that is parallel to the electric field and cannot be described by Eq. 2.9. Only the second term is of relevance to us in this thesis as we deal with silica optical fibres. Accordingly, Eq. 2.7 simplifies to:

$$\overrightarrow{\nabla}^2 \overrightarrow{E} - \frac{1}{c^2} \frac{\partial^2 \overrightarrow{E}}{\partial t^2} = \mu_0 \frac{\partial^2 \overrightarrow{P}}{\partial t^2} \tag{2.10}$$

By substituting the expression for the polarisation term expressed by Eq. 2.9 in Eq. 2.10, we end up with:

$$\overrightarrow{\nabla}^2 \overrightarrow{E} - \frac{n^2}{c^2} \frac{\partial^2 \overrightarrow{E}}{\partial t^2} = 0 \tag{2.11}$$

where n is the medium refractive index and is defined as:

$$n = \sqrt{\epsilon_r} = \sqrt{1 + \chi} \tag{2.12}$$

where the expression $\epsilon_r = n^2$ is called the Maxwell relation with ϵ_r as the relative permittivity. The absolute permittivity ϵ of a material is given as a function of ϵ_r and ϵ_0 as follows: $\epsilon = \epsilon_r \epsilon_0$. Solutions to Eq. 2.11 are monochromatic plane waves represented by:

$$\overrightarrow{E}(\overrightarrow{r}, t) = \overrightarrow{E_0}(x, y, z)\, e^{i(\pm \overrightarrow{k_{\mathrm{in}}} \cdot \overrightarrow{r} + \omega t)} \qquad \text{Multi-dimensional System} \tag{2.13}$$

$$\overrightarrow{E}(z, t) = \overrightarrow{E_0}(x, y)\, e^{i(\pm k_{\mathrm{in}} z + \omega t)} \qquad \text{One-dimensional System} \tag{2.14}$$

where $\overrightarrow{E_0}$ is the complex amplitude and the physical field is the real part of $\overrightarrow{E}$, $\overrightarrow{k_{\mathrm{in}}}$ is the propagation wavevector of the incident light, and ω is the angular frequency, and they fulfil the dispersion relation as follows:

$$k_{\mathrm{in}} = \left| \overrightarrow{k_{\mathrm{in}}} \right| = \sqrt{\epsilon_0} \frac{\omega}{c_0} = n \frac{\omega}{c_0} = \frac{2\pi n}{\lambda_0} \tag{2.15}$$

where k_{in} is the wavenumber and represents the magnitude of the wavevector $\overrightarrow{k_{\mathrm{in}}}$.

It should be noted that the vector dot product $\overrightarrow{k_{\mathrm{in}}} \cdot \overrightarrow{r}$ in Eq. 2.14 represents the wavevector and the position vector in a multi-dimensional system. However, in our case, we deal with a one-dimensional system where the direction of the wave is along the z-direction only, and is therefore represented by the scalar $k_{\mathrm{in}} z$.

Eq. 2.14 is a solution of the wave equation that describes the propagation of plane waves and will be further utilised in this thesis whenever the propagation or coupling between waves in

one-dimensional systems (e.g. optical fibres) is presented. In the coming sections, we will introduce how the propagating light waves get scattered in the different media and thoroughly explain the phenomena/mechanisms behind the scattering.

2.2 Light scattering in solid media

When a light wave propagates through a transparent medium, some of it gets transmitted, and a portion of it gets scattered. Depending on the type of waveguide and the scattering mechanism that takes place, light can just be lost or get backreflected and recollected at a receiving end. If we consider a solid medium, like an optical fibre for example, the light will be propagating and guided by total internal reflection within in its solid silica core. In this case, the light may either experience one or multiple of the different fibre-inherent inevitable scattering processes like Rayleigh, Brillouin, and Raman scattering, or it may be back-scattered by purposefully-engineered density fluctuations within the medium like what is called a fibre Bragg grating (FBG). In this section, we will introduce the different causes of scattering in a solid medium with a focus on optical fibres given that this is the main topic in this thesis. We will also briefly discuss how the scattering of light can be utilised to identify changes in parameters like temperature or strain affecting the medium where the scattering occurs, which, in our case as already mentioned, will be an optical fibre with a solid silica core.

For a relatively long time, optical fibres were merely regarded as waveguides for long-haul data transmission and communications applications. In fact, researches were actively searching
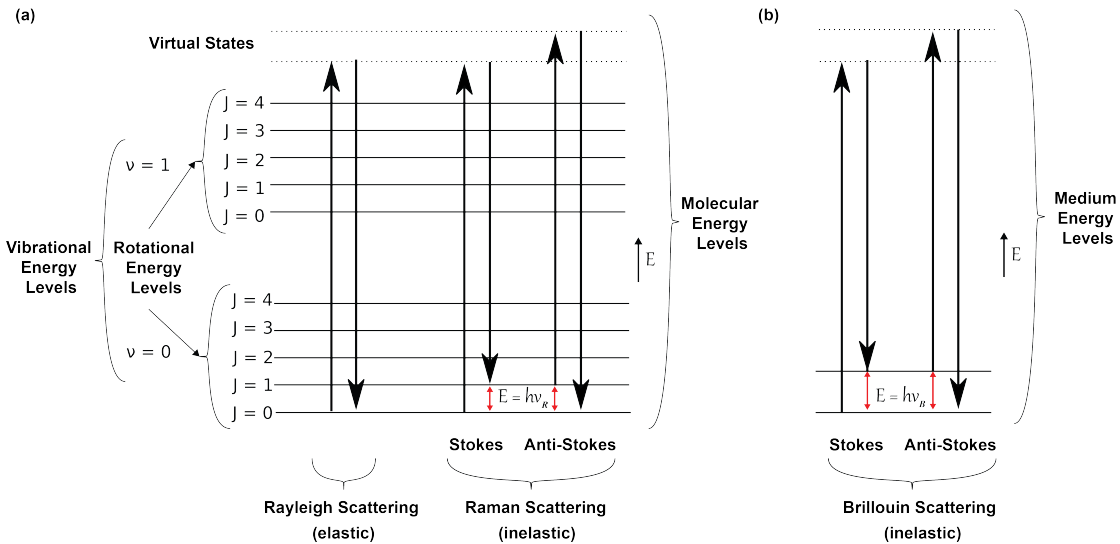
Figure 2.1 – Energy level diagram showing examples of light-matter interactions of any arbitrary medium (e.g. silica optical fibre); (a) Rayleigh elastic scattering and Raman inelastic scattering represented on the molecular energy levels, and (b) Brillouin inelastic scattering represented on the energy levels of the entire medium; figure adapted from [13]. Note: The spacing between the energy levels is not to scale.

for solutions to minimise all possible fibre losses. Little did they know that some of these inevitable losses can result in the birth of a whole new field, namely fully-distributed optical fibre sensing.

When light is launched into an optical fibre, it is affected by the different optomechanical and thermodynamic properties of the fibre resulting in the back-scattering of a small portion of the incident light. The three main scattering processes taking place in a silica optical fibre are Rayleigh, Raman, and Brillouin scattering. The diagram representing the quantum energy transitions for the different scattering processes is depicted in Fig. 2.1. An energy level transition (described by the vertical arrows in Fig. 2.1) may be triggered when an incident photon possesses the same energy as that of the difference between two energy levels. Transitions to lower energy levels (downwards) result in the generation of another photon, whereas transitions to higher energy levels (upwards) result in the absorption of the photon. The solid horizontal lines shown in Fig. 2.1 are the physical energy levels of the system and the dotted horizontal lines correspond to virtual states. The symbol ν in this figure stands for the vibrational quantum number and J refers to the rotational quantum number. It should be noted, however, that ν_R and ν_B are the frequencies of an optical phonon involved in Raman scattering and an acoustic phonon involved in Brillouin scattering, respectively.

From the figure, it is clear that Rayleigh scattering is an elastic process while Raman and Brillouin scattering are inelastic processes. This means that in the case of Rayleigh scattering, no frequency shift occurs, and thus a downward transition will yield an identical photon of the same frequency as that of the incident one. However, for the inelastic Raman and Brillouin scattering processes, the photon experiences a frequency shift that is exactly equal to the generated/annihilated phonons; optical phonon having an energy of $E = h\nu_R$ in the case of
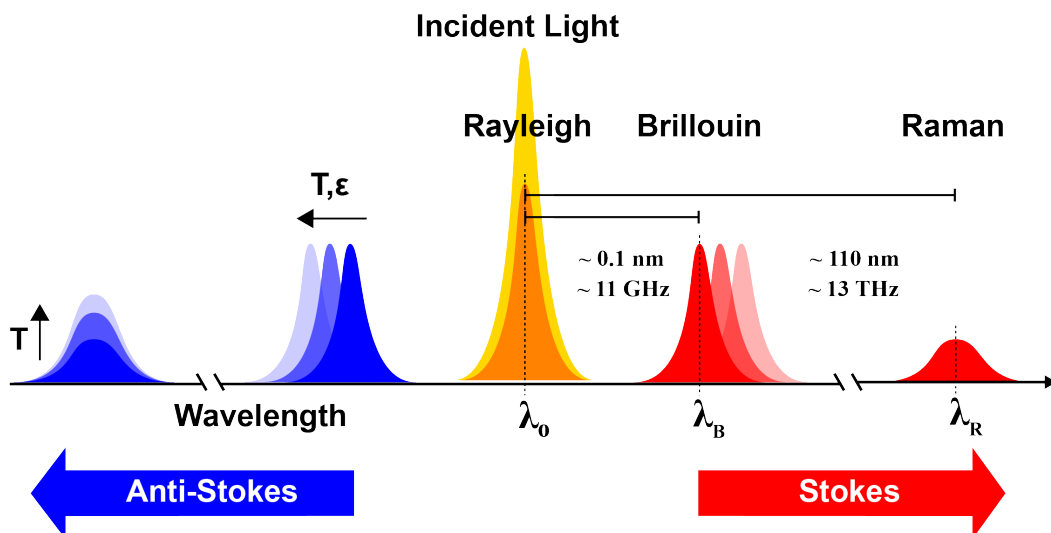
Figure 2.2 – The three fundamental scattering processes occurring in silica optical fibres when the wavelength of the incident light is at 1550 nm.

Scattering Process	Scattering Coefficient	Frequency Shift
Rayleigh	~-73 dB m^{-1}	No shift
Spontaneous Brillouin	~-90 dB m^{-1}	~ 0.1 nm (~ 11 GHz)
Spontaneous Raman	~-110 dB m^{-1}	~ 110 nm (~ 13 THz)

Table 2.1 – Typical values for the scattering coefficients and frequency shift for the three fundamental scattering processes for a standard silica SMF at a wavelength of 1550 nm.

Raman scattering, and acoustic phonon with an energy of $E = h\nu_B$ in the case of Brillouin scattering, where h is Planck's constant ($\sim 6.626 \times 10^{-34} \text{m}^2$ kg/s).

A visual representation of the three scattering processes is illustrated in Fig. 2.2. As observed, the yellow spectral distribution belongs to the incident light, the orange to the Rayleigh scattered light, the red is used for the Raman and Brillouin Stokes components, and the blue for the anti-Stokes components. For a typical standard silica optical fibre at a wavelength of 1550 nm, the scattering coefficients and the frequency shifts for the different scattering processes take the values presented in Table 2.1.

2.2.1 Rayleigh scattering

One interesting reality about Rayleigh scattering that should be known to everyone is the fact that Rayleigh scattering is the very reason behind why we see the colour of the sky as blue. Simply put, as the white sunlight travels through space and reaches Earth's atmosphere, it gets scattered by the molecules and particles filling the air that are of much smaller size compared to the radiation wavelength. Shorter wavelengths corresponding to the colours blue and violet [I] of the visible spectrum are the ones that scatter the most.

Scattering in a medium occurs due to the presence of local perturbations which cause the alteration of its optical properties. We, therefore, go back to Eq. 2.5 of the constitutive relations of the Maxwell's equations to describe the scattering processes using the dielectric tensor ϵ, which is an elemental parameter that describes how the medium will respond to an incoming electromagnetic field [14]. We, therefore and only for convenience, repeat Eq. 2.5 as follows:

$$\vec{D} = \epsilon \vec{E} = \epsilon_0 \vec{E} + \vec{P} \tag{2.16}$$

where the response of the medium is defined by the polarisation vector $\vec{P}$ described by Eq. 2.9 relating the polarisation field to the electric field through the electric susceptibility tensor χ. The dielectric tensor ϵ can be written as a function of the susceptibility tensor and the dielectric constant in vacuum using the following expression:

$$\epsilon = \epsilon_0(I + \chi) = \bar{\epsilon}I + \Delta\epsilon \tag{2.17}$$

[I]Despite the fact that the colour violet has a shorter wavelength than the colour blue, we perceive the sky to be blue-coloured. This is simply because violet is more absorbed in the higher atmosphere and less of it reaches Earth, and our eye receptors are more sensitive to the colour blue than violet.

where I is the identity matrix, $\bar{\epsilon}$ is the mean dielectric constant in the medium that represents the homogeneous contribution to the dielectric tensor and does not contain any information about lateral scattering, whereas $\Delta\epsilon$ describes the temporal and/or spatial fluctuations in the dielectric tensor which result in the scattering of light. The $\Delta\epsilon$ fluctuation term can be divided into its scalar and tensor contributions as follows:

$$\Delta\epsilon = \Delta\epsilon^s I + \Delta\epsilon^t \tag{2.18}$$

The first term $\Delta\epsilon^s$ represents fluctuations in the thermodynamic quantities such as pressure, density, temperature, and entropy, and results in scalar light scattering like Rayleigh and Brillouin scatterings. However, scattering arising from the second term $\Delta\epsilon^t$ is called tensor light scattering and causes the existence of scatterings like Raman and Rayleigh-wing scatterings.

At this stage we would like to calculate the intensity of the Rayleigh scattered light. We, therefore, have to recall 2.13, and hence present, using complex representation, the electric field of an optical plane wave which is incident on the medium:

$$\overrightarrow{E_{sc}}(\overrightarrow{R}, t) = E_{in}\overrightarrow{e_{in}}e^{j(\overrightarrow{k_{in}}\overrightarrow{R} - \omega t)} \tag{2.19}$$

where E_{in} is the incident field amplitude, $\overrightarrow{e_{in}}$ is the unit vector aligned with the light polarisation state (assuming a linear polarisation of the incident light), $\overrightarrow{k_{in}}$ is the propagation wavevector, R is the position of interest in the xyz coordinate system, and ω is the angular frequency. As illustrated in Fig. 2.3, the scattered field generated by a volume V of the medium at a position P which is far from the scattering volume (large $\overrightarrow{R}$, far-field approximation) is given by [14]:

$$\overrightarrow{E_{sc}}(\overrightarrow{R}, t) = E_{in}\frac{\omega^2}{c^2}[\overrightarrow{e_{sc}} \times (\overrightarrow{e_{sc}} \times \overrightarrow{e_{in}})]\frac{e^{j(k_{sc}R - \omega t)}}{4\pi R}\frac{1}{\epsilon_0}\int_V \Delta\epsilon(r', t)e^{j(\overrightarrow{k_{in}} - \overrightarrow{k_{sc}})\overrightarrow{r'}}d\overrightarrow{r'} \tag{2.20}$$

where $R = |\overrightarrow{R}|$ and $k_{sc} = |\overrightarrow{k_{sc}}|$, where $\overrightarrow{k_{sc}}$ is the propagation vector in the direction of the scattered wave and $\overrightarrow{e_{sc}}$ is the unit vector which aligns with the direction of $\overrightarrow{k_{sc}}$.

To calculate the scattered intensity, we then take the time-averaged value of $\overrightarrow{E_{sc}}\overrightarrow{E_{sc}}^*$, and it will be given as follows:

$$I_s = \langle\overrightarrow{E_{sc}}\overrightarrow{E_{sc}}^*\rangle \tag{2.21}$$

By substituting Eq. 2.20 into Eq. 2.21, we get the following expression [15]:

$$I_s = I_{in}\frac{\omega^4}{c^4}\frac{\sin^2\varphi}{\epsilon_0^2(4\pi R)^2}\int_V\int_V \langle\Delta\epsilon(\overrightarrow{r_1'}, t)\Delta\epsilon(\overrightarrow{r_2'}, t)\rangle e^{j[\overrightarrow{k_{in}} - \overrightarrow{k_{sc}})(\overrightarrow{r_1'} - \overrightarrow{r_2'})]}d\overrightarrow{r_1'}d\overrightarrow{r_2'} \tag{2.22}$$

where I_{in} is the intensity of the incident light, φ is the angle between the incident light field direction $\overrightarrow{e_{in}}$ and the propagation vector $\overrightarrow{k_{sc}}$ in the direction of the scattered wave. We shall notice that with the far-field approximation, when φ is equal to zero, the scattering intensity will also be zero, which means that no scattering can occur towards the X direction.
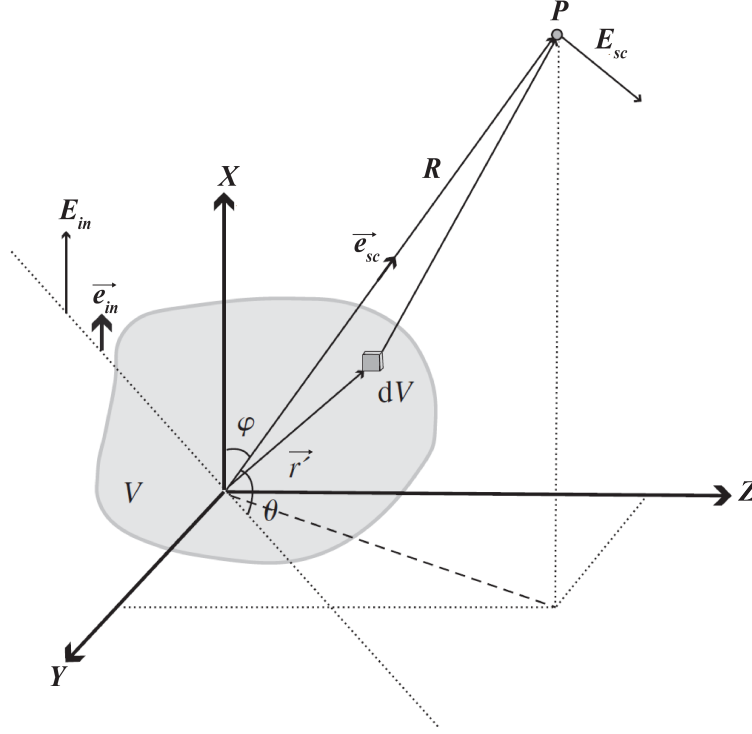
Figure 2.3 – Schematic showing the coordinate system to calculate the electric field E_{sc} of the Rayleigh scattered light [14].

Since the scatterers under consideration are assumed to be much smaller than the wavelength, the phase component of the integral can be approximated to be 1 ($\left|\vec{r_1'} - \vec{r_2'}\right|$ is small compared to the wavelength) and $\Delta\epsilon$ can be assumed to be constant within the volume V. The scattered intensity emitted by the volume V simplifies to:

$$I_s = I_{\text{in}} \frac{\omega^4 V^2 \sin^2\varphi}{16\pi^2 R^2 c^4} \frac{\langle \Delta\epsilon^2 \rangle}{\epsilon_0^2} \tag{2.23}$$

The strongest scattering happening in a silica optical fibre is Rayleigh scattering. It is caused by the density fluctuations or inhomogeneities, shown in Fig. 2.4, existent inside the core of an optical fibre, which are inevitably created during the drawing process of the fibre specifically because glass is amorphous in nature. Rayleigh scattering has been a fundamental limitation of fibre communications and contributes largely to the known loss value of a silica optical fibre at 1550 nm, namely ~0.2 dB/km which is about $4.5 \times 10^{-5} \text{m}^{-1}$. Despite it being a detrimental loss when it comes to data transmission, it carries useful localised information about the fibre surroundings and allows us to conduct optical fibre sensing that is distributed all along the fibre. As apparent from Fig. 2.4, Rayleigh scattering is a process which results in the light being scattered in many directions. A fraction of this scattered light which is about -73 dB/m gets backreflected and recaptured [16]. Important information about the fibre surroundings can be directly retrieved using a number of interrogation techniques. Typically-utilised Rayleigh-
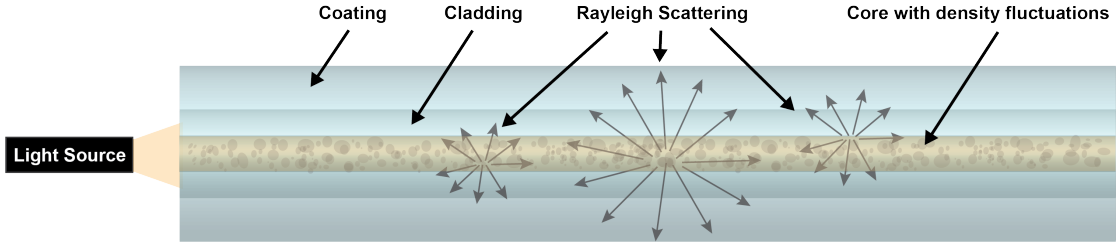
Figure 2.4 – Illustration showing all the layers of a standard single-mode fibre. Light is launched into fibre and gets scattered in all directions by the frozen core density fluctuations. This type of scattering is called Rayleigh scattering. Note: The illustration is not to scale.

based interrogation techniques are highly sensitive to environmental changes. In fact, such sensing techniques are significantly more sensitive than sensing techniques based on other scattering processes such as Brillouin scattering which is 1000× less sensitive than Rayleigh scattering. The sensitivity of coherent Rayleigh-based systems like phase-sensitive optical time-domain reflectometry (φ-OTDR) can be better understood by the following equation:

$$\varphi_o = \frac{2\pi\nu n(\epsilon, T)z}{c} \tag{2.24}$$

where φ_o is the phase of an optical signal, at a given frequency ν, and varies according to the distance z. As shown in the equation, the refractive index n is a function of strain (ϵ) and temperature (T). In practice, temperature changes (ΔT) mainly affect the refractive index n, whereas strain changes ($\Delta\epsilon$) cause the fibre to experience elongation/contraction, and have accordingly a much larger contribution on the propagated distance z. Several φ-OTDR systems are based on scanning the frequency of the interrogating light source which, as seen from (2.24), can compensate for variations in the phase φ_o resulting from strain and/or temperature changes. The sensitivity of φ-OTDR systems is thus usually defined as the ratio between the amplitude of the frequency change $\Delta\nu$ needed to compensate for one degree temperature change ΔT or one micro-strain $\mu\epsilon$. The temperature (T)/strain (ϵ) sensitivities for a conventional SMF at a wavelength of ~1550 nm are typically given as follows:

$$\frac{\Delta\nu}{\Delta T} \approx 1.3 \text{ GHz/K} \qquad\qquad \frac{\Delta\nu}{\Delta\mu\epsilon} \approx 152.4 \text{ MHz/}\mu\epsilon$$

More details about some interrogation systems utilised for the acquisition of the backreflected signal will be presented in section 2.4.

2.2.2 Brillouin scattering

Other types of scatterings occurring in a solid medium are spontaneous Brillouin and Raman scatterings. Brillouin scattering is an inelastic scattering process that occurs in different media like silica bulks such as in a silica optical fibre or fluids or plasma, for example. It was firstly

discovered independently by the French physicist Léon Nicolas Brillouin in 1922 and the Russian physicist Leonid Mandelstam in 1926.

In contrast to Raman scattering (see section 2.2.3) where the light interaction is with the fast vibrational oscillation (optical phonons with high energy and low momentum) of individual molecules inside the molecular chain, Brillouin scattering describes the light interaction with the slow oscillation of the entire molecular chain (acoustic phonons with low energy and high momentum) where there is mode-coupling and energy transfer between the optical and the vibrational modes of the entire medium [14]. This process is illustrated in Fig. 2.1 to highlight that for Brillouin scattering the interaction is with the whole medium and not with individual molecules, differently from Rayleigh and Raman scattering.

In general, the average number of phonons involved in spontaneous inelastic scatterings can be estimated using the Bose-Einstein statistics as described by the following equations [14, 17]:

$$\langle n_{AS} \rangle = \frac{1}{e^{\frac{h v_R}{k_B T}} - 1} \qquad \text{Anti-Stokes Scattering} \qquad (2.25)$$

$$\langle n_S \rangle + 1 = \frac{e^{\frac{h v_R}{k_B T}}}{e^{\frac{h v_R}{k_B T}} - 1} \qquad \text{Stokes Scattering} \qquad (2.26)$$

where $\langle n \rangle$ is the average number of phonons having a frequency equal to the Brillouin frequency shift v_B in the case of Brillouin scattering and the Raman frequency shift v_R in the case of Raman scattering, T is the absolute temperature in the unit of Kelvin, and k_B denotes the Boltzmann constant ($\sim 1.38 \times 10^{-23}$ m^2 kg s^{-2} K^{-1}). Using equations 2.25 and 2.26, we can see that due to the phonon annihilation in the anti-Stokes process, the scattering coefficient is proportional to $\langle n_S \rangle$, whereas during the Stokes process, where a new phonon is generated, the scattering coefficient is proportional to $\langle n_S \rangle + 1$. In the case of Brillouin scattering, the backreflected power may be scaled as follows: $(\langle n_S \rangle + 1) g_B \Gamma_B$ with g_B as the Brillouin gain and $\frac{\Gamma_B}{2\pi}$ as the Brillouin linewidth. More details concerning the gain and the linewidth follow in section 2.3.5.

Conservation of energy and momentum (Phase-matching condition)

Since Brillouin scattering involves coupling between electromagnetic waves and propagating acoustic waves with high momentum, the interaction requires the phase matching between the waves to be stringent. This simply means that a proper phase relationship between the interacting waves should be ensured along the propagation direction to guarantee an efficient coupling between the waves. To that effect, and concerning the Stokes process (equivalently for the anti-Stokes process), we shall apply energy and momentum conservation to the three interacting waves:
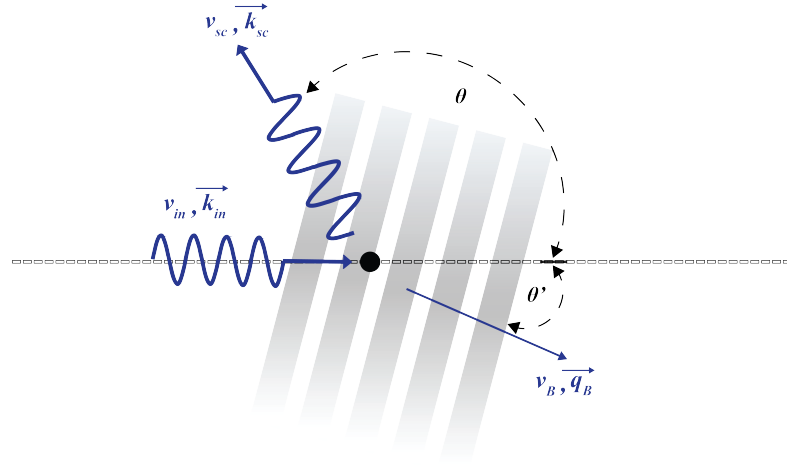
Figure 2.5 – Conservation of energy and momentum for spontaneous Brillouin scattering for the Stokes process; figure adapted from [14].

$$h\nu_{in} = h\nu_{sc} + h\nu_B \qquad\qquad \text{Energy Conservation} \qquad\qquad (2.27)$$

$$\hbar\overrightarrow{k_{in}} = \hbar\overrightarrow{k_{sc}} + \hbar\overrightarrow{q_B} \qquad\qquad \text{Momentum Conservation} \qquad\qquad (2.28)$$

where $\hbar = \frac{h}{2\pi}$ and is referred to as the reduced Planck's constant, ν_B is the Brillouin frequency shift and $\overrightarrow{q_B}$ is the acoustic wavevector. We then describe the three interacting waves with the following relationships:

- Incident optical wave having the velocity $v_o = \frac{c}{n_{\text{eff}}}$, the frequency $\nu_{in} = \frac{\omega_{in}}{2\pi} = \frac{k_{in}v_o}{2\pi}$ with ω_{in} as the angular frequency and $k_{in} = \left|\overrightarrow{k_{in}}\right|$ as the medium wavenumber and the magnitude of the wavevector $\overrightarrow{k_{in}}$. The wave is described by the following complex-valued electric field phasor:

$$E_{in}(z, t) = E_{0,in}(z, t)\, e^{-ik_{in}z + i\omega_{in}t} \qquad\qquad (2.29)$$

- Scattered optical wave having the velocity $v_o = \frac{c}{n_{\text{eff}}}$, the frequency $\nu_{sc} = \frac{\omega_{sc}}{2\pi} = \frac{k_{sc}v_o}{2\pi}$ with ω_{sc} as the angular frequency and $k_{sc} = \left|\overrightarrow{k_{sc}}\right|$ as the medium wavenumber and the magnitude of the wavevector $\overrightarrow{k_{sc}}$. The wave is described by the following complex-valued electric field phasor:

$$E_{sc}(z, t) = E_{0,sc}(z, t)\, e^{ik_{sc}z + i\omega_{in}t} \qquad\qquad (2.30)$$

- Acoustic wave having the velocity v_a, the frequency $\nu_B = \frac{\Omega_B}{2\pi} = \frac{q_B v_a}{2\pi}$ with Ω_B as the angular frequency and $q_B = \left|\overrightarrow{q_B}\right|$ as the acoustic wavenumber and magnitude of the acoustic wavevector $\overrightarrow{q_B}$. The wave is described by the following complex-valued electric

field phasor:

$$a(z, t) = a_0 \, e^{-i q_B z + i \Omega_B t} \tag{2.31}$$

where a_0 is the (time-independent, steady-state) density amplitude of the acoustic wave. We then end up with two coupled equations representing the separate vector components which are given as follows:

$$k_{\text{in}} = k_{\text{sc}} \cos(\theta) + q_B \cos(\theta') \tag{2.32}$$

$$k_{\text{sc}} \sin(\theta) = q_B \sin(\theta') \tag{2.33}$$

The diffraction grating illustrated in Fig. 2.5 represents the density variations (i.e. refractive index variations) induced by the acoustic wave present in the medium, and those variations are a consequence of a physical effect called photo-elasticity. This phenomenon occurs when the atomic density and the electric polarisation increase, as their increase leads to a higher electric susceptibility, which in turn causes a higher refractive index as per Eq. 2.12. The change in electric susceptibility can be written as a function of the initial average atomic density ρ_0 and its change $\Delta \rho$ using the following equation:

$$\Delta \chi = \frac{\gamma_e}{\rho_0} \Delta \rho \tag{2.34}$$

where $\gamma_e = \rho_0 \frac{\partial \epsilon}{\partial \rho}$ is the electrostrictive constant.

By squaring and summing the coupled equations presented in equations 2.32 and 2.33 and by making use of the relationships described above, we end up with the following general expression [14]:

$$4 v_a^2 v_{\text{in}} (v_{\text{in}} - v_B) \sin^2 \left(\frac{\theta}{2} \right) = \left(v_o^2 - v_a^2 \right) v_B. \tag{2.35}$$

Solving for v_B, Eq. 2.35 takes the following form:

$$v_B = 2 \frac{v_a}{v_o} v_{\text{in}} \sin \left(\frac{\theta}{2} \right) \sqrt{1 - \left(\frac{v_a}{v_o} \right)^2 \cos^2 \left(\frac{\theta}{2} \right)} - 2 \left(\frac{v_a}{v_o} \right)^2 v_{\text{in}} \tag{2.36}$$

The term $\left(\frac{v_a}{v_o} \right)^2$ can be reasonably approximated to zero, as it will lead to an infinitesimal value given that the medium light velocity v_o ($\sim 2 \times 10^8$ m/s in a silica medium) is at least four orders of magnitude larger the medium acoustic velocity v_a ($\sim 6 \times 10^3$ m/s in a silica medium). Accordingly, Eq.2.36 is written as follows:

$$v_B \approx 2 \frac{v_a}{v_o} v_{\text{in}} \sin \left(\frac{\theta}{2} \right) = 2 v_a \frac{n_{\text{eff}}}{\lambda_0} \sin \left(\frac{\theta}{2} \right) \tag{2.37}$$

where λ_0 is the incident light wavelength in vacuum. As can be clearly understood from

Eq. 2.37, the scattering angle θ has a major influence on the acoustic frequency or equivalently the amount of Brillouin frequency shift (BFS) experienced by the scattered light with respect to the incident light. If we substitute θ for 0° (i.e. scattering in the forward direction co-propagating with the incident light wave), we will right away realise that no shift will occur and the Brillouin scattering in the forward direction cannot be distinguished from the incident light. However, substituting θ for 180° (i.e. scattering in the backward direction counter-propagating with respect to the incident light wave), leads to the well-known phase-matching condition of backward Brillouin scattering:

$$\nu_B = 2n_{\text{eff}}\frac{\nu_a}{\lambda_0} \tag{2.38}$$

where we can see that ν_B is directly proportional to the acoustic velocity and the refractive index of the optical mode of the material. When launching a light that has $\lambda_0 = 1550$ nm in a standard silica SMF, ν_B usually lies somewhere between 9-11 GHz as shown in Fig. 2.2. The value of the ν_B differs according to different dopants applied to the fibre, and may even vary due to slight deviations in the fabrication process and the drawing conditions. This implies that fibres from the same manufacturer might no necessarily have the same exact BFS value. Obtaining the BFS value along an optical fibre is crucial for Brillouin based sensors. In fact, any change in the value given by the manufacturer essentially means that there is some sort of perturbation occurring in the surrounding of the fibre. Accordingly, distributed optical fibre sensing detecting changes in temperature or strain can be achieved by evaluating ν_B at each position in the fibre. To elaborate further and as mentioned earlier, we shall realise from Eq. 2.38 that ν_B is a function of ν_a that is related to the medium density through the following expression for solid media:

$$\nu_a = \sqrt{\frac{Y(1-\nu_p)}{\rho_0(1+\nu_p)(1-2\nu_p)}} \tag{2.39}$$

where Y is the Young's modulus also referred to as the modulus of elasticity or elastic modulus. It is a measure of how much resistance a material exhibits when it is subject to stretching. Thus, a material whose Young's modulus is high is more difficult to strain. ν_p is the Poisson's ratio, and ρ_0 is the medium density. The acoustic velocity ν_a simply represents the speed at which the acoustic wave presented by Eq. 2.31 propagates.

The temperature/strain sensitivities (i.e. the amount of change in the BFS with respect to the change in temperature T or strain ϵ for a conventional SMF at a wavelength of ~1550 nm are typically given as follows [18]:

$$\frac{\Delta\nu_B}{\Delta T} \approx 1 \text{ MHz/K} \qquad\qquad \frac{\Delta\nu_B}{\Delta\mu\epsilon} \approx 0.05 \text{ MHz/}\mu\epsilon$$

2.2.3 Raman scattering

In 1930, the Nobel Prize for physics was awarded to the Indian physicist C.V. Raman for his discovery in 1928 of the inelastic scattering phenomenon now known as Raman scattering. The effect named spontaneous Raman scattering occurs when light is shone on any arbitrary material which can be solid or a fluid. Unlike the elastic Rayleigh scattering, the scattering occuring due to the Raman effect is inelastic, meaning that the frequency of the scattered light is different from that of the incident light. We differentiate between two Raman processes; the Stokes process in which the scattered light components are down-shifted (i.e. having a lower frequency than the incident one), and the anti-Stokes process which involves a frequency up-shift of the scattered light (i.e. having a higher frequency than the incident one). As clearly illustrated in Fig. 2.1, the Raman scattering process involves vibrational or rotational transitions and the difference of photon energies is carried away by an optical phonon with an energy equal to $E = h\nu_R$ having a frequency corresponding to value of the frequency shift that took place. A typical frequency shift in a standard silica fibre at a centre frequency of ~193.5 THz is about ~13 THz as shown in Fig. 2.2.

Despite the fact that spontaneous Raman scattering is about 40 dB weaker (~-110 dB/m) than Rayleigh scattering (~-73 dB/m), it is, nevertheless, interesting to study because, unlike the other scattering processes, Raman scattering is only sensitive to temperature changes as elaborated in Fig. 2.2. This means that, when using silica fibres, the cross-sensitivity that is existent in sensing techniques relying on Rayleigh or Brillouin scattering is not a problem for Raman-based sensors. The first experimental demonstration was presented by *Dakin et al.* in 1985 [19].

The optical response and the behaviour of inelastic scatterings can be grasped by delving deeper into the understanding of a material's microscopic vibrations due to thermal motion inside the medium. Two different categories of vibrations are to be considered: the optical branch (Raman scattering) and the acoustic branch (Brillouin scattering) [14].

In the case of Raman scattering, when given a dense medium made of poly-atomic molecules for instance, the light interacts with optical-like thermally-activated vibrations (i.e. optical phonons) inside the molecular chain, for example like the bending or stretching modes between atoms within a molecule [20]. This interaction results in an excited quantum state due to the energy transfer between the incident photon and the vibration states of the molecule.

The temperature sensitivities of the Raman anti-Stokes and Stokes processes can be deduced from equations 2.25 and 2.26, where it can be seen that the temperature sensitivity of the anti-Stokes process (~ 0.83%/K) is higher than that of the Stokes process (~ 0.096%/K) [17]. By evaluating the scattering intensity ratio $I_{R(AS,S)}$ of both, the anti-Stokes I_{AS} and Stokes I_S processes, given by equations 2.26 and 2.25, using the following expression:

$$I_{R(AS,S)} = \frac{I_{AS}}{I_S} \propto \frac{\langle n \rangle}{\langle n \rangle + 1} = e^{\frac{h\nu_R}{k_B T}} \tag{2.40}$$

we get an exponential dependence of the intensity ratio on the temperature, making it possible to achieve distributed temperature sensing based on Raman scattering. The average phonon number in the Raman scattering process is significantly small, and is computed to be roughly ~ 0.14 in a silica optical fibre, when the frequency shift is $\nu_R = 13$ THz and $T = 300$ K.

Raman-based fully-distributed temperature sensors acting as nervous systems have proven to be highly crucial in numerous fields and applications such as in the oil and gas sector to keep track of pipeline leakages, in the energy distribution industry to detect any faults in power cables, and in civil engineering for structural health monitoring [21–23]. In this thesis, however, we will not study Raman scattering any further and the focus will be mainly on Rayleigh and Brillouin scatterings.

2.2.4 Fibre Bragg gratings

In the previous sections, we were talking about inevitable natural scattering processes occurring in solid silica fibres. Now, we will study a type of purposefully-engineered scattering mechanisms that can be manipulated and altered according to the need. Its principle is mostly the same as that of Rayleigh scattering explained in section 2.2.1. Both types of scatterings are are based on the same concept of scattering due to core density fluctuations, except for the fact that Rayleigh scattering centres exist unintentionally and are unavoidable, whereas fibre Bragg gratings are purposefully-engineered.

A fibre Bragg grating designates a periodic variation of the refractive index that is inscribed in the core of an optical fibre by exposing the latter to high-energy light. This refractive index variation is mostly of the order of $\sim 1 \times 10^{-3}$ which causes a relatively strong reflection. There are different fabrication techniques, one of which utilises a phase mask to imprint the corrugation [24], and another that employs femto-second lasers to achieve a point-to-point inscription of the gratings [25], and several others. Gratings are spectrally selective, as they exhibit a narrow reflectivity located around a specific wavelength that is determined by the following Bragg condition:

$$\lambda_{\text{Bragg}} = 2n_{\text{eff}}\Lambda_{\text{G}} \tag{2.41}$$

where Λ_{G} is the grating period and n_{eff} is the effective refractive index, and as can be seen in Eq. 2.41, the Bragg wavelength is dependent on these two parameters. Fibre Bragg gratings notably found applications in optical signal processing, where they may be used as filters, or in fibre based optical sensors, where they may be employed to measure parameters such as strain, temperature, pressure or humidity. Exposing the fibre to temperature changes or applying mechanical deformations to its core will result in a modification in the grating period (Λ_{G}), which in turn changes the Bragg wavelength (λ_{Bragg}). Accordingly, a shift of the FBG spectrum occurs as can be seen in Fig. 2.6 where the period Λ_G of the non-perturbed FBG corresponds to λ_{Bragg}, whereas Λ' of the perturbed FBG corresponds to λ'. By properly characterising this shift, one may infer the fibre temperature or stress from the measurement of the FBG central

wavelength. The following equation describes the effect of both temperature and strain, when applied to the fibre [26, 27]:

$$\Delta\lambda_{\text{Bragg}} = 2\left(\frac{\partial n_{\text{eff}}}{\partial l} + n_{\text{eff}}\frac{\partial \Lambda_{\text{G}}}{\partial l}\right)\Delta l + \left(\frac{\partial n_{\text{eff}}}{\partial T} + n_{\text{eff}}\frac{\partial \Lambda_{\text{G}}}{\partial T}\right)\Delta T \tag{2.42}$$

The relative change in Bragg wavelength due to strain is calculated by the following equation:

$$\frac{\Delta\lambda_{\text{Bragg}}}{\lambda_{\text{Bragg}}} = \left(1 - \underbrace{\frac{n_{\text{eff}}^2}{2}[p_{12}\nu_p(p_{11} + p_{12})]}_{p_e}\right)\varepsilon_z \tag{2.43}$$

where p_{11} and p_{12} are the strain-optic coefficients, $\nu_p = -\frac{\varepsilon_r}{\varepsilon_z}$ is the Poisson's ratio and $\varepsilon_z = \frac{\delta l}{l}$ where δl is the resulting elongation length and l is the total length of the fibre. The term denoted by p_e is the effective photo-elastic constant and is 0.22 in silica fibres [26]. Applying strain to the fibre leads to the longitudinal elongation of the fibre. For a typical germano-silicate fibre, 1 μɛ strain corresponds to 1.2 pm shift in centre wavelength (1550 nm).

The change in temperature results in an elongation of the fibre, which is described by the thermal expansion coefficient and in a change in the refractive index, which is described by the thermo-optic coefficient. The relative change in Bragg wavelength due to temperature is calculated by the following equation:

$$\frac{\Delta\lambda_{\text{Bragg}}}{\lambda_{\text{Bragg}}} = (\alpha_{\Lambda_{\text{G}}} + \alpha_{n_{\text{eff}}})\Delta T \tag{2.44}$$

where $\alpha_{\Lambda_{\text{G}}} = \left(\frac{1}{\Lambda_{\text{G}}}\right)\left(\frac{\partial \Lambda_{\text{G}}}{\partial T}\right)$ is the thermal expansion coefficient of the fibre that accounts for thermally-induced elongation, and is approximately $0.55 \times 10^{-6}\text{K}^{-1}$ for silica [26], and $\alpha_{\Lambda_{\text{G}}} = \left(\frac{1}{n_{\text{eff}}}\right)\left(\frac{\partial n_{\text{eff}}}{\partial T}\right)$ is the thermo-optic coefficient accounts for thermally-induced refractive index change, approximately $8.6 \times 10^{-6}\text{K}^{-1}$ for germanium-doped silica-core fibre [26], and 6 ×
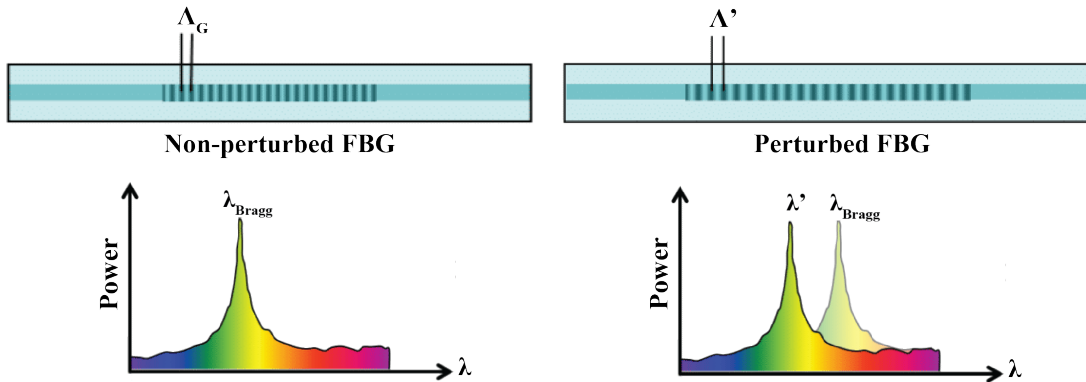
Figure 2.6 – Fibre Bragg grating written inside an optical fibre showing the spectrum of the backreflected signal for a non-perturbed and a perturbed FBG.

10^{-6}K^{-1} for silica fibres. The expected sensitivity for a 1550 nm Bragg grating is approximately 13.7 pm/K .

Fibre Bragg gratings have proven their high sensitivity as point sensors and accordingly received great attention as promising candidates for distributed sensing as they can be relatively easily multiplexed. Using these highly sensitive point sensors serially along the sensing distance, researchers were able to achieve quasi-distributed sensing at many points along the fibre [28], calling this structure Bragg grating arrays. These arrayed gratings, however, are not continuously distributed along the whole fibre, and can therefore only perform sensing along the positions at which the gratings are inscribed in the fibre. Despite that, Bragg grating array sensors are useful for applications where fully-distributed measurement is not necessarily required. In section 3, we will discuss a recently-introduced grating-based standard single-mode fibre that shows great potential in long-haul sensing.

2.3 Light scattering in gaseous media

In the previous section 2.2, we focused on elaborating on the different scattering mechanisms (inevitable and purposefully-engineered) occurring in solid silica fibres. It is natural to think that scattering also takes place in other types of media such as gases. In this section, we will explain some gas thermodynamics and how light scattering in gases occurs. The theory presented in this section is mainly based on the work conducted in [13] and is important to be thoroughly understood, as it will be further applied to the evaluation and analysis of the characteristics of gas-filled state-of-the-art hollow-core optical fibres, which is the topic of this thesis' chapters 6 and 7.

2.3.1 Some thermodynamics: Ideal gas

Equation of state for an ideal gas

The ideal gas model is a simplified and approximated concept that obeys the ideal gas law which is a simplified equation of state. It is used to predict the behaviour of gases and assumes that the gas molecules are small hard spheres moving in random directions yet are separated by an average distance (mean-free path) that is much larger than the size of the molecules. The model also assumes that the molecules only possess kinetic internal energy meaning that no account is taken of rotational or vibrational energy, and that no friction occurs between the molecules resulting in purely elastic collisions.

First proposed by Emile Clapeyron in 1834, the ideal gas law's purpose is to gather the laws of physical chemistry into one expression. The thermodynamic state of a fluid as per the ideal gas law combines the following parameters: the volume V, the number of moles per volume (volumetric number density) $n_d = \frac{N_t}{V}$ with N_t as the total number of molecules in the gas, the

ideal gas pressure P_{id}, and the temperature T, and is given as follows:

$$P_{\text{id}}V = n_d RT \longrightarrow P_{\text{id}} = RT\frac{1}{V_m} = RT\frac{\rho_0}{M_m} \tag{2.45}$$

where the proportionality constant R is the universal ideal gas constant, and is equal to $8.314\,\text{J}\,\text{K}^{-1}\text{mol}^{-1}$ which is the product of the Boltzmann constant k_B and Avogadro's number given by $N_A \sim 6.02214 \times 10^{23}\,\text{mol}^{-1}$. The molar volume V_m (i.e. the volume occupied by one mole) is given by the quotient $\frac{\rho_0}{M_m}$ where ρ_0 is the gas density and M_m is the molar mass. The ideal gas law gas can alternatively also be written as a function of the total number of molecules in the gas N_t rather than the number of moles n_d:

$$P_{\text{id}}V = N_t k_B T \longrightarrow P_{\text{id}} = \frac{N_t}{V}k_B T = n_d k_B T \tag{2.46}$$

Specific heat capacity for an ideal gas

The specific heat is defined as the quantity of heat energy Q per unit mass m needed to raise the temperature of a substance by one unit of temperature. The heat energy and the occurring temperature change are related through the specific heat capacity $c = \frac{C}{m}$, with C as the heat capacity, using the following expression:

$$Q = cm\Delta T \tag{2.47}$$

There are two distinct specific heat capacities depending on which of the two parameters, the pressure or the volume, is being kept constant throughout the heating process. At constant pressure (isobaric), the specific heat capacity is denoted by c_P, and in the case of maintaining a constant volume (isochoric), it is designated as c_V. While a substance (a gas for instance) is being heated, the specific heat capacity at constant pressure may be noticeably higher than that at constant volume. This is because at constant pressure, the medium is allowed to expand and exert work on its surrounding while it is being heated, whereas at constant volume, the heat occurs in a closed vessel that does not allow expansion. A key parameter in the evaluation of the specific heat is the quotient $\gamma_h = \frac{c_P}{c_V}$ which is known as the heat capacity ratio or the adiabatic index. The two quantities c_P and c_V are also related to the universal gas constant R through the Mayer's relation for an ideal gas by:

$$c_{P,M_m} - c_{V,M_m} = R \longrightarrow c_P - c_V = \frac{R}{M_m} \tag{2.48}$$

where $c_{P,M_m} = c_P M_m$ and $c_{V,M_m} = c_V M_m$ are the molar heat capacities.

Bulk modulus for an ideal gas

All fluids tend to get compressed/expanded when subjected to external forces. The amount of resistance to compression/expansion a substance shows is measured by its bulk modulus

K. It is described as the ratio of pressure change to the fractional change in volume per unit volume, and can be also described as a function of the fluid density since the volume is inversely proportional to it. Accordingly, the bulk modulus is formally defined by the following expression:

$$K = -V\frac{\mathrm{d}P}{\mathrm{d}V} = \rho_0 \frac{\mathrm{d}P}{\mathrm{d}\rho_0} \tag{2.49}$$

where the negative sign in $-V\frac{\mathrm{d}P}{\mathrm{d}V}$ is due to the fact that the increase of the applied pressure causes the volume to decrease but the density to increase as can be intuitively inferred from Eq. 2.49. The reciprocal of the bulk modulus gives the substance compressibility. Two types of bulk moduli can be defined, namely the isothermal bulk modulus at constant temperature $K_T = \left(\rho_0 \frac{\mathrm{d}P}{\mathrm{d}\rho_0}\right)_{T=\text{constant}}$, and the adiabatic also called isentropic bulk modulus at constant entropy $K_s = \left(\rho_0 \frac{\mathrm{d}P}{\mathrm{d}\rho_0}\right)_{s=\text{constant}}$. The two bulk moduli are related through the quotient of the specific heat capacities (heat capacity ratio) γ_h as follows:

$$\gamma_h = \frac{c_p}{c_V} = \frac{K_s}{K_T} \tag{2.50}$$

By differentiating Eq. 2.45 at constant temperature and substituting the expression for the isothermal bulk modulus K_T, we will see that $K_T = P$, and according to Eq. 2.50, it follows that $K_s = \gamma_h P$.

2.3.2 Some thermodynamics: Non-ideal gas

Equation of state expansion for a non-ideal gas

When the simplifying assumptions of the ideal gas model have to be given up, like in the case when gas is subjected to high pressure or high temperature, for example, the ideal gas approach will no longer be accurate and Eq. 2.45 has to be modified accordingly. Different techniques have been developed to solve this more difficult problem of the so-called many-particle system. The classical approach consists in firstly finding a reference state that can roughly represent the real system under consideration and its characteristics are not too deviated from it. We can then apply some type of perturbation theory around this reference state such as the virial expansion, for instance. This will provide systematic corrections to the ideal gas law, and yield a more suitable approximation for the real system as a function of temperature, pressure and the system density. Accordingly, Eq. 2.45, the pressure-explicit form of the equation of state for the ideal gas can be adjusted by the virial expansion in powers of the reciprocal molar volume or the gas density as follows [29, 30]:

$$P = P_{\text{id}}(T)\left(1 + \frac{B(T)}{V_m} + \frac{C(T)}{V_m^2} + ...\right) = P_{\text{id}}(T)\left(1 + B(T)\frac{\rho_0}{M_m} + C(T)\frac{\rho_0^2}{M_m^2} + ...\right) \tag{2.51}$$

with $B(T)$ and $C(T)$ as the second and third virial coefficients, respectively. These coefficients are a function of the temperature and act as correction factors for the equation of state while the gas density is increasing. They can be deduced from experiments or theoretically evaluated from the exact form of the inter-particle interaction potential $U(r)$ using the Lennard-Jones potential [31]. The second virial coefficient can be estimated using the following expression [32]:

$$B(T) = -2\pi \int_0^\infty r^2 \left[e^{\frac{-U(r)}{k_B T}} - 1 \right] dr \tag{2.52}$$

where r is the distance between two interacting particles and k_B is the Boltzmann constant. The more particles interact with each other (e.g. with increase of pressure), the more corrective terms (virial coefficients) are needed to reach a more accurate approximation of the equation of state. The virial coefficients have been thoroughly studied for many fluids and tabulated in several references [33–35]. The second and third virial coefficients provide the most correction to the ideal gas law, which is why for many practical purposes, these two coefficients alone are usually enough for a proper estimation up to ~100 bar.

Specific heat capacity for a non-ideal gas

Just like the equation of state for non-ideal gases, the specific heat capacities c_P and c_V should be altered to cope with high pressure and temperature changes. The same approach can be followed using the virial expansion where we determine a reference state and expand from it. The reference in our case is based on the ideal gas conditions. We will then denote the reference heat capacities by $c_{P,id}$ and $c_{V,id}$, and the virial expansion reads [29]:

$$c_P(P,T) \approx c_{P,id} - \frac{P}{M_m} \left(T \frac{\mathrm{d}^2 B(T)}{\mathrm{d}T^2} \right) \quad c_V(P,T) \approx c_{V,id} - \frac{P}{M_m} \left(2 \frac{\mathrm{d}B(T)}{\mathrm{d}T} + T \frac{\mathrm{d}^2 B(T)}{\mathrm{d}T^2} \right) \tag{2.53}$$

where P is the real gas pressure and not the pressure in the ideal gas conditions. $\frac{\mathrm{d}B(T)}{\mathrm{d}T}$ and $\frac{\mathrm{d}^2 B(T)}{\mathrm{d}T}$ are the first and second derivatives of the second virial coefficient, respectively. The heat capacity ratio is then calculated using the expressions presented in Eq. 2.53, and the expansion takes the following form [II]:

$$\gamma_h(P,T) = \frac{c_P(P,T)}{c_V(P,T)} = \frac{c_{P,id} - \frac{P}{M_m} \left(T \frac{\mathrm{d}^2 B(T)}{\mathrm{d}T^2} \right)}{c_{V,id} - \frac{P}{M_m} \left(2 \frac{\mathrm{d}B(T)}{\mathrm{d}T} + T \frac{\mathrm{d}^2 B(T)}{\mathrm{d}T^2} \right)}$$

$$\approx \gamma_{h,id} + \frac{1}{c_{V,id}} \frac{P}{M_m} \left(2 \frac{\mathrm{d}B(T)}{\mathrm{d}T} \gamma_{h,id} + T \frac{\mathrm{d}^2 B(T)}{\mathrm{d}T^2} \left(\gamma_{h,id} - 1 \right) \right) \tag{2.54}$$

where $\gamma_{h,id} = \frac{c_{P,id}}{c_{V,id}}$ is the ideal gas heat capacity ratio from where the virial expansion starts. Taking the difference of the altered specific heat capacities of Eq. 2.53, the following expression

---

[II]The final expression is attained and approximated by simplifying the original expression using $(1 - x)(1 + x) = 1 - x^2$, and neglecting the higher order terms.

for the expanded Mayer's relation is yielded:

$$c_P(P,T) - c_V(P,T) \approx c_{P,id} - c_{V,id} + \frac{P}{M_m}\left(2\frac{\mathrm{d}B(T)}{\mathrm{d}T}\right) \tag{2.55}$$

These modified expressions using the virial expansion will be further utilised to find a proper approximation for the acoustic velocity in a non-ideal gas which will be presented in section 2.3.6.

Bulk modulus for a non-ideal gas

In the case of a non-ideal gas, we will follow the same drill as before and apply the virial expansion on the bulk moduli, and expand up to the third virial coefficient. Using Eq. 2.51 and Eq. 2.49 at constant temperature, the expanded isothermal bulk modulus will be written as follows:

$$K_T \approx P_{\mathrm{id}}(T)\left(1 + 2B(T)\frac{\rho_0}{M_m} + 3C(T)\frac{\rho_0^2}{M_m^2}\right) \tag{2.56}$$

Utilising the relationship between the isothermal and the adiabatic bulk moduli presented in Eq. 2.50 along with Eq. 2.54 and Eq. 2.56, the following expression is yielded for the adiabatic bulk modulus:

$$K_s \approx \gamma_{\mathrm{h,id}}P_{\mathrm{id}}(T)\left(1 + 2B(T)\frac{\rho_0}{M_m} + \frac{1}{c_{V,\mathrm{id}}}\frac{P_{\mathrm{id}}(T)}{M_m}\frac{\mathrm{d}B(T)}{\mathrm{d}T}\right) \tag{2.57}$$

2.3.3 Gas flow regimes

There are different regimes which describe the behaviour of gas molecules at different gas pressures, and how the light scattering is affected accordingly [37, 38]. A key parameter defining those regimes is the ratio between the scattering wavelength and the mean-free path between molecular collisions referred to as the y-parameter which is essentially the inverse of
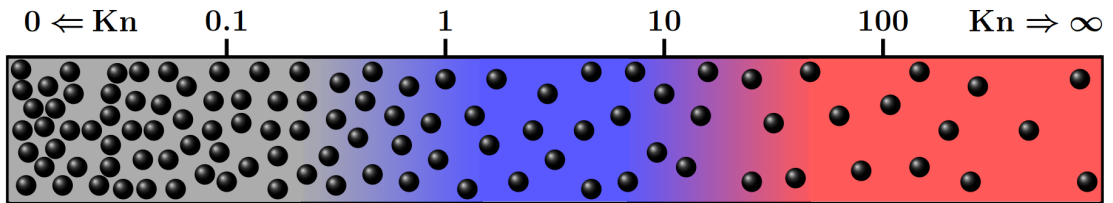
Figure 2.7 – Schematic showing the different gas flow regimes and the Knudsen number corresponding to them [36].

the Knudsen number K_n, and is given by the following expression [39]:

$$y = \frac{1}{2\pi} \frac{\lambda}{L_{\mathrm{mfp}}} = \frac{P}{k v_{\mathrm{th}} \eta_{\mathrm{s}}} = \frac{n_d k_B T}{k v_{\mathrm{th}} \eta_{\mathrm{s}}} \tag{2.58}$$

where λ is the wavelength of the scattered light, $L_{\mathrm{mfp}} = \frac{v_{\mathrm{th}}}{\alpha_{\mathrm{col}}}$ is the mean free path of the gas molecules, P is the gas pressure, v_{th} is the thermal velocity defined as $v_{\mathrm{th}} = \sqrt{\frac{2k_B}{M}}$ with M as the molecular mass, $\alpha_{\mathrm{col}} = \frac{P}{\eta_s}$ is an effective collision frequency, η_s as the shear viscosity of the gas, n_d is the volumetric number density, and T is the gas temperature. The wavevector $\overrightarrow{k}$ with its magnitude or wavenumber $k = \frac{2\pi}{\lambda}$ is defined as the difference between the scattered $\overrightarrow{k_{\mathrm{sc}}}$ and the incident $\overrightarrow{k_{\mathrm{in}}}$ wavevectors as follows: $\overrightarrow{k} = \left| \overrightarrow{k_{\mathrm{sc}}} - \overrightarrow{k_{\mathrm{in}}} \right|$. The different regimes are demonstrated in Fig. 2.7 along with their corresponding Knudsen number which simply determines what is the current gas flow regime. Three flow regimes are defined using the Knudsen number, namely the hydrodynamic regime (continuum flow) with $K_n \ll 1$ for high gas densities, the kinetic regime with 1 $K_n \approx 1$, and the Knudsen regime (Knudsen diffusion or free molecular flow) with $K_n \gg 1$ for low gas densities. Compared with the scattering wavelength, the mean free path of gas molecules in the hydrodynamic regime is so small that the gas can be treated as a continuous medium, thus classical Navier–Stokes equations can be applied to calculate the spectrum of the scattered light. The spectrum will contain three Lorentzian-shaped peaks, namely a central Rayleigh peak and two displaced Brillouin peaks (Stokes and anti-Stokes) on each side of the Rayleigh peak. In the Knudsen regime, the mean free path between collisions is very large and the light gets scattered by the gas molecules individually, and the spectral profile takes the form of a Rayleigh distribution. As for the kinetic regime with the intermediate range of Knudsen number, the gas flow cannot be treated using the continuum nor the individual particle approaches. In that case, the spectral shape cannot be straightforwardly obtained as in the case of the hydrodynamic and the Knudsen regimes. Accordingly, different models based on solutions of the Boltzmann distribution for the density fluctuations have been developed and validated for the spectra at this intermediate regime [40–42].

2.3.4 Rayleigh scattering cross-section

Molecular Rayleigh scattering occurs when light experiences elastic scattering from gas molecules. The total Rayleigh volume-scattering coefficient reads:

$$\beta_R = \sigma_R n_d \tag{2.59}$$

where σ_R is the Rayleigh scattering cross-section for a single molecule and is expressed as follows [43]:

$$\sigma_R = \frac{24\pi^3}{\lambda^4 n_d^2} \frac{(n_{\mathrm{gas}}^2 - 1)^2}{(n_{\mathrm{gas}}^2 + 2)^2} \frac{6 + 3\rho_n}{6 - 7\rho_n} \tag{2.60}$$

where n_d is the volumetric number density, n_{gas} is the gas refractive index, and the fraction $\frac{6+3\rho_n}{6-3\rho_n}$ is called the King correction factor with ρ_n as the depolarisation factor which describes the effect of molecular anisotropy. The term $\frac{(n_{\text{gas}}^2-1)^2}{(n_{\text{gas}}^2+2)^2}$ is a factor in the Lorentz-Lorenz relation which expresses the refractive index n_{gas} of a substance in terms of the atomic polarisability α_p. Polarisability describes the tendency of a substance that is subjected to an electric field to acquire an electric dipole moment which is proportional to the field applied to it. The Lorentz-Lorenz relation is written as follows [44]:

$$\frac{n_{\text{gas}}^2-1}{n_{\text{gas}}^2+2} = \frac{N_A \rho_0}{M_m} \frac{\alpha_p}{3\epsilon_0} = n_d \frac{\alpha_p}{3\epsilon_0} \longrightarrow n_{\text{gas}}^2 = \frac{2\rho_0\left(\frac{N_A}{M_m 3\epsilon_0}\right)\alpha_p + 1}{1 - \rho_0\left(\frac{N_A}{M_m 3\epsilon_0}\right)\alpha_p} \tag{2.61}$$

where N_A is Avogadro's number, ρ_0 is the gas density, M_m is the molar mass, and n_d is the number density. The term $F_{LL} = \left(\frac{N_A}{M_m 3\epsilon_0}\right)$ will be denoted as the Lorenz-Lorentz factor. It should be noted that by replacing the refractive index n_{gas} by ϵ_r using the Maxwell relation $\epsilon_r = n_{\text{gas}}^2$, Eq. 2.61 will then be called the Clausius-Mossotti relation.

Unlike in section 2.2.1, where light was scattered by steady density fluctuations in solid silica, here light is scattered by moving gas particles. This means that the spectral width of the scattered light will experience some broadening (Doppler effect) due to the motion of the molecules. Information about some gas parameters can be directly inferred from the Rayleigh spectrum. For example, the bulk flow velocity of the gas can be determined by knowing the amount of Doppler shift away from the incident central frequency. Additionally, the spectrum's total intensity is directly related to the gas density, and the width of the Rayleigh spectrum is a function of the gas temperature. This indicates that proper modeling of the Rayleigh spectrum is needed to be able to analyse the gas parameters. Therefore, the gas flow at different conditions has to be studied because the gas density has a direct impact on the shape of the spectrum.

2.3.5 Brillouin scattering in gas

In chapters 6 and 7 of this thesis, we are mainly interested in the hydrodynamic gas flow regime, as we will be analysing the occurrence of Brillouin scattering which becomes very prominent in this regime. The scattering spectral distribution associated with this flow regime consists of three Lorenztian-shaped peaks, and can be described as follows [39, 45]:

$$S_{\text{hy}}(q_B, \omega) \propto \underbrace{\left(\frac{\gamma_h - 1}{\gamma_h}\right) \frac{q_B^2 \kappa_C / \rho_0 c_P}{\omega^2 + (\kappa_C q^2 / \rho_0 c_P)^2}}_{\text{Rayleigh Peak}} + \underbrace{\frac{1}{\gamma_h}\left(\frac{\Gamma_B q_B^2}{(\omega + q_B v_a)^2 + (\Gamma_B q_B^2)^2}\right)}_{\text{Anti-Stokes Brillouin Peak}}$$
$$+ \underbrace{\frac{1}{\gamma_h}\left(\frac{\Gamma_B q_B^2}{(\omega - q_B v_a)^2 + (\Gamma_B q_B^2)^2}\right)}_{\text{Stokes Brillouin Peak}} \tag{2.62}$$

where q_B is the acoustic wavenumber, ω is the angular frequency of the light, κ_C is the thermal conductivity, Γ_B is the acoustic attenuation, and ν_a is the acoustic velocity. Eq. 2.62 includes three terms for each of the three spectral lines. The first term corresponds to the spectral distribution of Rayleigh scattering caused by the entropy waves as in the thermal fluctuations present in the molecules, and two anti-Stokes and Stokes Brillouin distributions existing because of the sound waves (phonons) that move either along or in the opposite direction of the scattering vector k resulting in momentum transfer to the incident photons. This then causes either an increase (anti-Stokes) or a decrease (Stokes) of the scattered light frequency as thoroughly explained in section 2.2. The shift in frequency occurring for the Brillouin lines is dependent on the gas and the wavelength used, and is given by the same equation for silica, namely $\nu_B = \frac{2n_{\text{eff}}\nu_a}{\lambda_0}$ as in Eq. 2.38.

Brillouin linewidth

The acoustic attenuation is a function of several thermodynamic quantities and is given by [46]:

$$\Gamma_B = \frac{q_B^2}{\rho_0}\left(\frac{(\gamma_h - 1)\kappa_C}{c_P} + \eta_b + \frac{4}{3}\eta_s\right) \tag{2.63}$$

where η_b and η_s are the volume (bulk) and shear viscosities, respectively. It is apparent from Eq. 2.63 that the acoustic attenuation of a sound wave in gas is mainly caused by the thermal conductivity and the viscous forces simply arising from the random motion of the gas molecules. The thermal conduction is defined as the energy diffusion across a temperature gradient (from higher to lower temperatures). The shear viscosity, however, is the result of a momentum transfer due to thermal diffusion which, in the presence of a velocity gradient, leads the gas molecules to diffuse from the higher to the lower flow velocity. The strength of the two processes highly depends on the strength of the gradients. The bulk viscosity involves the slow irreversible energy exchange between the internal degrees of freedom (e.g. rotational and vibrational modes) and the translational mode. This transfer of energy has an opposed direction at each π-phase-shift of the wave and leads to attenuation of the acoustic wave [47]. The Brillouin linewidth (i.e. full width at half maximum (FWHM) of the Lorentzian spectrum) is proportional to the acoustic attenuation and is simply given by $\frac{\Gamma_B}{2\pi}$.

Brillouin gain

The Brillouin gain obtained due to the interaction of the optical waves with the sound waves can be described as follows [11]:

$$\widetilde{g_B} = \frac{\gamma_e^2 \omega^2}{n_{\text{gas}}\, \nu_a\, c^3\, \rho_0\, \Gamma_B} \text{ (in m/W)} \tag{2.64}$$

where $\widetilde{g_B}$ is the intrinsic Brillouin gain, and g_B is the Brillouin gain that is calculated as a function of the acousto-optic overlap effective area expressed by A_{ao} as shown in the following equation:

$$g_B = \frac{\gamma_e^2 \omega^2}{n_{\mathrm{gas}} \, v_a \, c^3 \, \rho_0 \, \Gamma_B \, A_{\mathrm{ao}}} \ (\mathrm{in} \ \mathrm{m}^{-1}\mathrm{W}^{-1}) \tag{2.65}$$

where $\gamma_e = \rho_0 \frac{\partial \epsilon_r}{\partial \rho}$ is the electrostrictive coefficient in the gas medium and is described as the rate of change of the relative permittivity with respect to the gas density ρ, ω is the angular frequency of the light, n_{gas} is the gas index of refraction, c is the speed of light in vacuum, and A_{ao} is the acousto-optic overlap effective area. It is obvious from Eq. 2.65 that the Brillouin gain is highly dependent on the electrostrictive coefficient which is dependent on gas refractive index which itself changes with the variation in the gas density. We can, accordingly, use the Lorenz-Lorentz equation presented by Eq. 2.61 to help us estimate the electrostrictive coefficient when the gas density changes. By differentiating Eq. 2.61 with respect to the gas density ρ_0, we end up with:

$$\frac{\mathrm{d}n_{\mathrm{gas}}}{\mathrm{d}\rho} = \frac{3F_{LL}}{2n\left(1 - \rho F_{LL}\right)^2} = \frac{\left(n_{\mathrm{gas}}^2 - 1\right)\left(n_{\mathrm{gas}}^2 + 2\right)}{6\,n_{\mathrm{gas}}\rho} \tag{2.66}$$

The electrostrictive coefficient can then be determined using Eg. 2.12 and Eq. 2.66 as follows:

$$\gamma_e = \rho_0 \frac{\partial \epsilon_r}{\partial \rho} = \rho_0 \frac{\partial \chi}{\partial \rho} \longrightarrow \gamma_e = 2n_{\mathrm{gas}}\rho \frac{\partial n_{\mathrm{gas}}}{\partial \rho} = \frac{\left(n_{\mathrm{gas}}^2 - 1\right)\left(n_{\mathrm{gas}}^2 + 2\right)}{3} \tag{2.67}$$

It ought to be remarked that ρ_0 represents the initial gas density without any changes applied to it, whereas when the parameter becomes ρ, it means that there was a change in the gas density and the initial gas density is altered. As can be seen from Eq. 2.67, the electrostrictive coefficient is directly proportional to the gas density $\gamma_e \propto \rho$, and from Eq. 2.63 we infer that the Brillouin linewidth is inversely proportional to the gas density $\frac{\Gamma_B}{2\pi} \propto \frac{1}{\rho}$. Accordingly, and from Eq. 2.65, we observe that the Brillouin gain essentially depends on the gas density in a quadratic manner. This is an important realisation, as it shows the possibility to benefit from this square dependence by increasing the gas pressure, hence the gas density, and yielding significantly high Brillouin gains [13, 48]. The experimental demonstration verifying this relationship utilising different hollow-core fibres is presented in chapter 7.

2.3.6 Acoustic velocity in gas

Ideal gas

In section 2.2.2, we describe the acoustic velocity in Eq. 2.39 for solid silica as a function of the Young's modulus and the Poisson's ratio. For gas, however, the acoustic velocity is dependent on the Bulk modulus. The isentropic bulk modulus is related to the Young's

modulus Y mentioned in Eq. 2.39 through the following relation: $Y = K_T(1 - 2\nu_p)$, where ν_p is the Poisson's ratio. The acoustic velocity ν_a is then given by the following expressions:

$$\nu_a = \frac{\Omega_B}{q_B} = \sqrt{\frac{K_s}{\rho_0}} = \sqrt{\frac{\gamma_h K_T}{\rho_0}} = \sqrt{\frac{\gamma_{h,id} P}{\rho_0}} = \sqrt{\frac{\gamma_{h,id} RT}{M_m}} \tag{2.68}$$

It should be noted that the last two expressions are only valid for the ideal gas approximation.

Non-ideal gas

In the case of a non-ideal gas, where the gas is subjected to higher changes of temperature or pressure which cannot be properly approximated using the ideal gas approximation, the value of the bulk modulus needs to be determined correctly for a proper approximation of the acoustic velocity. To that effect, if of course the gas is not entirely deviated from an ideal gas, Eq. 2.68 can be amended using correction factors to the expression of the velocity for an ideal gas:

$$\nu_a = \sqrt{\frac{\gamma_h K_T}{\rho_0}} = \sqrt{\gamma_h \left(\frac{\partial P}{\partial \rho_0}\right)_T} \tag{2.69}$$

where the virial expansion in ρ_0 is applied as follows:

$$\left(\frac{\partial P}{\partial \rho_0}\right)_T \approx \frac{P_{id}}{\rho_0}\left(1 + 2B(T)\frac{\rho_0}{M_m} + 3C(T)\frac{\rho_0^2}{M_m^2}\right) \tag{2.70}$$

We then substitute γ_h and $\left(\frac{\partial P}{\partial \rho_0}\right)_T$ for their expanded expressions in Eq. 2.54 and Eq. 2.70, respectively, into Eq. 2.69. The final expression is yielded by ignoring the virial coefficients products along with the third virial coefficient ($C(T)$) and applying first order approximation to the square root, and in turn it follows:

$$\nu_a \approx \nu_{a,id} + \nu_{a,id}\frac{\rho_0}{M_m}\left(B(T) + \frac{1}{c_{P,id}}\frac{RT}{2M_m}\left(2\gamma_{h,id}\frac{\mathrm{d}B(T)}{\mathrm{d}T} + T\left(\gamma_{h,id} - 1\right)\frac{\mathrm{d}^2 B(T)}{\mathrm{d}T^2}\right)\right) \tag{2.71}$$

where $\nu_{a,id}$ is the acoustic velocity, given by Eq. 2.68, calculated for the case of an ideal gas. It is taken as the reference state from which the virial expansion starts. Eq. 2.71, however, is severely approximated which means that it can no longer hold at relatively high changes of pressures or temperatures. Despite that, it is quite safe to use it in the work presented in this thesis (in section 7) because the ranges of pressures reached are well below the threshold above which the expression breaks.

2.3.7 Acoustic velocity dependencies

Dependence on temperature

It can be directly observed from Eq. 2.68 that the acoustic velocity of an acoustic wave at constant entropy is a function of temperature in the ideal gas approximation, and to describe the rate of change of the acoustic velocity with the respect to the temperature, we write:

$$\left(\frac{\partial v_a}{\partial T}\right)_P = \left(\frac{\partial v_a}{\partial T}\right)_{\rho_0} = \frac{\sqrt{\frac{\gamma_{h,id}R}{M_m}}}{2\sqrt{T}} \xrightarrow{\times\frac{\sqrt{T}}{\sqrt{T}}} \frac{v_a}{2T} \tag{2.72}$$

This means that the temperature change would be the same whether the gas is assumed to be allowed to freely move in or out of an enclosure (i.e. constant pressure) or is confined within a sealed enclosure (i.e. constant density).

In the case of the non-ideal gas, where the acoustic velocity is approximated and governed by Eq. 2.71, we can understand that the acoustic velocity is dependent on the virial coefficient $B(T)$ and its derivative.

Dependence on pressure

The equation of state of an ideal gas presented by Eq. 2.45 shows that the pressure is proportional to the density at constant temperature. That said, and according to Eq. 2.68, we can clearly see that the acoustic velocity in the ideal gas situation does not show any dependence on the applied pressure. However, this relationship is different for the non-ideal gas case, as from the of expression of the acoustic velocity based on the virial expansion given by Eq. 2.71, we can immediately notice that the linear dependence of the acoustic velocity on the gas density which itself, as explained earlier, is related to the pressure through the virial expansion Eq. 2.51.

2.4 Interrogation techniques for optical fibre sensing

The scattering of light occurring in the different media which we have discussed in the previous sections is the very reason behind optical fibre sensing. The scattered light from the optical fibre contains essential localised information about the fibre surroundings. For this purpose, several interrogation techniques have been designed and implemented to detect the different types of scatterings. Here, we will present the fundamental principles upon which the currently-existing interrogation techniques rely. These include systems based on the interrogation in the time domain, in the frequency domain and in the correlation domain. The choice of the experimental system solely depends on the application and its needs. When there is an access to only one side of the optical fibre, the interrogation is referred to as reflectometry, whereas when both sides of the optical fibre are utilised for the experiment, the interrogation is called analysis. Further on in the thesis, we will only deal with time-domain and correlation-
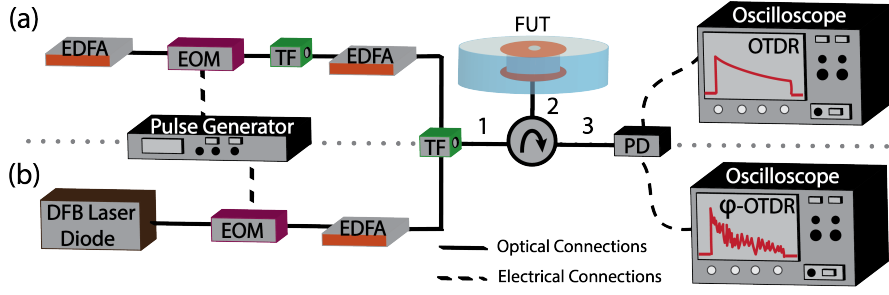
Figure 2.8 – Experimental setup examples of (a) OTDR; and (b) φ-OTDR. (DFB: Distributed feedback laser, EOM: Electro-optic modulator, EDFA: Erbium-doped fibre amplifier, TF: Tunable filter, VA: Variable attenuator, PD: Photo-detector, FUT: Fibre Under Test).

domain reflectometres which is why no emphasis was given on frequency-domain techniques nor was it given on analysis interrogation techniques, as they are out of the scope of this work.

2.4.1 Optical time-domain reflectometry

Optical time-domain reflectometry (OTDR), as its name suggests, is based on the time-of-flight measurement. The concept of time-of-flight in an OTDR can be assimilated to that of a radar system, in which radio waves travel through some medium (typically air), hit a target, and get reflected back. The position of that target is determined by the time it took the waves to complete a round-trip between the start position and the target. In contrast to a radar system, an OTDR is not based on radio waves for the interrogation, but it relies on shooting intensity-modulated optical waves (typically rectangular pulses) inside a waveguide (e.g. optical fibre), and as indicated earlier, the light gets scattered by any obstacle encountered while traveling through the fibre, be it fibre drawing defects, connection and splice losses, end-face Fresnel reflections, or others. Using the time-of-flight information of the received optical signal, the distance d traveled to the target and back can be directly calculated and precisely estimated by $d = \frac{ct}{2n_{\text{eff}}}$, where $\frac{c}{n_{\text{eff}}}$ is the propagation group velocity v_{group}[III] of the optical waves in the fibre. The back-scattered power received at the detector can be formulated as follows [14]:

$$P_{BS} = P_{in}\, \alpha_{BS}\, R_{sp} \exp\left(-2\alpha z\right) \tag{2.73}$$

where P_{in} is the input peak power to the fibre, and R_{sp} is the spatial resolution (in m) of the OTDR system (which is equivalent to half of the physical length of the interrogation pulse launched into the fibre), α is the linear fibre attenuation coefficient assumed to be constant at each position z, and the factor 2 accounts for the round-trip time that the light takes to reach the receiver at the input of the fibre. In 1976, *Barnoski et al.* [28] demonstrated the first experimental implementation of what is currently referred to as a conventional incoherent OTDR. It has been and is up until now (nowadays converted into a handy compact instrument)

[III] $\frac{c}{n_{\text{eff}}}$ is taken as the group velocity v_{group} since we are considering our medium to be non-dispersive in which case the phase velocity v_p is equal to v_{group}.

a very useful technique to evaluate the losses over entire optical links, and different sorts of applications whether in research laboratories or in the industry. Apart from the conventional incoherent OTDR, there is another type of OTDR that relies on a coherent light source instead of an incoherent one. The implementation of both techniques is essentially the same except for the light source utilised which can be seen in Fig. 2.8. As their names clearly indicate, in an incoherent OTDR, the light source is incoherent having a wide spectrum (e.g. the amplified spontaneous emission of an Erbium-doped fibre amplifier (EDFA)), whereas in a coherent OTDR, the light source is coherent with a narrow linewidth (e.g. laser). A coherent OTDR is also referred to as phase-sensitive OTDR (φ-OTDR), and can be subdivided into different techniques such as frequency-scanned direct-detection φ-OTDR which will be intensively discussed in section 4, and chirped-pulse φ-OTDR [49].

A conventional incoherent OTDR can solely be utilised to detect faults in fibre lines, but it cannot fulfil the requirement to achieve distributed optical fibre sensing because it lacks the coherence properties existent in coherent OTDRs. When a coherent laser source is used, the backreflected waves undergo constructive and destructive interference at the receiving end. The acquired jagged light intensity trace (lower oscilloscope in Fig. 2.8) can be utilised to retrieve the phase information of the waves through signal processing to provide useful localised information about the fibre surroundings. However, when the light source is incoherent, it means that the backreflected waves carry random phases, which when added together, will result in an averaged-out intensity trace as monitored on the upper oscilloscope in Fig. 2.8. Accordingly, loss of localised information is the outcome and no localised sensing can be realised with an incoherent OTDR.

2.4.2 Optical correlation-domain reflectometry

Optical correlation-domain (also referred to as coherence-domain) reflectometry (OCDR) is based on controlling the optical coherence of the light source. This can be achieved by directly modulating the laser frequency though direct injection current modulation [50] or
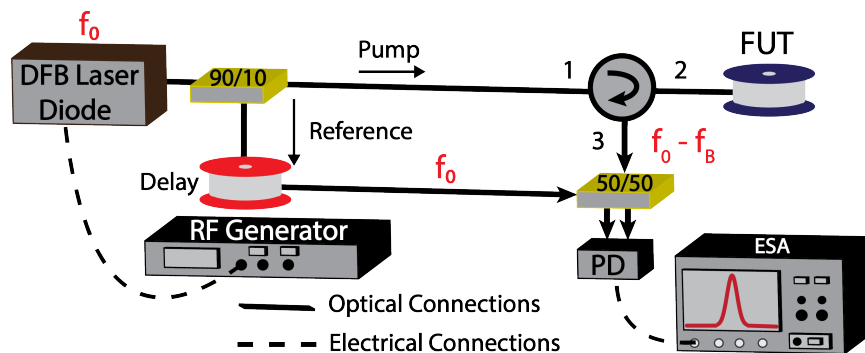
Figure 2.9 – General schematic of a BOCDR experimental setup example.

phase-modulation [51]. Another way would be by changing the laser source and using the amplified-spontaneous emission (ASE) of a fibre amplifier as the source instead [52].

OCDRs are typically utilised for the detection of Brillouin scattering and are in that case referred to as Brillouin optical correlation-domain reflectometres (BOCDR). Fig. 2.9 shows a general schematic as an example of a BOCDR, where the laser frequency is dithered by means of an RF generator. It is seen from the figure that the laser light gets divided into pump and reference branches. The reference signal is delayed and acts as a local oscillator that beats with the spontaneous Brillouin scattered light from the fibre under test (FUT).

When we take a look at Fig. 2.10 (a), we will see that the two beating signals may be in-phase or out-of-phase. When the two beating signals are in-phase, this heterodyne beating at the photo-detector (PD) results in a correlation peak (illustrated in Fig. 2.10 (b)) that may be moved along the fibre when the modulation frequency is altered. The Brillouin gain spectrum (BGS) can only be measured when the correlation between the two signals is high. However,
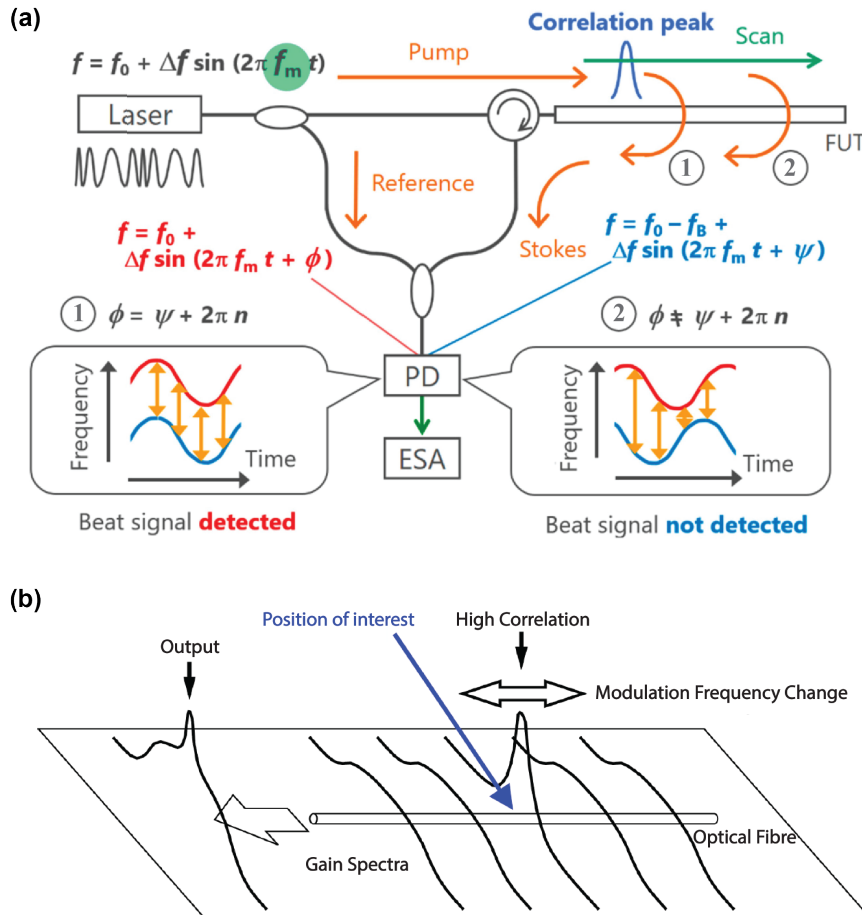
Figure 2.10 – (a) Conceptual schematic of an example of BOCDR using sinusoidal frequency modulation to the laser [53]; (b) Illustration showing the high correlation resulting in the measurement of the BGS; figure adapted from [54].

in the other case where the two signals are out-of-phase, the correlation is significantly small, and accordingly no BGS can be observed. From Fig. 2.10 (b), we can clearly see that the high correlation is at one particular position (beating signals are in-phase) and for the rest of the fibre positions (beating signals are out-of-phase) the correlation is almost negligible. In such a system the measurement range is given as a function of the modulation frequency f_m as follows:

$$D_m = \frac{v_{\text{group}}}{2f_m} \tag{2.74}$$

where v_{group} is the group velocity. The spatial resolution is given by:

$$R_{\text{sp}} = \frac{v_{\text{group}} \Delta v_B}{2\pi f_m \Delta f} \tag{2.75}$$

where $\Delta v_B = \frac{\Gamma_B}{2\pi}$ is the Brillouin linewidth and Δf is the amplitude of the frequency dithering. As can be realised from equations 2.74 and 2.75, both parameters are interlinked and there is a trade-off between a smaller spatial resolution and a larger measurement range. Other techniques were, therefore, developed to overcome this problem [55]. Still for many applications, such a system is quite convenient, as it offers a very small spatial resolution (of course depending on the length of the fibre) and is very easy to implement compared to many other configurations and interrogation systems. In chapter 7, it will be shown how this approach can be utilised in practice and will be opted for to conduct fully-distributed optical fibre sensing.

3 Investigation of fibres with enhanced directional backreflection

3.1 Introduction

In the fundamentals section 2, we have seen that the different scattering processes present in the standard silica optical fibres enable us to perform localised sensing which is entirely distributed and is only a matter of how short the spatial resolution is and how long the sensing range can be. If we take some time to think about it, we can understand that fibre Bragg gratings are nothing but purposefully-engineered density fluctuations. This, of course, reminds us of the fundamental scattering process in an optical fibre, namely Rayleigh scattering which occurs due to the inevitable density fluctuations created during the fibre drawing process. In section 2.2.1, we have rigorously discussed how it occurs and briefly mentioned that it results in scattering in almost all directions as shown in Fig. 2.4. What we have not yet addressed is the fact that during the process of Rayleigh scattering, when the light gets scattered in many directions, only a small fraction of the light actually gets recollected by the receiver. The power of the backreflected light reaching the input end of the fibre from a distance z is described by the following equation:

$$P_{\mathrm{BR}} = P_{\mathrm{in}}\,\alpha_{\mathrm{BR}}\,R_{\mathrm{sp}}\exp\left(-2\alpha z\right) \tag{3.1}$$

where P_{in} is the peak input power to the fibre, α_{BR} is the backreflection coefficient, R_{sp} is the spatial resolution, and $\exp\left(-2\alpha z\right)$ accounts for the round-trip loss experienced by the light while it's propagating along the fibre. As apparent from Eq. 3.1,the power captured by the receiver P_{BR} is proportional to the backreflection coefficient α_{BR} which itself can be written as:

$$\alpha_{\mathrm{BR}} = \alpha_{\mathrm{BS}}\,F_{\mathrm{Re}} \tag{3.2}$$

with α_{BS} as the scattering coefficient and F_{Re} as the recapture fraction. The recapture fraction is a function of the numerical aperture (NA) of the fibre and the refractive index $F_{\mathrm{Re}} = \frac{(NA)^2}{4.3n^2}$. For a standard single-mode fibre (SMF), the reflection parameters take the values presented in table 3.1 [16, 56]. From the table, we can see that about 28.9 dB (corresponding to an efficiency

Parameter	Symbol	Value
Scattering Coefficient	α_{BS}	$\sim 4.2 \times 10^{-5} \text{m}^{-1}$ ($\sim$-43.8 dB m^{-1})
Recapture Fraction	F_{Re}	$\sim 1.3 \times 10^{-3}$ ($\sim$-28.9 dB)
Reflection Coefficient	α_{BR}	$\sim 5.4 \times 10^{-8} \text{m}^{-1}$ ($\sim$-72.7 dB m^{-1})

Table 3.1 – Typical reflection values for a standard silica SMF.

of $\sim$0.13%) of the scattered light is lost and never reaches the receiver. This, of course, triggers curiosity and makes us think of solutions to overcome this problem to make use of all the scattered signal.

One of the most common techniques adopted to achieve SNR enhancement in Rayleigh-based sensors relies on the core manipulation of the sensing fibre, thereby inducing supplementary density fluctuations in the fibre core which in turn results in higher Rayleigh scattering. Therefore, several studies in the literature proposed different approaches to increase the scattering centres along the fibre, for instance with the use of nano-particle doping achieving a back-scatter enhancement of 36.5 dB, yet a round-trip loss of 25.5 dB/m [57], or using UV exposure reaching 50 dB of signal enhancement with a 0.15 dB/m induced loss [58, 59], along with others.

An inevitable repercussion of improving the Rayleigh back-scattering through the enhanced scattering in *many directions* (shown in Fig. 3.1) by inducing more scattering centres is the increased total loss in the fibre; ergo, only short distance sensing would be possible. For instance, let us assume a scenario in which a 30 dB enhancement in the backreflected signal is achieved, yet is obtained at the expense of a fibre loss of around 0.2 dB/cm. In such case, the accordingly enhanced backreflected signal will result in a higher/equivalent back-scattered power only up to a distance of $\sim$74 cm when compared with a standard SMF (0.2 dB/km). Thus, considering the total cost of manipulated fibres along with the added fibre losses, the
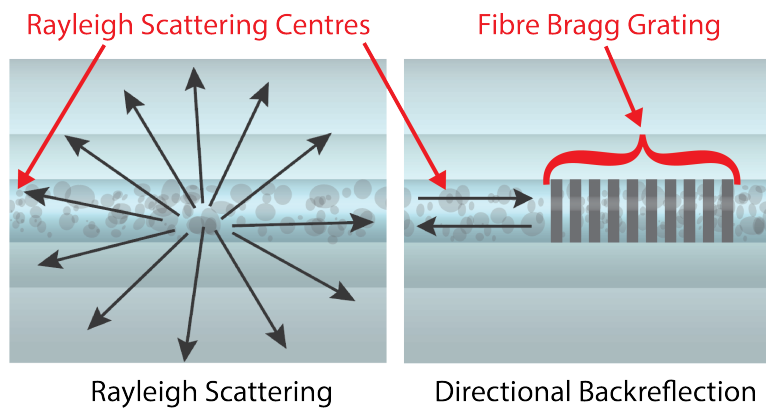
Figure 3.1 – Illustration showing the directional reflection due to the purposefully-engineered fibre Bragg gratings, and the Rayleigh scattering occurring due to the inevitable Rayleigh scattering centres.

real benefit of the higher SNR obtained by increasing the number of scattering centres is quite sceptical. However, such fibres can still find a panoply of applications which don't demand long range distributed sensing yet require high accurate measurements of the measurand, such as in biomass reactors, nuclear reactors, and others.

3.2 Directional reflection

As a consequence of the high loss induced by the scattering centres, the spotlight has been turned on the inscription of faint Bragg gratings along the sensing fibre to benefit from an enhanced *directional* backreflected signal (shown in Fig. 3.1) with a fairly low fibre loss [56, 60]. Firstly presented in [61], *Thévenaz et al.* demonstrated the idea of using faint long grating (FLOGs) as fully-distributed sensors. This work opened the door for FBGs to be also considered for long fully-distributed optical fibre sensing. However, it should be remarked that the gratings can no longer have very high reflectivities like the ones used for point or quasi-distributed sensing. This is because with such high modulations of the refractive index ($\sim 1\times10^{-3}/1\times10^{-4}$), all the light will be reflected, hence only short distances can be interrogated, as the pulse will be depleted right away. That is why, careful treatment of the gratings is required and reflectivities corresponding to the order of the Rayleigh density fluctuations ($\sim 1\times10^{-7}/1\times10^{-8}$) need to be achieved. A confusion would probably arise at this point where we wonder that if we need the gratings to be as weak as the Rayleigh density fluctuations, then why fabricate gratings in the first place? Aren't gratings supposed to be strong enough to ensure a strong reflection? To answer this question, we have to firstly understand that in this scenario, gratings are needed to achieve a *directional* reflection which cannot be yielded by point-like scattering centres. A lot of works have been oriented towards increasing the number of Rayleigh scattering centres [57, 58] which indeed increases the scattering in many directions, but does not fulfil the directionality requirement, and therefore, does not necessarily lead to an enhanced **received** signal. This because gratings have refractive index changes **across the entire cross-section**, while random irregularities do not. Accordingly, gratings can be thought of as weak *directional* reflection barriers from which the light is reflected with ~100% efficiency.

In this chapter, we talk about some types of long faint gratings and how they can be fabricated. We will also study the spatio-temporal coupling between the counter-propagating waves (a temporal pulse and a continuous wave) using the coupled-mode theory after presenting the conventional spatial coupled-mode theory in section 3.4.1, which will allow us to further understand which type of gratings are the most suitable for achieving fully-distributed sensing.

3.3 Types of fibre Bragg gratings

There are a lot of different types of fibre Bragg gratings which have been extensively discussed in the literature to be employed for various applications [62]. In our case, we are only interested in the fibre Bragg gratings which can be beneficial to be utilised for long distributed fibre
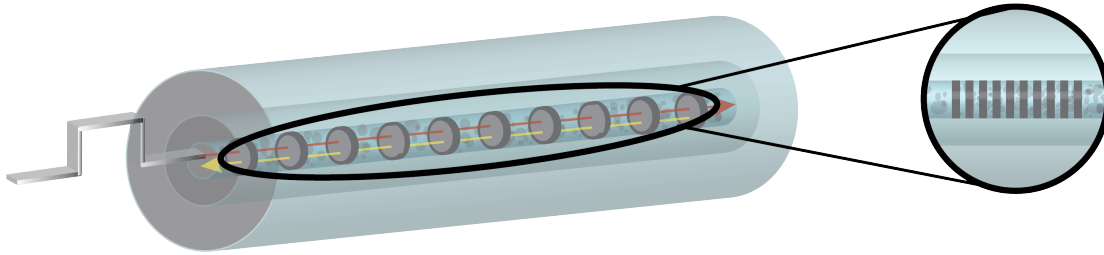
Figure 3.2 – Schematic showing an optical fibre with uniform fibre Bragg gratings written in its core. The figure on the right shows a top view of the fibre cross-section highlighting the uniform distribution of the gratings along the fibre.
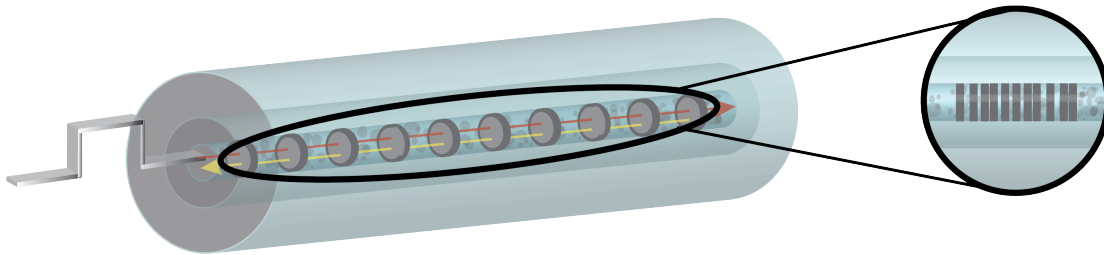
Figure 3.3 – Schematic showing an optical fibre with random fibre Bragg gratings written in its core. The figure on the right shows a top view of the fibre cross-section highlighting the random distribution of the gratings along the fibre.

sensing. The type of grating which would, at first glance, make the most sense would be uniform long faint gratings [61].

3.3.1 Uniform gratings

By uniform gratings it is meant that the gratings are continuously written and the grating pitch is the same all along the fibre as can be seen in Fig. 3.2. This means that during the grating inscription process, no phase-hopping occurs. In reality, uniform gratings are quite challenging to achieve, simply because an extremely high accuracy of the translation stage is needed. This, however, is not the only hurdle when it comes to uniform gratings, as we will see in section 3.4.2. We will come to understand that the strong grating uniformity is actually a disadvantage for long range sensing.

3.3.2 Random gratings

Given the multiple problems faced when we talk about uniform gratings, we shall introduce another type of gratings which is of high interest to us, namely random gratings. The randomness comes mainly from the random spacing between the different gratings as can be seen in Fig. 3.3. Random gratings can be also subdivided into randomly-spaced single-wavelength gratings and randomly-spaced chirped gratings. As their names already indicate, the former

has identical grating periods, whereas the latter has different periods with the Bragg frequency increasing or decreasing. The chirping can be along the whole fibre or over the individual gratings. If the chirping is done over the whole length of the fibre, this means that when the fibre length is decreased, some frequencies will be removed from the reflection spectrum. In the other case, however, by reducing the fibre length, the reflection will be reduced, but all the frequencies covered by the chirping will still appear in the reflection spectrum.

3.4 Coupled-mode theory

The coupled-mode theory or formalism is usually opted for to model the coupling of various types of systems (optical, electrical, etc.). It is often used in guided-wave optics as a perturbational approach to analyse electromagnetic wave propagation and media interaction in space and time [62, 63].

3.4.1 Spatial coupled-mode theory

Spatial coupled-mode theory, as its name suggests, consists in modelling a system in the space domain. Here, we will revise the analytical solution for the spatial coupling between two waves in a perturbed waveguide having sinusoidal corrugation of the refractive index as a prerequisite to the spatio-temporal coupled-mode theory presented in section 3.4.2. We differentiate between the spatial and the spatio-temporal coupling situations, as in the former situation the coupled waves are continuous waves (CW) that are interacting at all times during their presence in the waveguide, whereas in the latter situation the coupling occurs between a CW and a temporal pulse that propagates along the waveguide and interacts with the CW only at specific instants of time.

The sinusoidal corrugation of the refractive index (illustrated in Fig. 3.4) is a good approximation for a fibre Bragg grating where the perturbation term shows a dependency on the
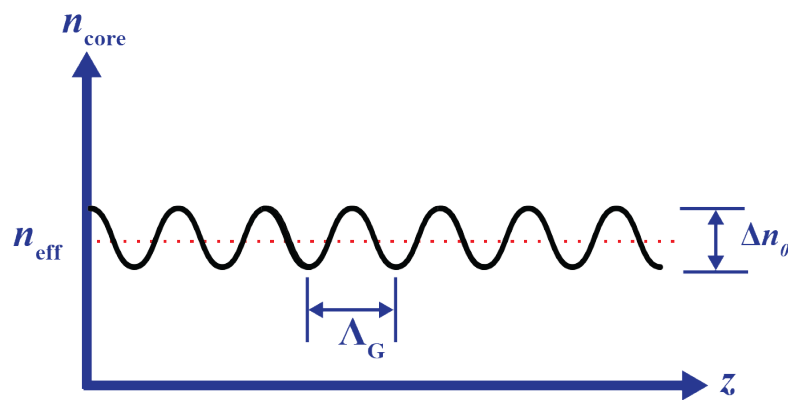
Figure 3.4 – Sinusoidal variation of the refractive index of the fibre core along the z-coordinate.

longitudinal spatial coordinate z as described by the following expression:

$$\Delta n(z) = \Delta n_0 \cos(Kz) = \frac{1}{2}\Delta n_0 (e^{iKz} + e^{-iKz}) \tag{3.3}$$

where $K = \frac{2\pi}{\Lambda_G}$ with Λ_G is the perturbation period as illustrated in Fig. 3.4.

If we assume that we are dealing with a single-mode waveguide (e.g. standard single-mode fibre) and that the perturbation is isotropic as far as polarisation is concerned, only two distinct eigenwaves present in the waveguide can be coupled as a result of the perturbation, namely one forwardly-propagating wave and another backwardly-propagating. The perturbed fields of these two counter-propagating waves take the following general form:

$$E_{\text{in}}(z) = E_{0,\text{in}}(z)\, e^{-i k_{\text{in}} z} \qquad\qquad \text{Forward Propagation} \tag{3.4}$$

$$E_{\text{sc}}(z) = E_{0,\text{sc}}(z)\, e^{+i k_{\text{sc}} z} \qquad\qquad \text{Backward Propagation} \tag{3.5}$$

where $E_{0,in}(z)$ and $E_{0,sc}(z)$ are the amplitudes (envelopes), and $\pm z$ indicates the direction of propagation. By examining the effect of both counter-propagating waves on each other, we will end up with the Helmholtz equation stating [64–66]:

$$\nabla^2 E_{\text{in}} + n_{\text{eff}}^2 k_{\text{in}} E_{\text{in}} + \underbrace{\Delta n_{\text{eff}} n(z) k_{\text{in}} E_{\text{sc}}}_{\text{Perturbation}} = 0 \tag{3.6}$$

Substituting the expressions in 3.5 into Eq. 3.6, simplifying by using the slowly varying envelope approximation [62], we yield the following two coupled equations for the amplitudes:

$$\frac{\mathrm{d}}{\mathrm{d}z} E_{0,\text{in}}(z) = -i C_c e^{i\Delta K z} E_{0,\text{sc}(z)}$$
$$\frac{\mathrm{d}}{\mathrm{d}z} E_{0,\text{sc}}(z) = +i C_c e^{-i\Delta K z} E_{0,\text{in}(z)} \tag{3.7}$$

where $\Delta K = 2k_m - K$ is the deciding factor of whether the coupling is at resonance (i.e. $\Delta K = 0 \longrightarrow 2k_m = K$) or off-resonance (i.e. $\Delta K \neq 0$); assuming that $k_m = k_{\text{in}} = k_{\text{sc}}$, and $C_c = \frac{\Delta n_0 k_0}{2}$ is the coupling constant with $k_0 = \frac{k_m}{n_{\text{eff}}}$.

When we talk about resonant coupling, it means that the period of the sinusoidal variation of the refractive index is chosen to be $\Lambda_G = \frac{2\pi}{2k} = \frac{\lambda_m}{2}$ where $\lambda_m = \frac{\lambda_0}{n_{\text{eff}}}$ is the wavelength of the light in the medium. Solving the coupled equations presented in Eq. 3.7, we get an expression for each amplitude taking the following form [64]:

$$E_{0,\text{in}}(z) = A_0 \frac{e^{C_c(z-L)} + e^{-C_c(z-L)}}{e^{C_c(L)} + e^{-C_c(-L)}} = A_0 \frac{\cosh(C_c(z-L))}{\cosh(C_c L)}$$
$$E_{0,\text{sc}}(z) = i A_0 \frac{e^{C_c(z-L)} - e^{-C_c(z-L)}}{e^{C_c(L)} + e^{-C_c(-L)}} = A_0 \frac{\sinh(C_c(z-L))}{\cosh(C_c L)} \tag{3.8}$$

where A_0 is the initial amplitude at the zeroth position $E_{0,\text{in}}(0) = A_0$ of the incident wave, and L is the total length of the waveguide. The coupling efficiency in terms of intensity $\left(\frac{I_{\text{sc}}}{I_{\text{in}}}\right)$ or

grating reflectivity (R_G) can be calculated using the following equation:

$$\frac{I_{sc}}{I_{in}} = R_G = \tanh^2(C_c L) \tag{3.9}$$

In the case when the coupling is off-resonant, it is interesting to study and determine the spectral interval over which the coupling remains efficient when the resonant frequency is shifted in either direction. An analytical solution can also be formulated for this case and is given as follows:

$$E_{0,in}(z) = A_0 e^{i\frac{\Delta_K}{2}z} \frac{\zeta \cosh(\zeta(z-L)) - i\frac{\Delta_K}{2}\sinh(\zeta(z-L))}{\zeta \cosh(\zeta L) + i\frac{\Delta_K}{2}\sinh(\zeta L)}$$
$$E_{0,sc}(z) = A_0 e^{-i\frac{\Delta_K}{2}z} \frac{C_c \sinh(\zeta(z-L))}{\zeta \cosh(\zeta L) + i\frac{\Delta_K}{2}\sinh(\zeta L)} \tag{3.10}$$

where $\zeta = \sqrt{C_c^2 - \left(\frac{\Delta_K}{2}\right)^2}$, and the reflectivity in this case is given by:

$$\frac{I_{sc}}{I_{in}} = R_G = \frac{C_c^2}{C_c^2 + \frac{\zeta^2}{\sinh^2(\zeta L)}} \tag{3.11}$$

The coupled-mode formalism, as already explained, is quite a strong mathematical tool and can accurately model coupling and energy transfers between waves in optical fibres. In this section, we have explained how it can be utilised for static fibre Bragg gratings, but it is also worth mentioning that it can be applied when the perturbation is caused by a dynamic grating as well, just like in the case of Brillouin scattering [67].

3.4.2 Spatio-temporal coupled-mode theory

Numerical model

For a distributed optical fibre sensing system based on time-domain techniques (one of the most commonly-used methods for the interrogation of Rayleigh backreflected signals), the coupling between the propagating waves will have to be described a bit differently than the model studied in section 3.4.1. One of the interacting waves will be an interrogating temporal pulse instead of a continuous wave. This means that the coupling will not occur between two continuous waves as in the case of the spatial coupled-mode theory. To that effect, we need to slightly modify the equations presented in 3.4.1 to have an accurate model. In this case, the perturbed fields of the counter-propagating signals take the following form:

$$E_{in}(z,t) = E_{0,in}(z,t)\, e^{-ik_{in}z + i\omega t} \qquad \text{Forward Propagation} \tag{3.12}$$
$$E_{sc}(z,t) = E_{0,sc}(z,t)\, e^{+ik_{sc}z + i\omega t} \qquad \text{Backward Propagation} \tag{3.13}$$

By substituting equations 3.13 and 3.13 into Eq. 3.6 and using the slowly varying envelope approximation, we end up with the following two coupled equations:

$$\frac{\partial}{\partial z}E_{0,\text{in}}(z,t) + \frac{1}{v_g}\frac{\partial}{\partial t}E_{0,\text{in}}(z,t) = -iC_c e^{i\Delta Kz}E_{0,\text{sc}}(z,t)$$
$$\frac{\partial}{\partial z}E_{0,\text{sc}}(z,t) - \frac{1}{v_g}\frac{\partial}{\partial t}E_{0,\text{sc}}(z,t) = +iC_c e^{-i\Delta Kz}E_{0,\text{in}}(z,t)$$

(3.14)

where v_g is the group velocity, $\Delta K = 2k_m - K$ is the deciding factor of whether the coupling is at resonance (i.e. $\Delta K = 0 \longrightarrow 2k_m = K$) or off-resonance (i.e. $\Delta K \neq 0$); assuming that $k_m = k_{\text{in}} = k_{\text{sc}}$, and $C_c = \frac{\Delta n_0 k_0}{2}$ is the coupling constant with $k_0 = \frac{k_m}{n_{\text{eff}}}$.

The equations provided in Eq. 3.14 are extremely challenging to be solved analytically unless a strong assumption is made. For example, such equations have been solved for dynamic gratings in the case of Brillouin scattering, but with the assumption that the incident pulse is unchanged throughout its propagation along the fibre [67]. This assumption is valid in that case, as the interaction is supposed to be weak enough so that the pulse depletion can be neglected. In our case, however, this assumption is definitely not valid because the backreflected signal is actually created from the forwardly-propagating temporal pulse. This means that if we assume that the pulse is not being slightly depleted while it is propagating, there will not be any reflected signal in the first place. That is why, the model has to incorporate the energy transfer of the interrogation pulse to the backreflected signal even though the interaction might be relatively weak. To that effect, our only resort would be going for solving those equations numerically. For this, we will proceed by utilising the first derivative of the central difference theorem of 4th order accuracy and the 4th order Runge-Kutta method. Runge-Kutta methods are iterative approaches used to perform numerical analyses and solve initial-value problems of differential equations. Such methods were presented by the German mathematicians Carl Runge and Wilhelm Kutta [68].

We will assume that we are at resonance; ΔK will be equal to zero hence reducing the exponential term on the right hand side of the coupled equations in 3.14 to 1. The numerical solution will follow using two steps:

1. Discretisation of the two equations in space using the first derivative of the central difference theorem of 4th order
2. Solving the discretised equations using the 4th order Runge-Kutta numerical method by sweeping them with time

Firstly, we will rearrange the coupled equations as follows:

$$\frac{\partial}{\partial t}E_{0,\text{in}}(z,t) = -v_g\left(\frac{\partial}{\partial z}E_{0,\text{in}}(z,t) + iC_c E_{0,\text{sc}}(z,t)\right)$$
$$\frac{\partial}{\partial t}E_{0,\text{sc}}(z,t) = v_g\left(\frac{\partial}{\partial z}E_{0,\text{sc}}(z,t) - iC_c E_{0,\text{in}}(z,t)\right)$$

(3.15)

where $\frac{\partial}{\partial t}E_0(z,t)$ can be written using the 4th order centred difference approximation given as

follows:

$$\left(\frac{\partial}{\partial z}E_0(z,t)\right)_i = \frac{-E_{0,i+2} + 8E_{0,i+1} - 8E_{0,i-1} + E_{0,i+2}}{12\Delta z} + O(\Delta z^4) \tag{3.16}$$

The rearranged coupled equations governed by Eq. 3.16 can then be straightforwardly sub-stituted in Eq. 3.15, and we accordingly yield the following discretised coupled equations in space:

$$\begin{aligned}
\frac{\partial}{\partial t}E_{0,\text{in}}(z,t) &= -v_g\left(\frac{-E_{0,\text{in},i+2} + 8E_{0,\text{in},i+1} - 8E_{0,\text{in},i-1} + E_{0,\text{in},i+2}}{12\Delta z} + iC_c E_{0,\text{sc}(z,t)}\right) \\
\frac{\partial}{\partial t}E_{0,\text{sc}}(z,t) &= v_g\left(\frac{-E_{0,\text{sc},i+2} + 8E_{0,\text{sc},i+1} - 8E_{0,\text{sc},i-1} + E_{0,\text{sc},i+2}}{12\Delta z} - iC_c E_{0,\text{in}(z,t)}\right)
\end{aligned} \tag{3.17}$$

Following the discretisation of the coupled equations in space, we will then proceed by solving them using the 4th order Runge-Kutta (RK4) numerical method which states [68, 69]:

$$\begin{aligned}
k_1 &= h_t f(t_n, y_n) \\
k_2 &= h_t f\left(t_n + \frac{h_t}{2}, y_n + \frac{k_1}{2}\right) \\
k_3 &= h_t f\left(t_n + \frac{h_t}{2}, y_n + \frac{k_2}{2}\right) \\
k_4 &= h_t f(t_n + h, y_n + k_3) \\
y_{n+1} &= y_n + \frac{k_1}{6} + \frac{k_2}{3} + \frac{k_3}{3} + \frac{k_4}{6}
\end{aligned} \tag{3.18}$$

where h_t is the time step, f is the central difference approximation function, t_n is the time for which we are solving the coupled equations, y_n describes each of the original coupled equations, and y_{n+1} describes the solution to each of the coupled equations.

In Eq. 3.18, k_1 is the slope at the beginning of the interval, depending only on y, k_2 is the slope at the midpoint of the interval, using y and k_1, k_3 is also the slope at the midpoint of the interval, but is a function of y and k_2, and finally k_4 is the slope at the end of the interval which depends on y and k_3. As seen in Eq. 3.18, greater weight is given to the slopes at the midpoint, when the four slopes are averaged. Since the RK4 numerical technique is a fourth-order method, the local truncation error is on the order of $O(h_t^5)$, and the total accumulated error is on the order of $O(h_t^4)$.

Results and conclusion

The model was solved for a 60 m long standard single-mode fibre with an effective refractive index of about $n_{\text{eff}} = 1.5$ for different pulse widths. A typical pulse width for experimental systems is about $\tau_{\text{pw}} =10$ ns which corresponds to a spatial resolution $R_{\text{sp}} =1$ m. We, therefore, will only show the results corresponding to this spatial resolution. The gratings introduced to the fibre are in the form of a sinusoidal variation of the refractive index with a change
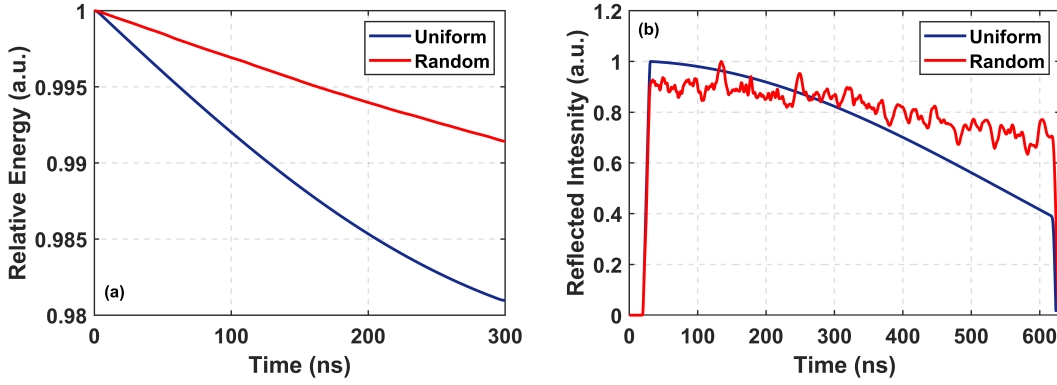
Figure 3.5 – Graph comparing the numerical results of uniform and random gratings (a) Pulse relative energy at the far end of the fibre as a function of the propagation time; (b) Backreflected intensity as a function of the propagation time considering the round-trip traveled by the light.

corresponding to $\Delta n_0 = 1 \times 10^{-8}$ which is roughly of the same order of magnitude as the density fluctuations leading to Rayleigh scattering. The modulation needs to be as weak as possible to avoid the fast depletion of the interrogation pulse, yet a backreflection should be high enough to be detected. The simulation was conducted for uniform and randomly-spaced gratings, both with a fixed Bragg wavelength of 1550 nm. For the random gratings, each grating is 1 mm long and is randomly separated from other gratings by any value within the range from 0 to 5 mm. Since the fibre considered in the simulation is only 60 m long, the fibre loss was neglected.

Fig. 3.5 (a) shows the relative energy lost from the original pulse during its propagation along the fibre distance as a function of the propagation time, and Fig. 3.5 (b) shows the reflected intensity as function of the round-trip time (i.e. the time it takes the light to propagate to the end of the fibre and back to reach the beginning of it). It can be observed in Fig. 3.5 (a) that the lost pulse energy for random gratings is smaller than that of uniform grating. This is relatively intuitive given the fact that for uniform gratings reflections occur all along the fibre, whereas for random gratings there are some fibre portions where reflections do not occur. However, what is quite surprising is the fact that the amount of backreflected intensity (seen in Fig. 3.5 (b)) at the end of the fibre is considerably lower for the case of uniform gratings when compared to random gratings. This result is surprising because the backreflected intensity ratio for uniform and random gratings should be similar to that of the lost energy ratio which is not the case here.

This can be explained using the concept of multiple reflections which, initially, were assumed to be insignificant, given the fact that the gratings under consideration are ultra-weak. According to the first-order Born approximation, when the gratings are extremely weak and short, i.e. the product of the coupling coefficient C_c and the grating length L_g is very small

($C_cL << 1$), the effect of the multiple reflections can be neglected. In our case, however, their effect is not negligible even though the coupling is relatively weak. The length of the grating plays a major role here and causes the Born approximation to break down. Due to the phase difference between the reflection coefficients of the forward- and the backward-propagating waves, higher order reflections interfere destructively with lower order reflections causing a severe decay in the transmission [70]. This can be understood from Fig. 3.5 (b), where we can see a strong decrease in the backreflected signal from the uniform gratings. In the case of the random gratings, the decay rate is much slower. This can be justified by the fact that the randomness of the grating spacing randomises the phase difference between the interfering waves which does not necessarily cause entire destructive interference.

As far as distributed sensing is concerned, random gratings would indeed fit better than uniform gratings because the interrogating temporal pulse can propagate for longer distance before being depleted. For uniform gratings, however, we can expect that the pulses may deplete pretty quickly making it very difficult to conduct long-range sensing. A recently published article [71] showing the limitations of a uniform all-grating fibre for distributed sensing demonstrated similar conclusions to our results presented here in this chapter. The direction of research when it comes to long-range distributed sensing is, therefore, oriented towards the use of random gratings rather than uniform gratings.

3.5 Fibre Bragg grating fabrication

There are different types of fabrication techniques which have been intensively studied in the literature [62]. Two of the most widely-utilised techniques are those which use ultraviolet (UV) laser along with phase masks [60] or point-by-point inscription using infrared (IR) femtosecond lasers [72]. In the following section, we will present an example of the experimental setup that is based on using UV laser and a phase mask for the fabrication of weak Bragg gratings with a slight randomness caused by the uncertainty of the translation stage. The goal of this fabrication exercise is to understand how low of a reflectivity will be able to reach and what is the lowest value of reflection which the interrogator can measure.

3.5.1 Fabrication setup

The setup utilised for the FBG fabrication is depicted in Fig. 3.6. The laser used is an Innova 300C FreD coherent continuous-wave (CW) laser that allows grating inscription in the deep-ultraviolet (UV) region (244 nm of wavelength) with powers up to 100 mW. In our case, we care about minimising the power as much as possible, so that we can obtain weak gratings with very low reflectivity. Therefore, the laser power is set to 50 mW, because the use of a lower value makes the laser unstable. The laser light is directed towards a first mirror, then a second to pass through mechanical shutter. This shutter is controlled using a computer program, where a parameter is set to pass or reject the light beam. This parameter determines the exposure time of the laser beam on the fibre. When the light beam passes through the
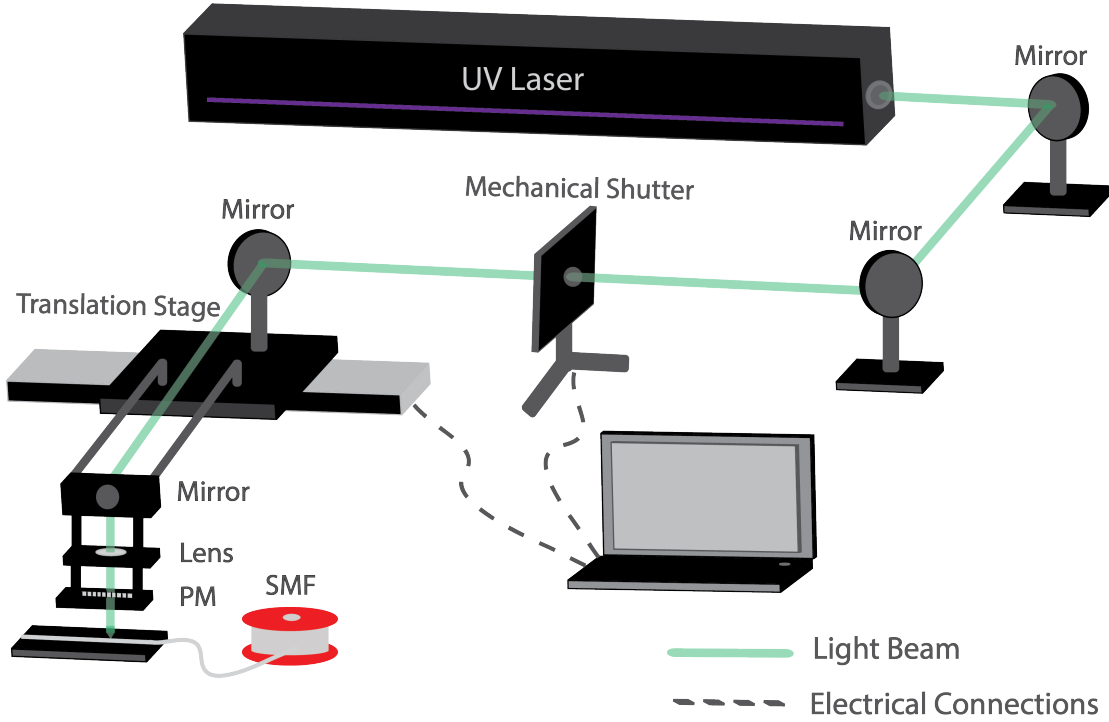
Figure 3.6 – Experimental setup for the fabrication of fibre Bragg gratings; PM: phase mask.

mechanical shutter, it gets reflected by a mirror that is fixed on a translation stage. The stage is also manipulated with a program to be able to control the speed of the translation. The speed was set to 1 mm/s. It should be noted that the speed does not affect the exposure time in our case, because the stage stops when the gratings are written. However, the speed should not be set to be too fast, because it might slightly alter the stopping position due to the fast movement. The light is then reflected by another mirror and gets directed towards a plano-convex lens with a focal length of 2.5 cm, which focuses the laser beam onto a phase mask (PM) placed over the fibre. It should be noted that we did not always focus the beam in the focal length, and this is because we wanted to minimise the intensity as much as possible. The fibre was connected to a commercial optical frequency-domain reflectometer (OFDR), namely the LUNA OVA 5100 in reflection mode to be able to monitor the fabrication in real-time with a spatial resolution of 1.59 pm. We have tried several exposure times, so that we can know the minimum reflection that can be measured by the interrogation system. 10 cm grating arrays of approximately 24 gratings with a period of 4 mm ($\Lambda_{\text{Bragg}} = \frac{\Lambda_{\text{PM}}}{2}$) are imprinted inside 0.5 m pieces of hydrogenated germanium-doped standard silica single-mode fibres (SMF).

The backreflected traces of the different gratings along with their spectra can be seen in Fig. 3.7. The left figure shows backreflected OFDR traces for each of the fabricated gratings for the different exposure times: (a) 30 ms, (b) 50 ms, and (c) 70 ms. Each grating is about 1 mm long and separated by 3 mm from the following one. We can see from Fig. 3.7 (d) showing the spectra measured with an optical spectrum analyser (OSA) (see Fig. 3.8 (b)) that the gratings
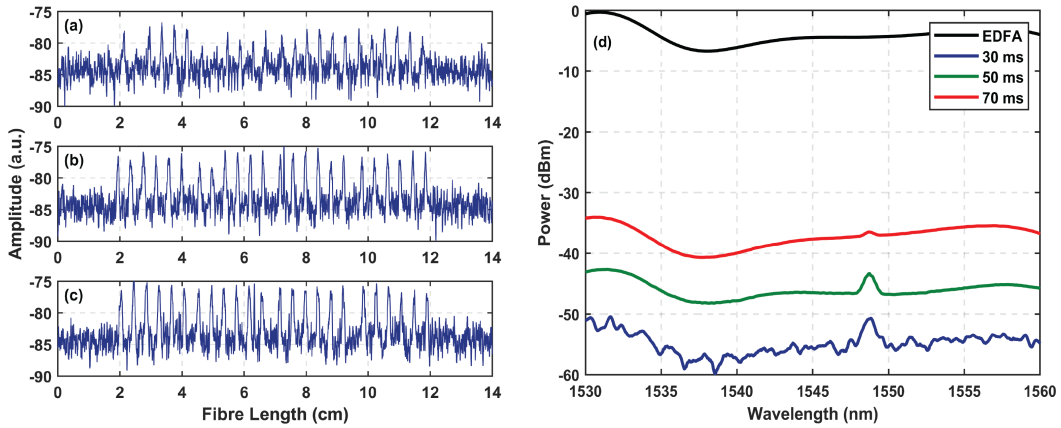
Figure 3.7 – Fibre Bragg grating arrays of about 24 gratings for different exposure times; Left figure: OFDR traces showing the backreflected amplitude versus the fibre length: (a) 30 ms, (b) 50 ms, and (c) 70 ms; Right figure: (d) Spectra of the fabricated gratings, where the solid black curve represents the transmitted spectrum of the EDFA.

have a peak at a wavelength approximately equal to λ_B = 1548.5 nm. The OSA was used with a resolution of 0.2 nm and no time-averaging. As observed, the longer the exposure time, the wider is full width at half maximum (FWHM) bandwidth of the grating peak. The reflectivities R of the fabricated gratings were calculated from the peak of the reflected signal R_p below the transmitted signal (the EDFA reference signal used as the input source as shown in Fig. 3.8 (a)) using the following equation [62]:

$$R = 10^{-\frac{R_p}{10}} \tag{3.19}$$

Using Eq. 3.9 and the values calculated using Eq. 3.19, we can calculate the modulation index strength according to the reflectivity values obtained from the experiment. The values for the reflectivities, the modulation indices, and the bandwidths corresponding to the different exposure times are summarised in table 3.2. We can see that the reflectivity for the gratings fabricated during an exposure time of 30 ms is relatively low. However, it seems that if we require longer lengths, the gratings should then have even weaker modulation indices.

Exposure time	Reflectivity	Δn_0	FWHM
30 ms	-46 dB ($2.5 \times 10^{-3}\%$)	2.5×10^{-8}	0.96 nm
50 ms	-39 dB ($1.3 \times 10^{-2}\%$)	5.6×10^{-8}	1.2 nm
70 ms	-32 dB ($6.3 \times 10^{-2}\%$)	1.2×10^{-7}	1.4 nm

Table 3.2 – Reflectivity, modulation index strengths and FWHM values for the fabricated fibre Bragg gratings.

49
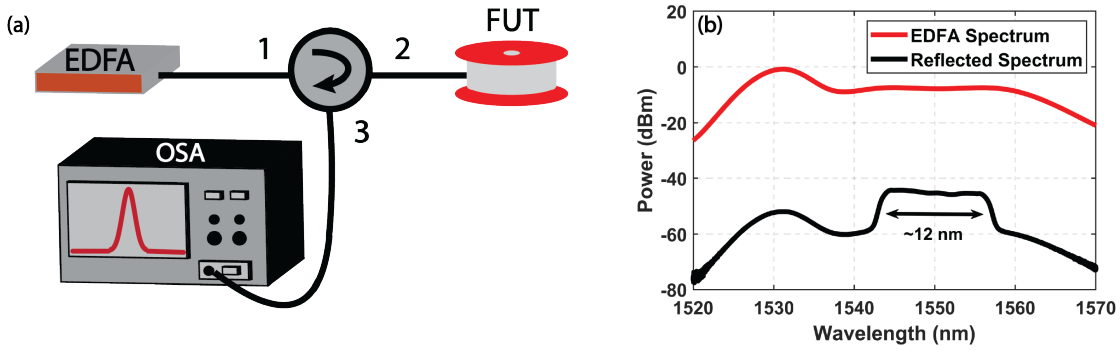
Figure 3.8 – (a) Experimental setup for the measurement of the backreflected grating spectra; (b) Graph showing the enhancement bandwidth of the REF expanding over 12 nm for a 10 m sample of the fibre.

3.6 Directional backreflection-enhanced fibre

In the previous section, we mentioned two types of random gratings, but we only investigated one of them, namely randomly-spaced gratings with a fixed centre Bragg wavelength. The other type deals with randomly-spaced gratings which are chirped whose common purpose is to yield a larger reflection bandwidth. The chirping additionally results in a lower back-reflected signal when compared to non-chirped gratings. An example of such kind of fibres was proposed in [73, 74]. In that work, *Westbrook et al.* presented a reflection-enhanced fibre (REF) using a standard single-mode fibre (SMF) which has overlapped chirped Bragg gratings inscribed in its core. Accordingly, a ~10 dB *directional* enhancement over a bandwidth of ~12 nm from 1544 nm to 1556 nm was achieved, whereas the optical losses were measured to be below 0.7 dB/km [75].

We have seen that there is no need to insist on fabricating uniform gratings, as random gratings will yield better results due to the severe destructive multiple reflections occurring in the case of uniform gratings. Besides, random gratings are fabricated more easily, and since there is already a commercial and mature fibre that serves our purpose, we opted for one such fibre [75] for our experimental demonstration showing the distributed temperature measurement presented in Chapter 5. The REF used in our experiments is about 100 m long and has an overall propagating loss of 0.7 dB/km. It has an enhancement of 12 nm in the backreflected spectrum which is shown in Fig. 3.8 (b) measured with an OSA using a resolution of 2 nm and no time-averaging. The reflectivity R measured from the spectrum is about -53 dB (4.9×10^{-4}%) for a 10 m sample of the fibre. Those fibres offer the directional backreflection which we need to improve the performance of Rayleigh-based sensors. Due to the directionality, a higher backreflection is yielded which is almost 10× higher than the Rayleigh back-scattering level. This enhanced backreflected signal triggered our curiosity to investigate its effect on the SNR enhancement and on the overall measurement accuracy for Rayleigh-based systems. So far, no figure-of-merit has been demonstrated for Rayleigh-based systems that can evaluate the system by means of a simple expression. Therefore, we present a thorough study on finding a

clear relationship between some of the fundamental system parameters. The coming chapters deal with this theoretical model which we confirm with experimental results in form of a comparison between the performances of a standard SMF and the REF.

4 Frequency shift uncertainty in direct-detection Rayleigh-based systems

4.1 Introduction

In the previous chapter, we discussed the difference between scattering in many directions and directional scattering, and how the directionality of the backreflection can result in a significant signal enhancement. For optical fibre sensors, a backreflected signal enhancement is always desired, as it directly impacts one of the most crucial parameters for any sensing system, namely the signal-to-noise ratio (SNR). Improving the SNR of a sensing system can dramatically scale up its performance in terms of sensing range, accuracy of the measurement, speed of acquisition, spatial resolution, along with others [76]. A few methods employed for this purpose are conventional temporal averaging, spatial averaging [77], increasing the power of the launched pulse directly or with pulse coding achieving an SNR enhancement of 8 dB [78, 79], enhancing the back-scattered signal through Raman amplification [80, 81], data processing methods [82, 83] increasing the SNR by 8.4 dB and 8.5 dB, respectively, and enhancing the back-scattered light by manipulating the scattering properties of the fibre [58, 84, 85] achieving an SNR as high as ~ 35 dB [86]. Alongside the prodigious effort made to achieve SNR enhancement, several works extensively discussed the possibility to resolve the physical alterations at the sub-metre scale which will substantially improve the accuracy in the determination of the exact location of the external perturbation [87, 88].

Despite the tremendous work that has been carried out aiming at ameliorating the system performance of Rayleigh-based DOFS through interdependent parameters such as SNR and spatial resolution, a proper relationship pertaining the dependency of these parameters on the measurement frequency shift (FS) uncertainty has not been properly addressed yet. For Brillouin-based DOFS, a comprehensive model has been derived to estimate the FS uncertainty of the Brillouin gain spectrum with respect to various measurement parameters [89]. The derived model is valid for any system for which the peak value of a resonance is evaluated through quadratic least-square fitting. In the case of coherent Rayleigh-based DOFS, for instance in direct-detection frequency-scanned φ-OTDR systems, the most widely and commonly-used method to estimate the relative value of the FS between reference and mea-

surement signals is cross-correlation [90–92]. Cross-correlation is a standard method utilised for delay estimation in sonar and radar systems [93–95], and is also adopted in other coherent Rayleigh-based DOFS [96]. The presence of unavoidable additive noise in the traces that are being correlation fundamentally limits the performance of the cross-correlation estimator and leads to uncertainty in the estimated FS. Besides, other experimental parameters, such as spatial resolution, can also influence the accuracy of estimation.

We will firstly have a thorough explanation of the working principle of direct-detection frequency-scanned phase-sensitive optical time-domain reflectometry (φ-OTDR), then we will carry on by presenting the experimental results along with the theoretical confirmation.

The study presented in this chapter is published in [97] and permission of the copyright holder was granted for the work to be reproduced here.

4.2 Direct-detection frequency-scanned φ-OTDR

4.2.1 Working principle

General concept of φ-OTDR

To model a φ-OTDR system mathematically, we start by assuming that we launch a linearly polarised interrogating rectangular light pulse of width τ_{pw} into an optical fibre. Only the light scattered back along the fibre axis will be taken into consideration. The inhomogeneities in the material density of the fibre scatter the incident light and result in an additional phase change in the scattered field. Assuming that the initial optical field at the beginning of the fibre $z_0 = 0$ is $\overrightarrow{E_{\mathrm{in}}}$, we can express the complex amplitude vector of the light reflected from a single scattering point located at a position z as:

$$\overrightarrow{E_{\mathrm{sc}}}(z) = \overrightarrow{E_{\mathrm{in}}} \alpha_{\mathrm{BR}}(z) e^{-\alpha z + j\varphi(z)} \tag{4.1}$$

where α, $\alpha_{\mathrm{BR}}(z)$, and $\varphi(z)$ are the fibre attenuation coefficient, the backreflection coefficient and the additional phase change experienced by the incident light, respectively. The phase change is:

$$\varphi(z) = \int_0^z k(x)\mathrm{d}x = 2\pi \frac{f}{c} \int_0^z n(x)\mathrm{d}x \tag{4.2}$$

where k is the local propagation constant of the fibre and c is the light speed in vacuum. From Eq. 4.2 we can see that the scattered light $\overrightarrow{E_{\mathrm{sc}}}(z)$ at position z is dependent on the optical frequency f and the refractive index distribution $n(z)$ in the range [0, z].

Following the one-dimensional strategy for the simplicity of the modelling, the optical fibre can be regarded to be consisting of uniformly distributed scatterers of fixed size Δz, but with random density changes and thus refractive index fluctuations. The refractive index of each

scatterer is assumed to be $n_m = n_{\text{ave}} + \Delta n_m$, where n_{ave} (~ 1.46) is the average refractive index of the fibre and Δn_m represents the index fluctuation, which is in the order of 10^{-8}. We can, therefore, rewrite Eq. 4.1 as a discrete summation rather than a continuous integral, such that the electric field of the light that is reflected from the mth scatterer is:

$$\overrightarrow{E_{\text{sc}}}(z_m) = \overrightarrow{E_{\text{in}}} \alpha_{\text{BR}}(z_m) e^{-\alpha m \Delta z + j2\pi \frac{f}{c} \sum_{i=1}^{m} n_i \Delta z} \tag{4.3}$$

For a pulse width of τ_{pw}, the back-scattered signal received at the fibre beginning at time t is the summation of the individual contribution from every discrete location:

$$\overrightarrow{E_{\text{sc}}}(t) = \sum_{m=1}^{N} \overrightarrow{E_{\text{in}}} \alpha_{\text{BR}}(z_m) e^{-2\alpha m \Delta z + j2\pi f(t-t_m)} \text{rect}\left(\frac{t-t_m}{\tau_{\text{pw}}}\right) \tag{4.4}$$

$$\text{rect}\left(\frac{t-t_m}{\tau_{\text{pw}}}\right) = \begin{cases} 1, & 0 \leq \frac{t-t_m}{\tau_{\text{pw}}} \leq 1; \\ 0, & \text{otherwise.} \end{cases} \tag{4.5}$$

where $N = \frac{L_{\text{tot}}}{\Delta z}$ stands for the number of scatterers over the fibre length L_{tot}, and the factor 2 in Eq. 4.4 accounts for the light completing a round-trip in the fibre. The time delay which is calculated as the round-trip time from the beginning of the fibre to the mth scattered point is accordingly given by:

$$t_m = 2 \sum_{i=1}^{m} n_i \frac{\Delta z}{c} \tag{4.6}$$

The optical power at the photo-detector then becomes [98]:

$$\mathbb{P}(t) = |E_{\text{sc}}(t)|^2 = \mathbb{P}_1(t) + \mathbb{P}_2(t) \tag{4.7}$$

$$\mathbb{P}_1(t) = \sum_{m=1}^{N} E_{\text{in}}^2 \alpha_{\text{BR}}^2(z_m) e^{-2\alpha m \Delta z} \text{rect}\left(\frac{t-t_m}{\tau_{\text{pw}}}\right) \tag{4.8}$$

$$\mathbb{P}_2(t) = \tag{4.9}$$

$$2 \sum_{m=1}^{N} \sum_{k=m+1}^{N} E_{\text{in}}^2 \alpha_{\text{BR}}(z_m) \alpha_{\text{BR}}(z_k) \cos(\varphi_{\text{mk}}) e^{-2\alpha(m+k)\Delta z} \text{rect}\left(\frac{t-t_m}{\tau_{\text{pw}}}\right) \text{rect}\left(\frac{t-t_k}{\tau_{\text{pw}}}\right)$$

where $\varphi_{\text{mk}} = 2\pi f(t_m - t_k)$. The subtotal term $\mathbb{P}_1(t)$ in Eq. 4.8 represents the sum of independently scattered waves and is only dependent on the input power as well as the fibre loss, but shows no dependence on the phase of the light, thus exhibits no dependence on the strain and temperature of the fibre or the frequency of the light. $\mathbb{P}_2(t)$ is, therefore, the term of interest here, as it accounts for the interference between the individual light waves scattered from distinct scatterers within the input pulse width, and causes the jagged appearance of a typical φ-OTDR trace. The quantity φ_{mk} denotes the phase difference between the back-scattered waves from the mth and k^{th} scatterer, and it can be written as:

$$\varphi_{\text{mk}} = \frac{2\pi f \sum_{i=m}^{k} n_i \Delta z}{c} \tag{4.10}$$

Environmental perturbations resulting in temperature and/or strain variations will change φ_{mk}, yielding a different interference intensity pattern $\mathbb{P}_2(t)$, thus the notion of the "phase-sensitive" technique. From Eq. 4.10 we can see that φ_{mk} is proportional to the laser frequency f, the local refractive index n_i, and the spacing Δz between the scatterers. The scatterers are solidified in the fibre once it is manufactured thus the spaces between scatterers are fixed for a given fibre. Temperature and strain will induce a linear change of the fibre refractive index.

Concept of frequency-scanned φ-OTDR

After having presented the general concept of φ-OTDR, we would now like to focus entirely on direct-detection frequency-scanned φ-OTDR. This technique retrieves the phase information from the back-scattered light at each position in the fibre through laser frequency (f) scanning with a specified step size (Δf) [98] (Fig. 4.1 (a)) followed by data processing. The methodology consists of interrogating the fibre with highly coherent laser pulses, with a pulse width determined by the desired spatial resolution of the measurement. The period of the pulses is made greater than the round-trip time of the pulse in the fibre, so that the pulse optical carrier frequency is scanned over a preset frequency range. The statistical distribution of coherent Rayleigh back-scattered intensity follows an identical process as the generation of chaotic light, formally equivalent to a random walk process, so that the normalised back-scattered intensity pattern received at the photo-detector follows an exponentially decaying distribution [99]. The back-scattered optical intensity measured by the photo-detector for each fibre location is thus a function of time (or equivalently a function of distance, as shown in Fig. 4.1 (b)), and the pulse laser optical frequency. Accordingly, a 2-D array is constructed having the columns as the different positions throughout the sensing fibre, and the rows as the scanned frequencies, which is illustrated on the upper part of Fig. 4.1 (c). The intensity of the light received at the photo-detector corresponding to each pulse at a specified frequency of the laser constructs an irregular time-domain trace along the whole length of the fibre (Fig. 4.1 (b)). Such a trace corresponding to a particular frequency and a row in the array in Fig. 4.1 (c) can be considered as a fingerprint of the fibre as it is static under constant environmental conditions.

The information in the array can be also interpreted column-wise and it similarly appears like a jagged trace, representing the coherent Rayleigh spectral response at a given position (shown in the lower portion of Fig. 4.1 (c)) and will be designated hereafter as the *artificially-constructed signal*. Indeed this signal is a spectral response and is not measured directly. It is actually constructed from separate data points from the time-domain traces of different frequencies, and thus we use the terminology "artificially-constructed".

Optical phase difference created by the localised external perturbations changes the pattern of the artificially-constructed trace at this specified location. This is because the optical path length of the propagating light is changed as a consequence of the variation of refractive index. This causes a phase change on each elementary wave resulting in an effect equivalent to a frequency change. This phase difference can thus be fully restored through an appropriate optical FS of f, which then provides a direct indication of the local refractive index change
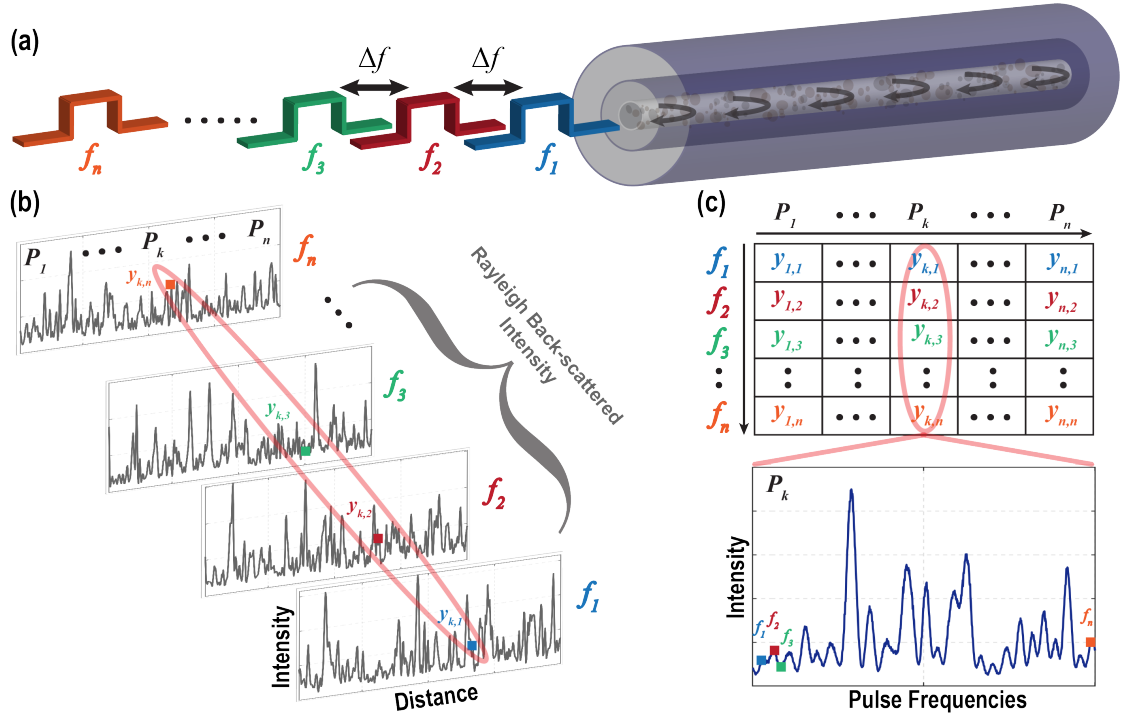
Figure 4.1 – Concept of frequency-scanned φ-OTDR: (a) Schematic showing optical pulses at different frequencies separated by a frequency scan step of Δf shot in a standard single-mode fibre one at a time, (b) Rayleigh back-scattered intensity time-domain traces corresponding to the different pulse frequencies entering the fibre, (c) Upper figure: Experimentally obtained 2-D array containing the different positions along the sensing fibre (columns) for different frequencies in the scanning range (rows); (P_1-P_n: positions, f_1-f_n: frequencies); Bottom figure: Back-scattered intensity corresponding to a specific position in the fibre for all the different pulse frequencies.

at that location. One of the most commonly-used methods in φ-OTDR to determine the FS caused by the localised external perturbation acting along the fibre, is to compute the cross-correlation function ($\hat{R}_{x_r,x_m}$) between the artificially-constructed reference trace (x_r) and a subsequent measurement trace (x_m) which is given by [87]:

$$\hat{R}_{x_r,x_m}(\delta f) = \frac{1}{F} \sum_{i=1}^{F} x_r(f_i)\, x_m(f_i - \delta f) \tag{4.11}$$

These signals are formed by the optical intensity values of the φ-OTDR time-domain signals at one particular fibre position for all the pulse frequencies in the scanning range (depicted in the lower portion of Fig. 4.1 (c)). F is the number of frequencies in the total frequency-scan range of the laser, δf is the FS that has to be determined. The value of δf that maximises the above function, designated as $\delta f^{\max}$, provides a measured value of the FS. The accuracy with which the FS can be estimated is influenced by a number of parameters. Hence, the uncertainty in the estimation (FS uncertainty, σ) can be considered as the difference between

the measured value ($\delta f^{\max}$) and the true value ($\delta \hat{f}^{\max}$) estimated independently and is not taken from the same set of measurements of the FS which can be formulated as:

$$\sigma = \sqrt{\frac{1}{I} \sum_{m=1}^{I} (\delta f_{x_{r,m}}^{\max} - \delta \hat{f}_{x_r}^{\max})^2} \tag{4.12}$$

where I is the total number of measurements/iterations. In the case when the true value is not independently known, but is estimated from the same experimental sample of data, the normalising factor will be $\frac{1}{I-1}$ instead.

It should be noted that the signals used for cross-correlation are artificially constructed, and that there is no mathematical difference whatsoever between considering these signals to be physically in any particular domain. They can be simply regarded as signals with a specific number of samples in no defined domain, indicating that the physical quantity represented on the x-axis is completely irrelevant for the estimation. Consequently, the FS estimation can be approached in a similar manner as a time-delay estimation problem just like in the case of sonar and radar systems [93–95].

4.2.2 Experimental setup

The experimental setup we employ in this work is a direct-detection frequency-scanned φ-OTDR which is used to verify the expression for the measurement uncertainty which will be presented later on in the coming sections. The functionalities of all system components along with the devices used in the experimental setup will be thoroughly elaborated in this section.

In the experimental setup displayed on Fig. 4.2, a 1 MHz linewidth distributed feedback (DFB) continuous-wave (CW) laser with a centre wavelength at 1550 nm is used as the coherent light source of the φ-OTDR interrogation system utilised in this work. The stability of the
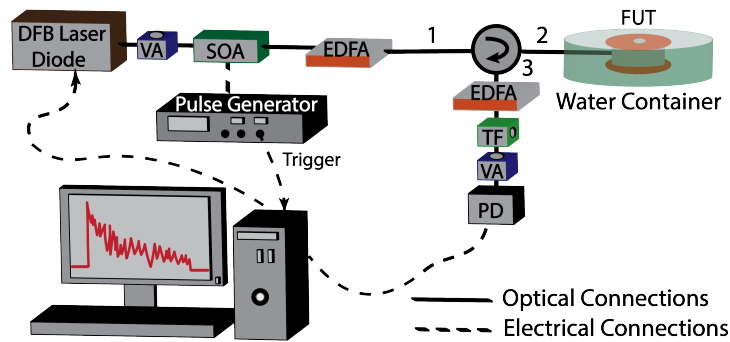
Figure 4.2 – Experimental setup of a frequency-scanned φ-OTDR using direct detection (DFB: Distributed feedback laser, SOA: Semiconductor optical amplifier, EDFA: Erbium-doped fibre amplifier, TF: Tunable filter, VA: Variable attenuator, PD: Photo-detector, FUT: Fibre Under Test).

laser is highly essential to avoid significant laser frequency drifts that could lead to additional uncertainty in the FS estimation. This, however, can be mitigated by technical improvement, such as laser stabilisation by locking, or by performing a fast measurement to make laser drifting negligible and measuring precisely the laser frequency when data is acquired. External intensity modulation of the CW light is achieved by means of a high extinction ratio (ER) semiconductor optical amplifier (SOA) leading to the generation of optical pulses, with desired spatial resolution for the measurement. The power of the pulse is then amplified by an Erbium-doped fibre amplifier (EDFA) followed by a variable attenuator, which serves to limit the power directed into the fibres to avoid nonlinear optical effects such as modulation instability.

The light then enters port 1 of a circulator, and passes through port 2 to travel into the fibre under test, which in this case is a ~ 100 m single-mode fibre. A second amplification stage is required to boost the back-scattered signal before passing through a 1 nm optical filter, which is necessary to filter out the ASE noise generated by the EDFAs. The signal is then captured by a 125 MHz photo-detector, and acquired by a data acquisition card (DAQ) at a sampling rate of 500 MS/s.

The frequency sweep of the interrogating pulse is carried out by remotely controlling the laser driver, which in turn tunes the current of the DFB laser. The current scan is performed over 10 mA (3.2 GHz frequency range) with a step of 0.01 mA (3.2 MHz frequency step). Since there is no external perturbation applied to the fibre in the present scenario, the frequency scan range is limited to 3.2 GHz. It should be pointed out that the fibre is immersed in a large water bath to minimise any environmental influences occurring during the measurement.

4.2.3 Calculation of the SNR in a φ-OTDR system

The SNR of a trace having an intensity distribution following an exponentially decaying probability density function (PDF) can be estimated by the following equation [100, 101]:

$$M = \frac{\mu}{\sigma_n} \tag{4.13}$$

where M is the SNR, μ and σ_n are the mean and the standard deviation of the signal, respectively, for several consecutive measurements. Due to the jagged noise-like intensity pattern of the time-domain trace of a φ-OTDR system governed by an exponential PDF, Eq. (4.13) can be used for the rough estimation of the SNR since the limited sample leads to large uncertainties in the calculation of the mean μ. Here, we propose a different approach and compare its result with that of the statistical estimation to know if the conventional method used for incoherent OTDR systems is also applicable in the case of a φ-OTDR system. Using an incoherent OTDR setup (as illustrated in the left figure of Fig. 4.3), we calculate the backreflection coefficient of the fibre using the following equation:

$$\alpha_{\mathrm{BR}} = \frac{P_{\mathrm{BR}o}/P_{\mathrm{in}o}}{R_{\mathrm{sp}}} \tag{4.14}$$

59

where α_{BR} is the backreflection coefficient (in m^{-1}) measured from the signal received at the input end of the fibre and is assumed constant along the whole fibre, P_{BRo} is the back-scattered power obtained from the OTDR trace (as shown in the right figure of Fig. 4.3), $P_{in o}$ is the input peak power to the fibre, and R_{sp} is the spatial resolution (in m) of the OTDR system (which is equivalent to half of the physical length of the interrogation pulse launched into the fibre). It should be noted that α_{BR} is the product of the absolute value of the Rayleigh back-scatter coefficient and the re-capture factor. In the case of a standard single-mode fibre, the α_{BR} is found to be -72.7 dB/m. The same method is utilised to calculate the α_{BR} of a different type of fibre under test as illustrated in Fig. 4.3. For the REF mentioned in section 3.6, α_{BR} is calculated to be -64.1 dB/m. The difference in the value of α_{BR} is explained by the fact that the core of the REF has been subjected to refractive index manipulation to enhance the back-scattering as already discussed earlier in section 3.6. Thus, α_{BR} serves as a metric parameter for a given fibre under test.

Once the backreflection coefficient of the fibre under test is known, the backreflected power ($P_{BR\varphi}$) from the φ-OTDR system (depicted in Fig. 4.2), at a distance z in the fibre assuming that the backreflection coefficient is constant along the entire fibre, can be simply calculated using Eq. 3.1 which we will repeat here for convenience [14]:

$$P_{BR\varphi} = P_{in\varphi}\, \alpha_{BR}\, R_{sp} \exp\left(-2\alpha z\right) \tag{4.15}$$

where α is the attenuation coefficient of the fibre, and the factor 2 accounts for the round-trip distance that the light travels to reach the receiver at the input of the fibre. Using the conversion gain of the photo-detector utilised in the setup along with the gain and loss in optical power caused by the different optical components in the setup, the actual power reaching the photo-detector is determined. The value of the power obtained is the optical power (which is equivalent to the electrical voltage through the conversion gain of the photo-detector).
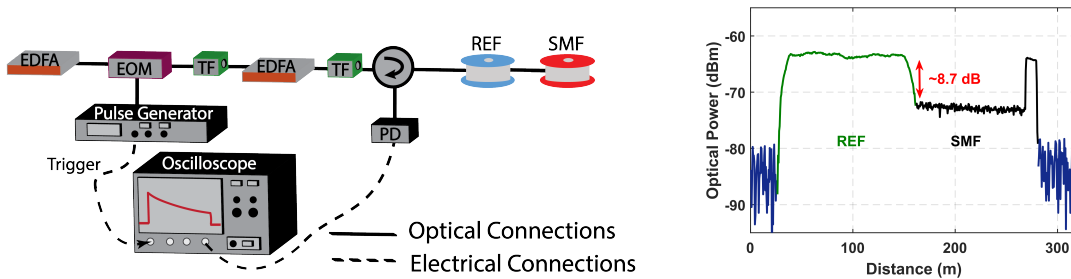
Figure 4.3 – Left figure: Incoherent OTDR experimental setup.; Right figure: Back-scattered OTDR trace in terms of back-scattered optical power as a function of the fibre distance for two sets of fibres with different SNR, namely the REF and a single-mode fibre (SMF). Note: The blue traces before and after the fibres represent the noise floor. The spike before the noise floor is the reflection at the fibre end.

Different types of noises (such as optical and electrical noises) generated in the system will be additive noises to the signal, and can be quantified by computing the standard deviation, at each position in the fibre, of a number of time-domain traces. This value quantifies the overall noise electrical voltage in the system, which when multiplied with the conversion gain of the photo-detector results in an equivalent noise optical power value. Thus, taking the ratio between the optical signal power and the noise power will yield the SNR (M_o) of the system. It should be mentioned that the SNR (M_e) is calculated as the integrated square of the electrical voltage. This means that the SNR calculated in this section (i.e., M_o) is equivalent to $\sqrt{M_e}$.

The proposed method of calculation of the SNR for a φ-OTDR system presented earlier is compared to the conventional method of SNR estimation for a trace following an exponential PDF. As illustrated in Fig. 4.4, the calculated SNR from the φ-OTDR time-domain traces using Eq. (4.19) and the theoretical model resulted in nearly the same values. This can be explained as follows: in the case of an OTDR, since an incoherent light source is used, the interrogating input pulse will have a short coherence length unlike the coherent light pulse in the case of the φ-OTDR. This makes the PDF of the OTDR time-domain trace follow a Gaussian distribution with significantly lower variance [102, 103]. Thus, the time-domain trace of the OTDR appears to be like in Fig. 4.3, with the mean value of the time-domain trace obtained from the peak of the Gaussian distribution. For the case of the φ-OTDR, the interrogating input pulse is highly coherent, making the time-domain trace follow an exponentially decaying PDF. The expected value (mean) of the exponentially decaying PDF of the time-domain trace will give the average intensity of the back-scattered light. This implies that the mean value of the back-scattered intensity obtained from the time-domain traces of the OTDR and the φ-OTDR are equivalent. Thus, the SNR calculated using Eq. (4.13) or the proposed model will yield nearly the same result. The comparison assures that Eq. (4.13) can be followed for a rough estimation of the SNR even for a jagged intensity profile like in the case of a φ-OTDR system.
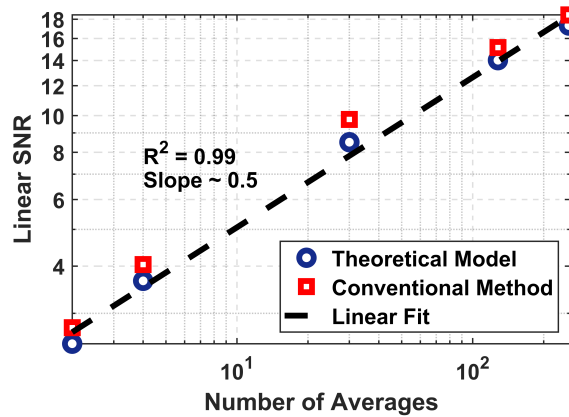
Figure 4.4 – Log-log plot of SNR versus number of averages; blue dashed line: calculated SNR using the theoretical model, red squares: calculated SNR using the mean value of the jagged time-domain trace divided by the standard deviation of 20 time-domain traces.

4.3   Theoretical estimation of the measurement FS uncertainty

4.3.1   Measurement FS uncertainty for a rectangular input pulse

Due to the presence of inevitable measurement noises, the cross-correlation estimator comprises uncertainty which needs to be taken into consideration during the estimation. All sources of noise in the system can be considered as zero-mean additive white Gaussian noise to the original signal. In turn, in this work we solely address uncertainty due to system noises. Any additional ambiguities in the estimation, like significant laser frequency drifting or large errors resulting from correlation for instance, do not result from noise and, hence, have to be addressed independently as elaborated in great detail in one of the previous studies [87]. One important point to highlight here is that the expression which will be presented in Eq. 4.16 is subject to the assumption that the correlation window/frequency scan range is chosen to be large enough to cover the entire range of external changes and to avoid the occurrence of large errors [87]. For example, if a 10 degree temperature change is applied to the fibre, the correlation window/frequency scan range should be chosen to be around 13 GHz (keeping in mind that 1 degree of temperature change causes around 1.3 GHz of frequency shift). It is also worth noting that parabolic fitting is applied to the cross-correlation peak for the frequency shift determination, and the uncertainty induced by the fit can be calculated using the rigorous model presented in [89].

The estimated uncertainty in the FS determination is given by Eq. (4.12). Since the Rayleigh back-scattering can be considered as a random process [100, 104, 105], a probabilistic model (see Appendix A) can be followed to obtain an expression for the uncertainty in the determination of the FS using cross-correlation as presented in [106–110] in the case of time-domain radar signals. Eventually, considering the mathematical equivalence between the time-delay estimation in the case of the sonar and the radar systems and the FS estimation in the present scenario, the expression for the uncertainty with which the FS can be determined is given as
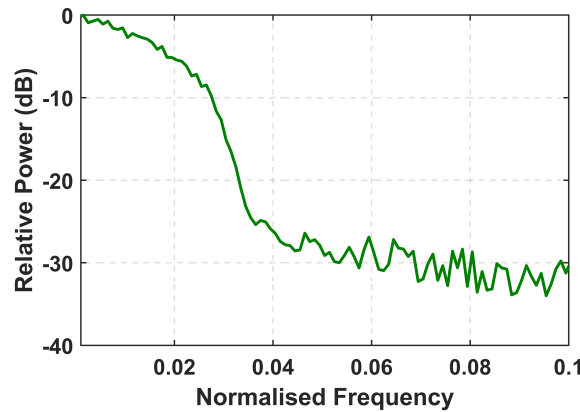
Figure 4.5 – Power density of the signal under consideration as a function of the normalised frequency.

[109, 111]:

$$\sigma = \frac{1}{\beta \sqrt{M_e}} = \frac{1}{\beta M_o} \tag{4.16}$$

where M_o represents the SNR calculated using the optical power and the parameter β represents the square root of the second moment β^2 of the power density $|U(f)|^2$ of the artificially-constructed signal $u(x)$ expressed as follows:

$$\beta^2 = 4\pi^2 \frac{\int f^2 |U(f)|^2 df}{\int |U(f)|^2 df} \tag{4.17}$$

where f is the laser frequency and $U(f)$ is the Fourier transform of $u(x)$.

It should be noted that the SNR for the optical power of the signal is equivalent to the square root of the SNR of the electrical power M_e. In the present case of direct-detection frequency-scanned φ-OTDR, the SNR (M_o) is calculated using the power of the optical signal received at the photo-detector. Consequently, the dependence of σ on the SNR is inverse as shown in Eq. (4.16). The handling of the artificially-constructed signal, and the appropriate usage of Eq. (4.16) for the case of direct-detection frequency-scanned φ-OTDR is addressed in great detail under section 4.3.2.

The parameter β (mentioned in Eq. (4.16)) can be solved either computationally or analytically. Prior knowledge of the shape of the power density of the signal under consideration is not required when the computational approach is followed. However, to obtain an analytical solution for β, an expression for the power density needs to be formulated. In a previous work presented in [112], the electrical power spectrum of the back-scattered light in direct-detection φ-OTDR (which can be calculated from the auto-convolution of the optical power density of the input pulse) for rectangular and sinc input pulses are given theoretically and validated experimentally. In the case of a rectangular input pulse, the analytical expression for the electrical sinc-shaped power density is given in [112]. However, this expression cannot be used in this study due to the fact that the signal under consideration for estimating the FS using cross-correlation is not the direct time-domain trace. In addition, the time-domain signals and the artificially-constructed signals are not related by ergodicity which means that the power densities will not yield the same distribution. Thus far, the power density of the artificially-constructed signal used in cross-correlation in direct-detection frequency-scanned φ-OTDR has not been investigated in any of the previous works. It is found that the power density for this artificially-constructed signal (with a rectangular input pulse to the fibre) has a triangular shape (illustrated in Fig. 4.5). The triangular shape, however, cannot be seen on the graph due to the dB-scale on the y-axis. The graph shows the summation of the power densities at each fibre position creating a smooth curve that manifests the actual shape of the power density. It should be noted that the use of the normalised frequency for the x-axis is

for the generality of the concept. The axis is simply normalised by the step size (Δf) of the artificially-constructed signal. The concept of normalised frequency will be further utilised and elaborated in section 4.3.2. The triangular-shaped power density is expected in this case because the artificially-constructed signal can be assimilated to a time-domain signal obtained using a sinc input pulse. Therefore, the power density of the artificially-constructed signal is logically given by the auto-correlation of a rectangular spectrum (for a sinc input pulse) which is triangular-shaped.

An analytical expression for β, given in Eq. (4.16), for a triangular-shaped power density is thus obtained similarly to [113], and takes the following form:

$$\beta = \frac{2\pi\tau_{\text{pw}}}{\sqrt{6}} \tag{4.18}$$

where τ_{pw} is the pulse width (full width at half maximum) of the rectangular input pulse, which is also equivalent to the bandwidth of the power density of the artificially-constructed signal under consideration. Thus, the analytical solution for the FS uncertainty of a direct-detection frequency-scanned φ-OTDR system with a rectangular input pulse is given by:

$$\sigma = \frac{\sqrt{6}}{2\pi\tau_{\text{pw}}M_o} \tag{4.19}$$

The above equation relates, in the case of a rectangular input probe pulse, the uncertainty in the FS estimation to the pulse width and the SNR of the signal.

4.3.2 Calculation of the measurement FS uncertainty computationally

As mentioned earlier, the traces used for performing the cross-correlation are signals which are artificially formed from the back-scattered optical intensity values for each fibre position as a function of all the pulse frequencies within the scanning range (lower part of Fig. 4.1 (c)). However, it should be highlighted that throughout this study, no domain is defined for these artificially-constructed signals, and they are considered as signals with a specific number of samples. An example of such an artificially-constructed signal is shown in Fig. 4.6 (a). In the present experiment, the total number of rows in the acquired 2-D array (representing the total number of frequencies that are scanned in the frequency range) (upper part of Fig. 4.1 (c)) is 1000. Therefore, the signal depicted in Fig. 4.6 (a) has the same number of points as the number of frequencies in the scanning range which is 1000 samples. From the localised power density (Fig. 4.6 (b)) of this constructed signal depicted in Fig. 4.6 (a), the term β in Eq. (4.16) is calculated. The x-axis of Fig. 4.6 (b) is expressed in the units of normalised frequency (cycles/sample) where the axis is basically normalised by the step size (Δf) of the artificially-constructed signal. Utilising the normalised frequency terminology here is merely to present the concept in a rather simple and general manner that is independent of the step size. This is
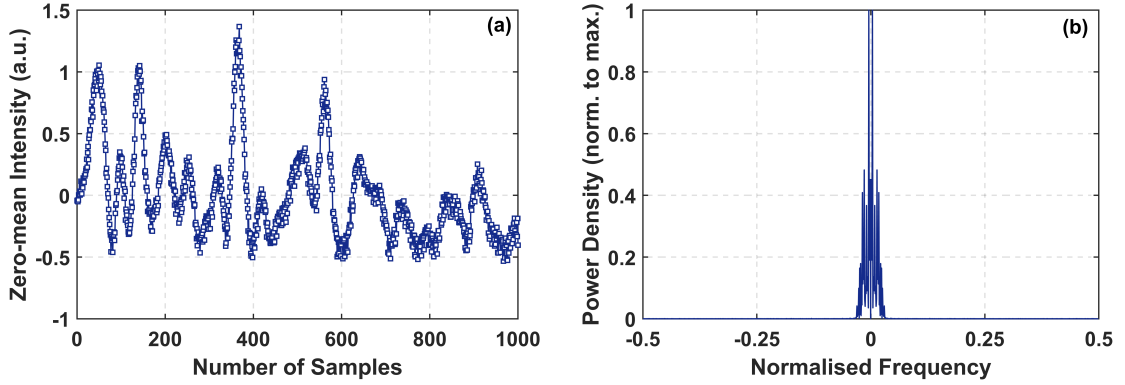
Figure 4.6 – (a) Back-scattered zero-mean intensity; (b) Localised power density (norm. to max.) of the signal in (a) as a function of the normalised frequency.

the most general approach which can be followed for the calculation of β. In this approach, no prerequisite information about the power density of the artificially-constructed signals is required. Finally, the value of the FS uncertainty (σ) obtained in Eq. (4.16) is then scaled back by the original frequency scan step Δf such that the absolute value and the proper unit of σ are yielded.

4.4 Experimental verification of the theoretical expressions

4.4.1 Measurement FS uncertainty dependency on the SNR

As explained in 4.3.1, an analytical expression is proposed to understand the influence of two main system parameters on the measurement frequency shift uncertainty of the φ-OTDR, while estimated using cross-correlation. The expression for calculating β given in Eq. 4.17 can be solved either analytically (as given in section 4.3.1) or computationally (as given in section 4.3.2). The former requires prior knowledge about the shape of the power density of the artificially-constructed trace, unlike in the case of the latter. When the expression for β is solved computationally, the values obtained for β are normalised by the step size of the artificially-constructed signal, hence an associated normalised parameter $\bar{\beta} = \beta \times \Delta f$ is introduced, and will be used in some figures in the manuscript hereafter.

According to the computational approach, we found that the value of $\bar{\beta}$ is varying with respect to the SNR as depicted in Fig. 4.7. This phenomenon is quite counter-intuitive, but will be clearly elaborated later on in this section.

To evaluate this dependency of $\bar{\beta}$ on the SNR, the SNR is varied keeping the pulse width a constant at 10 ns (corresponding to a spatial resolution of 1 m) during the experiment. Fig. 4.8 illustrates the impact of the SNR on the power density. It is quite visible from the figure that a higher SNR yielded a higher amplitude of the power density. $\bar{\beta}$, however, is normalised,
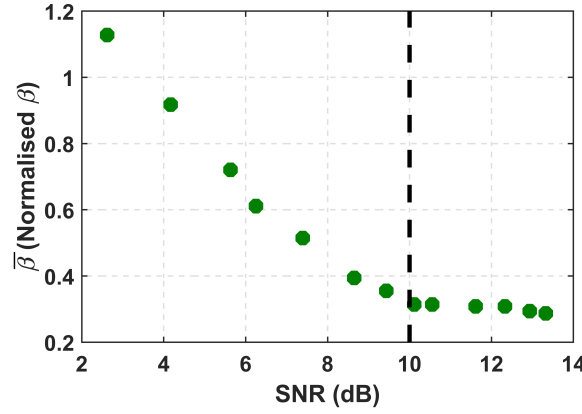
Figure 4.7 – Graph showing the dependency of $\bar{\beta}$ on the SNR. The black dashed line marks the SNR ($\sim$10 dB) at which the $\bar{\beta}$ starts being constant which means that it is not dependent on the SNR anymore.

hence the change in the amplitude of the power density through the SNR variation is cancelled out. Since $\bar{\beta}$ is derived under the assumption that SNR$>>$1, the presence of noise can bring unexpected ambiguities in the value of $\bar{\beta}$, implying that the square root of the second moment of the normalised power density will be higher for low SNR values. Fig. 4.8 (b) depicts $\bar{\beta}$ corresponding to low and high SNR conditions. When the SNR is low, the square root of the second moment of the power density, i.e., $\bar{\beta}$ is high. Alternatively, when the SNR is higher, $\bar{\beta}$ is low and it will remain a constant for even higher SNR values (as shown in Fig. 4.7). This results in an SNR-dependent $\bar{\beta}$ in the low SNR regime, whereas as per the proposed model it should be independent of the SNR. The latter condition is valid only when the SNR is relatively high, and in the present case this value is found to be around 10 dB (illustrated in Fig. 4.7). The constant value of the $\bar{\beta}$ is found accordingly to be around $\sim$0.25.

Figure 4.8 – Graphs showing: (a) the localised power density as a function of frequency for two different signal strengths (solid lines), the envelopes of the power densities (dashed lines); and (b) the square root of the second moment of the power densities ($\bar{\beta}$) in (a) as a function of distance.

It is worth noting that a significant discrepancy between the FS uncertainty calculated from the model and that from the experiment will occur (in the low SNR regime) if the σ is calculated with noise-dependent $\bar{\beta}$. However, fixing the $\bar{\beta}$ to a constant value of ~0.25 in all SNR conditions will result in perfectly-matching experimental and theoretical values, which indicates that the model is valid for all SNR cases as can be seen in Fig. 4.9. The value of $\bar{\beta}$ calculated computationally has to be de-normalised as follows $\beta = \bar{\beta} \times \frac{1}{\Delta f}$. Since $\Delta f = 3.2$ MHz in our case the value of $\beta \sim 78$ ns yielded can be then taken as a constant for any φ-OTDR system using 10 ns rectangular pulses. Other pulse widths can be calculated using a simple proportion.

To validate the expression for the FS uncertainty proposed in Eq. (4.16), various measurements are conducted along a ~100 m long standard single-mode fibre with 1 m spatial resolution. The SNR in the experiments is altered using two techniques; firstly by changing the input power to the fibre while keeping the averaging constant, and secondly by keeping a constant input power while increasing the number of averages. Fig. 4.9 (a) shows the FS uncertainty as a function of the SNR for the case in which the SNR is altered by varying the input power. As can be observed, the inverse proportionality between the FS uncertainty of the measurement and the SNR (M_o) proposed by the theoretical model is validated through the significantly well-matched theoretical and experimental values. In Fig. 4.9 (b), the FS uncertainty is plotted against the number of averages showing the second case in which the SNR is varied by increasing the number of averages. As per the calculation from [89], the SNR is implicitly related to the number of averaged traces through the relationship: $\text{SNR} \propto \sqrt{N_{avg}}$ where N_{avg} is the number of time-averaged traces. Thus, applying this relationship to Eq. (4.16), the FS uncertainty is related to the number of averages by $\frac{1}{\sqrt{N_{avg}}}$ which is illustrated in Fig. 4.9 (b). Fig. 4.9 (a) and (b) show a remarkable agreement between the measured FS uncertainty and the theoretically predicted FS uncertainty. This agreement thus confirms the inverse and inverse square root relationship of σ with the SNR and the number of averaged time-domain traces, respectively.
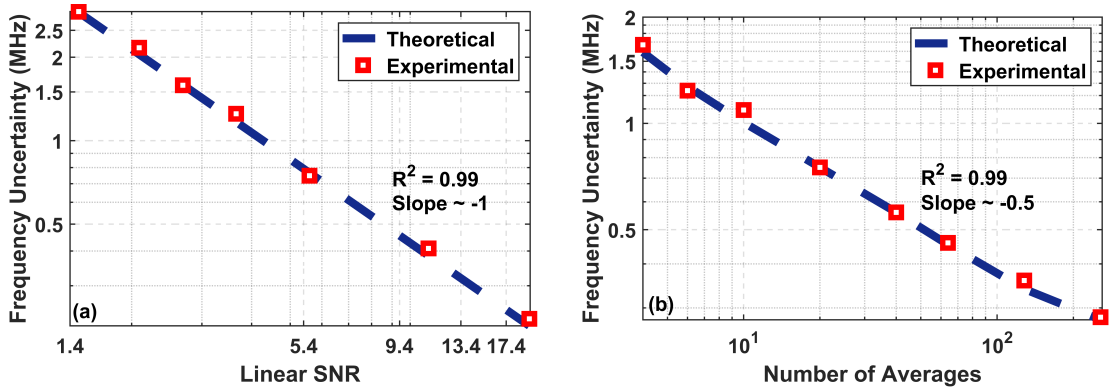
Figure 4.9 – Graphs represent the log-log plot of the frequency uncertainty as a function of (a) the optical power SNR (M_o); and (b) the number of averages.

4.4.2   Measurement FS uncertainty dependency on the spatial resolution

Another major parameter which plays a significant role in the FS estimation is the spatial resolution of the φ-OTDR system (pulse width of the interrogating input pulse). It is found from a number of experimental analyses that the uncertainty in the FS estimation using cross-correlation decreases with the increase of the pulse width. The experiment is performed by keeping all system parameters constant, and only varying the pulse width from 30 ns to 55 ns. From Eq. (4.14), it is obvious that an increase in the pulse width (thereby the spatial resolution) of the input pulse by a factor of 2 will increase the backreflected power P_{BR_φ} by 3 dB, which will be reflected in the SNR as well. This implies that a change in the pulse width is coupled with a linear change in the SNR. In the theoretical model proposed here, the relationship between the FS uncertainty and the pulse width is reflected through the value β. Since these artificially-constructed signals can be thought of as a spectral response of the time-domain traces, and are not directly measured but artificially extracted from the time-domain traces, the alteration of the pulse width is reflected in the artificially-constructed signals as well. Thus, a narrower pulse width results in spectrally-broader individual features

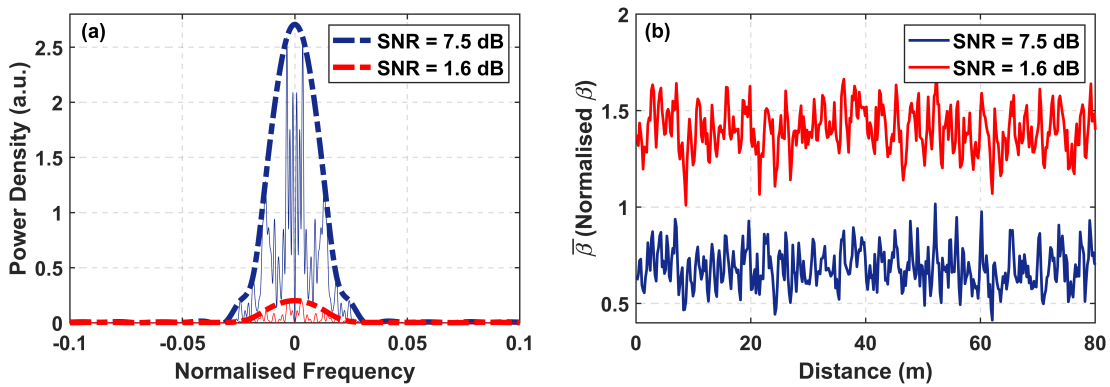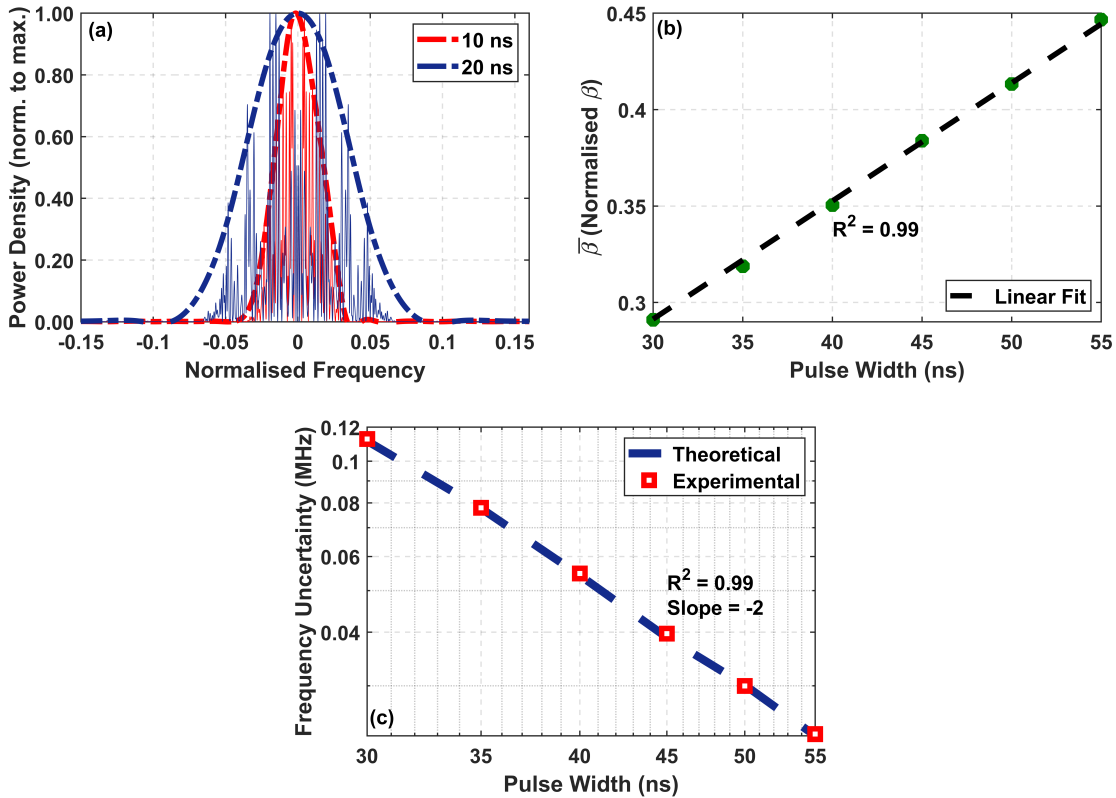Figure 4.10 – Graph showing: (a) the localised power density as a function of frequency for different pulse widths (solid lines), the envelopes of the power densities (dashed lines); (b) $\bar{\beta}$ as a function of different pulse widths; and (c) the log-log plot of FS uncertainty as a function of different pulse widths.

of the artificially-constructed signal (consecutive statistically-dependent points in the signal form one peak), as a result of the broader spectral distribution of the pulse. The power density of such an artificially-constructed signal is then calculated from the Fourier transform of the signal's auto-correlation function. Thus, it returns physically to the domain of the interrogating signal (time-domain). The full width at half maximum yielded for this power density is then linearly proportional to the pulse width used in the experiment. It should be highlighted and clearly understood that both, the interrogating signal and the power density of the artificially-constructed signal, are functions of the same domain and therefore vary jointly.

As given by the analytical expression in Eq. (4.17) for β for a rectangular input pulse, $\bar{\beta}$ of the power density linearly depends on the pulse width τ_{pw}. Experimentally, this is demonstrated as an increment in the width of the normalised power density as illustrated in Fig. 4.10 (a), implying that the square root of the second moment of the power density is proportional to the pulse width. Fig. 4.10 (b) shows the linear dependency of β and the pulse width of the interrogating pulse. It is, thus, confirmed that the larger the width of the interrogating pulse, the higher is the value of β. Finally, the influence of the pulse width on the FS uncertainty is analysed. The dependency of the FS uncertainty on the pulse width is expected to be inversely proportional as suggested by Eq. 4.19. However, since the SNR is also varied with respect to the pulse width, the dependence of the spatial resolution on the FS uncertainty is inverse square as validated through the experimental results given in Fig. 4.10 (c).

4.5 Summary

To sum up, the influence of two key system parameters (SNR and spatial resolution) on the estimation of the FS using cross-correlation is thoroughly evaluated through the presented analytical and computational models along with the experimental results. These experimental validations confirm that the proposed model for estimating the FS uncertainty for Rayleigh-based DOFS with the use of cross-correlation can be used to predict the accuracy of such sensing systems. Besides, the model can be used as an efficient tool for optimising the experimental parameters to achieve the best system performance. The proposed expression is valid in all cases of SNR and all different pulse widths, irrespective of the shape of the interrogating laser pulse and delivers a quantitative prediction of the final uncertainty. Similar functional dependence of the uncertainty on SNR and pulse width is expected using other techniques to determine the FS, such as the least-mean square method [87], though possibly with a different scaling factor to be determined in a further work.

In the following chapter, we will utilise the model presented in this chapter and verify this relationship of the measurement FS uncertainty using the REF, while performing a fully-distributed temperature measurement.

5 Temperature measurement using the REF and φ-OTDR

In the previous two chapters, we extensively studied reflection-enhanced optical fibres and one of the typical Rayleigh-based interrogation techniques that are utilised with this type of fibres. Whilst such reflection-enhanced fibres are extensively employed in several experiments based on φ-OTDR [114], the effect of the experimental conditions on the performance of these fibres has not been examined so far and is yet to be discovered further.

In this chapter, we will present an elaborated study on the use of one of such reflection-enhanced fibres interrogated by means of a φ-OTDR setup. The ultimate aim of the work in this chapter is to investigate the effect of the high backreflection on the overall performance of the sensor. To that effect, we will conduct a fully-distributed temperature measurement and utilise our theoretical model presented in the previous chapter as an evaluation tool for our sensor.

The study presented in this chapter is published in [115] and is reproduced here.

5.1 Enhanced-signal associated noises

5.1.1 Noises in a φ-OTDR system

When compared with a typical incoherent OTDR, φ-OTDR is a highly sensitive interrogation technique for Rayleigh-based DOFS [116], which makes the measurements highly susceptible to environmental fluctuations. The intrinsic backreflected signal enhancement in the REF makes it even more prone to environmental fluctuations and other signal-dependent noises in the system. Hence, the mitigation of such signal-dependent noises is highly essential to fully exploit the signal enhancement provided by the REF into an effective SNR enhancement. In this context, we observed that conventional methods used to further improve the SNR of the system, for instance through trace time-averaging or straightforwardly by increasing the input optical power to the fibre (below the onset of nonlinear effects) would not necessarily yield the expected results. An investigation of this phenomenon is presented in great detail in

this section.

In a conventional direct-detection φ-OTDR setup, the possible noises in the system responsible for the variation of the photocurrent of the photo-detector (PD) are the thermal and the shot noises of the PD along with the signal-ASE and ASE-ASE beating noises originating from the pre-amplifier used before the PD. It should be noted that for the effect of the ASE-ASE beating noise to be insignificant, an extremely narrow-bandwidth optical filter (much narrower than the one used in our system) after the optical amplifier needs to be utilised. As a result, the standard deviation of several consecutive time-domain traces σ_n which is a measure of the total detected noises in the PD can be expressed as [116, 117]:

$$\sigma_n = \sqrt{\sigma_{\text{th}}^2 + \sigma_{\text{sh}}^2 + \sigma_{\text{sig-ASE}}^2 + \sigma_{\text{ASE-ASE}}^2} \tag{5.1}$$

where σ_{th}^2, σ_{sh}^2, $\sigma_{\text{sig-ASE}}^2$ and $\sigma_{\text{ASE-ASE}}^2$ are the variances of the thermal noise, shot noise, signal-ASE beating noise, and ASE-ASE beating noise, respectively. σ_{th} is independent of the optical power of the backreflected light (P_{BR}) to the PD, whereas the σ_{sh} and $\sigma_{\text{sig-ASE}}$ are dependent on P_{BR} through a square-root relationship. The expressions describing the variances of the corresponding voltages for the different noises are written as follows [116, 117]:

$$\sigma_{\text{th}}^2 = 4 k_B T R_f B_{\text{eq}} + 3.7 k_B T \pi^2 R_f^2 \frac{C_t^2 B_{\text{eq}}^2}{g_m} \tag{5.2}$$

$$\sigma_{\text{sh}}^2 = R_f^2 \, 2 \, q_e \left(\frac{\eta_{\text{PD}} \, q_e \, P_{\text{in}}}{h\nu} + I_d \right) B_{\text{eq}} \tag{5.3}$$

$$\sigma_{\text{sig-ASE}}^2 = (q_e \eta_{\text{PD}} G_A R_f)^2 \frac{2 F_A P_{\text{BR}} B_{\text{eq}}}{h\nu} \tag{5.4}$$

$$\sigma_{\text{ASE-ASE}}^2 = (q_e \eta_{\text{PD}} G_A F_A R_f)^2 P_{\text{BR}} B_o B_{\text{eq}} \tag{5.5}$$

where k_B is the Boltzmann constant, T is the temperature, R_f is the transimpedance gain resistance, B_{eq} is the equivalent noise bandwidth related to the photo-detector bandwidth through $B_{\text{eq}} = \frac{\pi}{2} B_{\text{PD}}$, C_t is the total input capacitance of the photo-detector, g_m is the field-effect transistor transconductance, q_e is the electronic charge, η_{PD} is the photo-detector quantum efficiency, h is Planck's constant, ν is the laser frequency, I_d is the dark current of the photo-detector, G_A and F_A are the gain factor and the optical noise figure of the optical amplifier, respectively. F_A is written as a function of the gain factor as follows: $\frac{1 + 2 n_{\text{sp}} (G_A - 1)}{G_A}$ where n_{sp} is the spontaneous emission factor (ideally 1), and B_o is the optical bandwidth.

The SNR of the system which is estimated directly from the time-domain trace following an exponentially-decaying probability density function is given by:

$$\text{SNR} = \frac{\mu_{P_{\text{BR}}}}{\sigma_n} \tag{5.6}$$

Here, $\mu_{P_{\text{BR}}}$ is the mean and σ_n is the standard deviation of the electrical amplitude of the reflected optical signal along the fibre, for several consecutive measurements. It should be mentioned that the electrical amplitude of the signal is equivalent to the optical power through

the conversion gain of the photo-detector. As mentioned in the previous sections, P_{BR} can be calculated theoretically using Eq. 3.1. The impact of the variable attenuation utilised before the PD in the φ-OTDR setup should, of course, be taken into consideration when calculating the effective gain provided by the pre-amplifier [118]. It should be mentioned that during the experiment, the average power to the PD is maintained well below saturation by means of a variable attenuator.

5.1.2 Different noise regimes in a φ-OTDR system

To understand the influence of the different noises (mentioned in section 5.1.1) on the SNR improvement of the system with respect to the backreflected signal, we performed the experiment using the same experimental setup mentioned in the previous section which is depicted in Fig. 4.2. We varied the input power to the fibres under consideration and observed the behaviour of the SNR accordingly. The evolution of the SNR as a function of the backreflected power (P_{BR}) from the two sets of fibres is illustrated in Fig. 5.1. It can be clearly seen that for a given input peak power (P_{in}) to the fibres and considering their lengths of 100 m each, the SNR of the REF is always higher than that of the SMF due to the intrinsic increase in the backreflection coefficient (α_{BR}) of the former. Additionally, the evolution of the SNR with respect to the input power (or backreflected power) of the REF is very similar to that of the SMF, but at a noticeably faster rate. There are two distinct regimes of interest in terms of the SNR improvement shown in Fig. 5.1. In the first region (Region A in Fig. 5.1), the SNR of the system is improved linearly (slope of ~1 in the log-log graph of Fig. 5.1) with respect to the in-
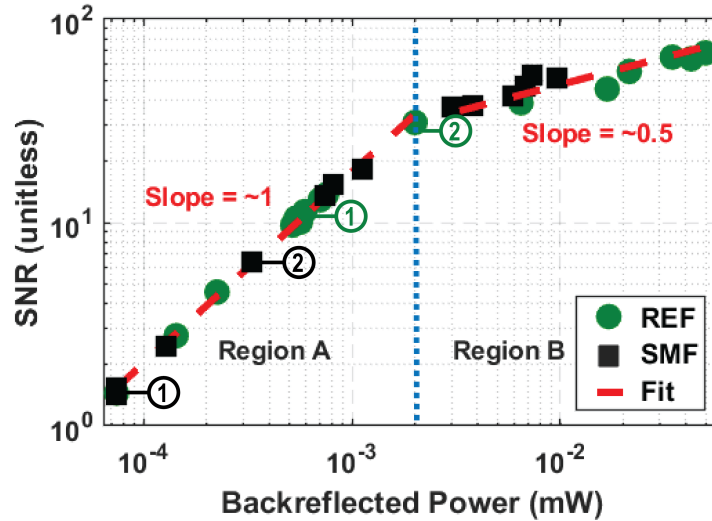
Figure 5.1 – Log-log graph showing the SNR as a function of the backreflected power for both fibres. The encircled numbers mark SNR values at two different input peak powers for both fibres (black circles for SMF, green circles for REF). The same number corresponds to the same input power for the two fibres; ① corresponds to an input power of ~18.9 dBm and ② corresponds to ~25.4 dBm.
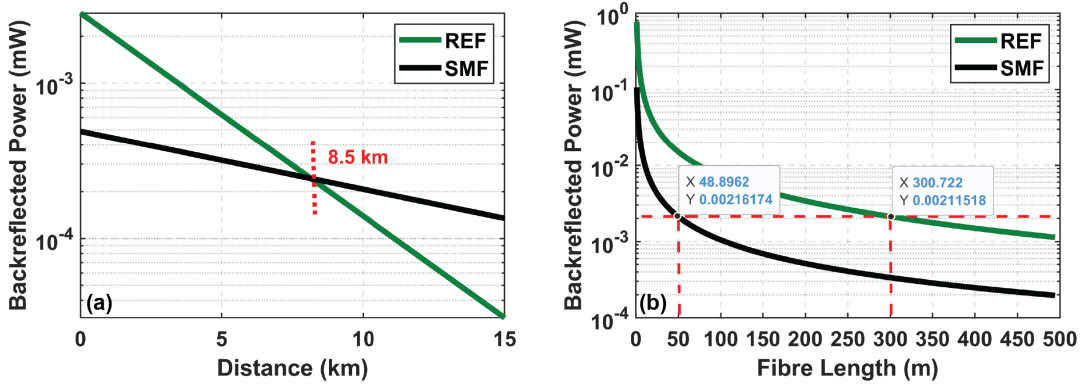
Figure 5.2 – (a) Log-log graph showing the backreflected power as a function of distance for both fibres; (b) Semi-log graph showing the backreflected power as a function of the fibre length for both fibres calculated using Eq. 5.6 highlighting the contribution of the loss term.

put/backreflected power to/from the fibre. This is mainly because σ_n in Eq. 4.11 is dominated by the signal-independent noises, namely σ_{th} and $\sigma_{ASE-ASE}$. In the second region (Region B), the SNR of the system is improved with a square-root dependency (slope of ~0.5 in the log-log graph of Fig. 5.1) with respect to the backreflected power. At these powers, σ_n is dominated by the signal-dependent noises. Under the given experimental conditions (1 m spatial resolution and length of the fibres of 100 m each), a P_{BR} value of 0.002 mW (corresponding to an SNR of ~33.9 (15.3 dB in the dB-scale)) is the threshold below which the SNR of the fibres increases linearly with respect to the input peak power/backreflected power.

As mentioned in the earlier paragraph and as can be seen from Fig. 5.1, the SNR of the REF is always higher than that of the SMF irrespective of the kind of noises affecting the SNR. This implies that a better SNR is achieved with such backreflection-enhanced fibres as long as the contribution of the exponential term in Eq. 3.1 is lower than the enhanced backreflection coefficient (α_{BR}). In this particular kind of REF, having an α_{BR} of ~-64.1 dB/m and α of ~0.7 dB/km, a higher P_{BR} is observed up until a fibre distance of ~8.5 km (Fig. 5.2 (a)). Beyond this length, as a result of the increased loss in the REF, the value of P_{BR} of the SMF will start to be higher than that of the REF.

It is interesting to further analyse the consequences of this change of regime for different sensing configurations and thus to determine under what conditions the SNR could be impaired. In an optimised configuration for a sensor of given fibre length, the input peak pulse power to the fibre (P_{in}) is set at its maximum possible value, which is the critical power P_{crit} allowed below the onset of nonlinear effects in the fibres, mainly the effect of modulation instability [119]. Assuming a spatial resolution of 1 m and varying the sensing fibre length, the threshold value of P_{BR} (0.002 mW, under the present experimental conditions) is obtained when the total length of the REF is around 300 m. Since α_{BR} of the SMF is lower than that of the REF, this value is reached when the length is around 50 m. This implies that when using P_{crit} as the input power to the fibres under consideration, they will be in the signal-independent

noise regime (Region A in Fig. 5.1) when the length of the fibres is greater than 300 m and 50 m for the REF and the SMF, respectively. For any length of the fibres that is shorter than these values, at the P_{crit}, the noise regime of the fibres can only be in Region B in Fig. 5.1. The noise regime in Region B is therefore predominant only for short sensing ranges and is observed at all positions over this fibre length, given the negligible effect of attenuation over such short distances. As a corollary, a change of spatial resolution will modify the critical length of the fibre proportionally (e.g. a 2 m spatial resolution will extend the limit lengths shown in Fig. 5.2 (b) by a factor 2). These numbers are critically related to the noise level of the optical amplifier and can certainly vary depending on the devices used in the experimental setup. However, the noise level is observed to stay in a given range in most commonly-used amplifiers and the numbers presented here can be safely considered as a good representation of a general situation.

We also demonstrate a peculiar situation in which there is dissimilarity in the noise regimes

Figure 5.3 – (a) Time-domain trace (optical power) along the distance of the fibre; (b) The standard deviation of 20 time-domain traces corresponding to input peak powers of around 25.4 dBm. (c) Cross-correlation between the time-domain traces and the standard deviation traces of (a) and (b)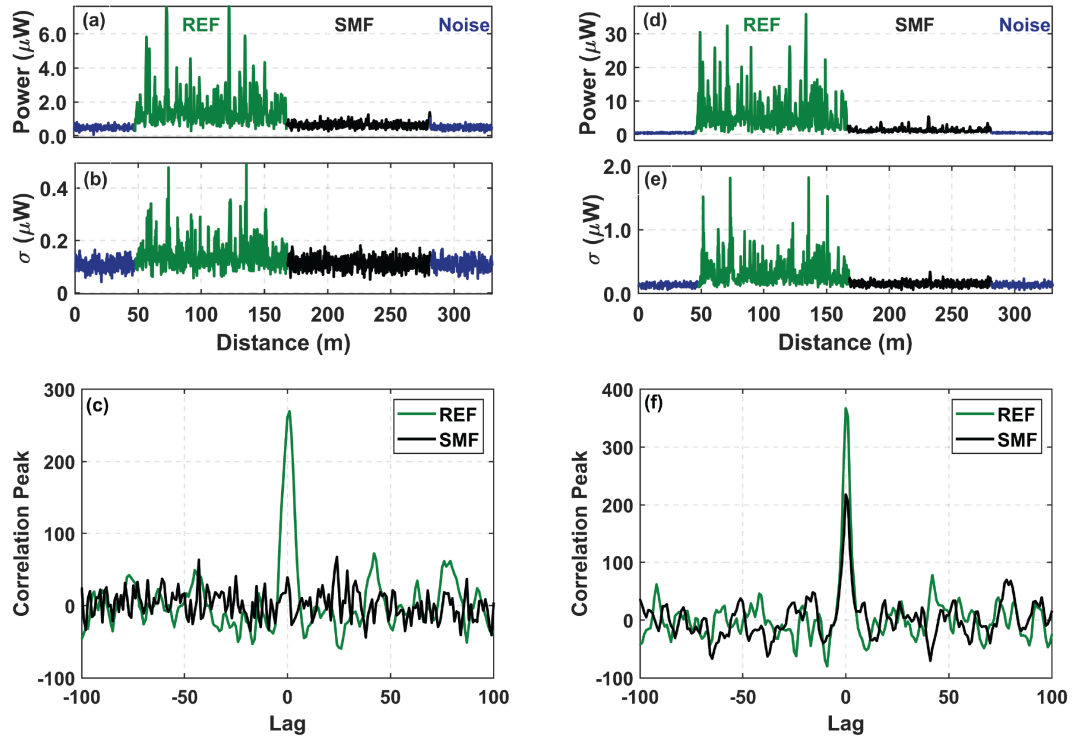; (d) Time-domain trace (optical power) along the distance of the fibre; (e) The standard deviation of 20 time-domain traces corresponding to input peak powers of around 33.2 dBm. (f) Cross-correlation between the time-domain traces and the standard deviation traces of (d) and (e). Note: The blue traces before and after the fibres in (a), (b), (d) and (e) represent the noise floor.

between the REF and the SMF with the aid of Fig. 5.3 for a given input power. It ought to be remarked that this situation may probably be the most common if a comparison is made between the two fibres. Fig. 5.3 (a) shows the Rayleigh back-scattered optical intensity time-domain traces, and Fig. 5.3 (b) shows the standard deviation traces of several consecutive time-domain traces of the REF and the SMF for an input peak power of 25.4 dBm. It should be mentioned that the two sets of fibres are adjoined such that the signals received at the PD from the fibres experience the same experimental and detection conditions. Under these conditions, the signal enhancement provided by the REF (estimated from the mean of the time-domain trace) is nearly 7.4× (~8.7 dB) higher than that of the SMF (Fig. 5.3 (a)). The REF/SMF standard deviation ratio is around 1.2× (Fig. 5.3 (b)), yielding an overall 7.9 dB higher SNR for the REF when compared to the SMF, instead of a full SNR increase of 8.7 dB higher. That is because at the used input peak power of 25.4 dBm, signal-dependent noises are more prominent in the case of the REF, whereas in the case of the SMF, the overall noise is limited by the signal-independent noises of the system. This claim is evident from Fig. 5.3 (a) and (b), and can be further substantiated by Fig. 5.3 (c) which shows the cross-correlation between the time-domain trace and the standard deviation trace of Fig 5.3 (a) and (b). A clear correlation peak is observed for the REF, but as expected there is zero correlation for the SMF. This rather simple correlation technique between the time-domain trace and the standard deviation trace clearly points out whether the noises are signal-dependent or not. As can be seen in Fig. 5.3 (b), the mean of the standard deviation of the SMF matches well with the mean of the noise floor of the system confirming that for the given input power to the fibres, the SMF is limited by signal-independent noises, whereas the REF is not. If we take a look at a different scenario where the input peak power to the fibres is around 33.2 dBm (Fig. 5.3 (d) and (e)), we will notice that in this case both fibres are limited by signal-dependent noises. This again can be clearly observed in Fig. 5.3 (f) using the correlation between the signals of Fig. 5.3 (d) and (e), where we can now see a significant correlation peak for the SMF as well. Unlike in the case with lower power, in this case the SMF is no longer limited by the signal-independent noises in the system and is now in the regime of signal-dependent noises.

This is a crucial inference because the SNR improvement provided by the REF is not always exactly matching with the signal enhancement when put in comparison with the SMF at a given input power. For this difference in the SNR to be maintained between the REF and the SMF, both of them should share similar standard deviation of the measurement. Having different sets of noises in the two different fibres can lead to an erroneous estimation in the physical parameters like the temperature uncertainty when a comparison is made. Hence, the present analysis of the enhanced signal from the REF highlights the need for the regulation of the input power to such fibres and the optimisation of the interrogation setup to yield the best performance.

Beside the analysis of the SNR with respect to the power, we also investigated the SNR dependency on the number of time-averaged traces, and confirmed the square-root dependence (slope of 0.5 in a log-log graph) in the case of the SMF, but the dependence was slightly different for the REF (slope of 0.2 in a log-log graph). The range of averages between 1 and 2048 averages

is applied to the traces, and already at 8 averages the difference in the slope is observed. This again implies a slower rate in the SNR increase for the REF. Since this result is quite surprising, we speculate that this discrepancy is possibly occurring because of other sources of noises that take place when the duration of the experiment is extended (e.g. signal distortions due to environmental fluctuations). We further confirm our speculations by nullifying this anomaly using a real-time data acquisition card (DAQ), thereby yielding a square-root dependence of the SNR with respect to the number of averages for both fibres.

To sum up, the management of the number of time-averaged traces (if no real-time DAQ is available) as well as the input power to such backreflection-enhanced fibre is vital to benefit from its full potential. It should be considered that the higher intrinsic signal enhancement, like in the REF, is always accompanied by higher signal-dependent noises and any increment in the input power (even though well below the onset of the nonlinear effects) will not necessarily yield the expected SNR enhancement as explained earlier. Hence, addressing the signal-dependent noises is crucial to understand how to utilise the full potential of such fibres.

5.2 Experimental Demonstration

Despite the fact that using such backreflection-enhanced fibres can be quite tedious due to the continuously interfering system noises, they can be really beneficial in DOFS, provided that the experimental conditions are optimised. One interesting characteristic offered by backreflection-enhanced fibres, as a pure consequence of the enhanced SNR, is a fairly better spectral shift quality as can be seen in Fig. 5.4. As shown, the REF is has a more distinct correlation peak that is around 1.5× higher than the SMF. This quantity can be explained as the measure of the correlation strength between two data sets, when interrogated using a φ-OTDR setup. Commonly, when a frequency-scanned φ-OTDR system is employed, the correlation strength can be significantly improved (at a given SNR), and large correlation errors can be
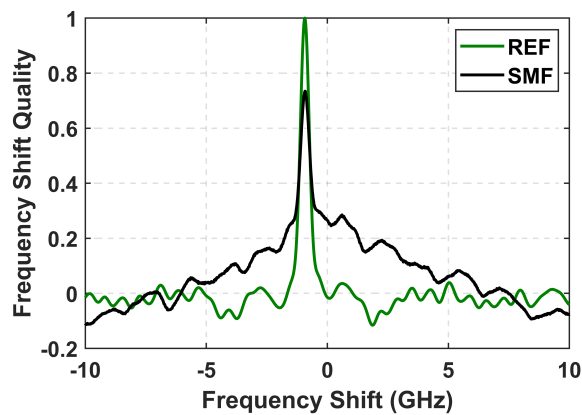
Figure 5.4 – Local correlation as a function of the frequency shift at an arbitrary position in the two fibres.

mitigated when the frequency scan range of the probe pulse is sufficiently large [120]. Yet, a large scan range requires a longer measurement time. However, if the SNR is high enough with the aid of a fibre like the REF, the scan range can be significantly reduced leading to much faster measurements.

5.2.1   Temperature measurement

Under the same amplification and detection conditions, and by taking utmost advantage of the qualities exhibited by the REF, a distributed temperature measurement with the REF and the SMF is performed with the setup shown in Fig. 5.5. The experimental setup is the same as that presented in section 4.2.2 (i.e. the same specifications of the devices are used) except for the fact that in this demonstration we are interrogating the REF followed by an SMF. We are adding a hot spot of 5 m at each fibre end to perform the temperature measurement, and accordingly the frequency-scan range and step are changed to 13 GHz and 17 MHz, respectively. At the hot spot, the temperature is varied from 301.5 K to 309 K.

In an initial work conducted by us [121], we observed an unexpected disparity in the temperature uncertainty improvement. In that work, at first glance, it seemed that the improvement in the temperature uncertainty was not following the inverse relationship with the increase in the SNR, when we were conducting a comparison between the SMF and the REF. As mentioned in the previous section, for the given input power, the total noise of the REF was dominated by the signal-dependent noise (thereby higher σ_n), whereas for the SMF it was the signal-independent noise dominating. This apparently reduced the SNR difference between the two sets of fibres below the intrinsic value of 8.7 dB. Such an erroneous estimation can be made very commonly due to the lack of the awareness of the different noises playing the role for the same input power.

Thus, in the present case this is mitigated by controlling the experimental conditions. The input peak power launched into the fibres under test is 25.4 dBm and no averages were applied to the traces, so as to avoid any environmental fluctuation, such that a proper 8 dB SNR difference between the two fibres is attained. Since the frequency shift uncertainty of the
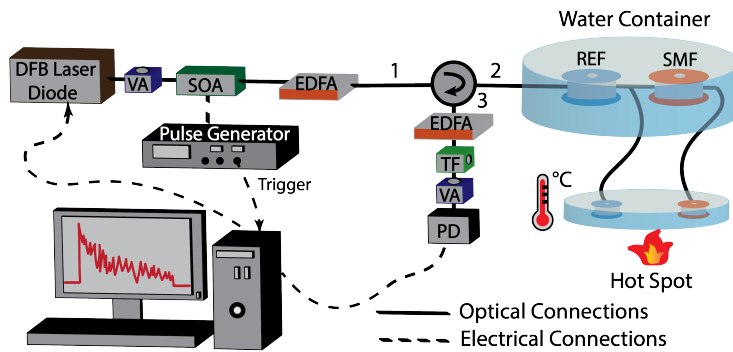
Figure 5.5 – Experimental setup of a frequency-scanned φ-OTDR using direct detection.
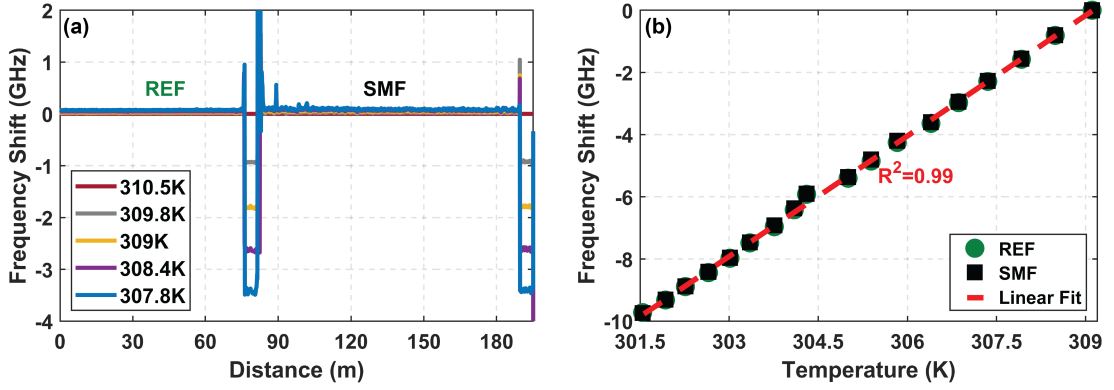
Figure 5.6 – (a) Frequency shift versus the distance along the fibre; (b) Frequency shift as a function of temperature with a slope of 1.29 GHz/K.

measurement, in a Rayleigh-based DOFS, is inversely proportional to the optical SNR of the signal, it is expected that the temperature uncertainty of the REF will be much lower than that of the SMF, for a given set of experimental conditions. Fig. 5.6 (a) shows the frequency shift of the Rayleigh back-scattered intensity of the REF and SMF over a range of 10 K. It shows the frequency shift of the temperature measurement as a function of distance and highlights the position of the hot spot in the two fibres under consideration. The frequency shift as a function of temperature is depicted in Fig. 5.6 (b). The linear fit of the plot yielded a correlation coefficient of 0.99, and the sensitivity obtained from the slope, for both REF and SMF, is 1.29 GHz/K. This implies that, despite the modifications of the fibre core due to the presence of continuous Bragg gratings throughout the REF, the thermo-optic coefficient of the original silica fibre is not altered, thereby showing the same temperature sensitivity as that of the SMF.

5.2.2 Model verification with REF

The frequency uncertainty (σ_f) of the temperature measurement calculated from the traces for an arbitrary fibre distance of 40 m (shown in Fig. 5.6 (a)) as well as the theoretical uncertainty (red dashed lines) calculated using the expression in Eq. 5.7 are illustrated in Fig. 5.7. As can be seen, in the case of the REF, for a metric spatial resolution, the mean value of the uncertainty is found to be 0.6 MHz, which is nearly 6.5× lower than that of the SMF. This significantly low uncertainty value for the REF is a pure consequence of its ~6.5× (~8 dB) higher SNR, and this can be corroborated by our model presented in section 4.3.1, in which we found out that, for a Rayleigh-based sensing system using a rectangular input pulse, σ_f is inversely-related to the SNR as given by Eq. 4.19 which we will repeat here for convenience:

$$\sigma_f = \frac{\sqrt{6}}{2\pi \tau_{\mathrm{pw}} M_o} \tag{5.7}$$

79
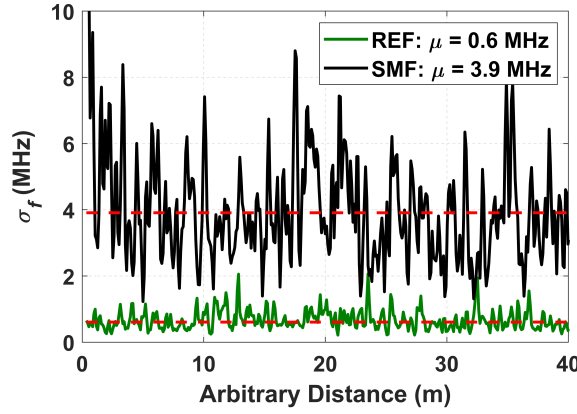
Figure 5.7 – Experimental frequency uncertainty as a function of an arbitrary distance of 40 m in each fibre; theoretical values (red dashed line).

where τ is pulse width and M_o is the system SNR for optical power. The temperature uncertainty, σ_t, is in turn given as a function of σ_f as follows:

$$\sigma_t = \frac{\sigma_f}{S} \tag{5.8}$$

where S is the temperature sensitivity (1.29 GHz/K) of the fibres under test. Using Eq. (5.8), which provides a direct relation between σ_t and σ_f, the temperature uncertainty obtained when using the REF is as low as 0.5 mK, whereas that of the SMF is 3 mK which is the generally known value for standard single-mode fibres for metric spatial resolution.

5.3 Summary

In this chapter, we investigated the performance of a state-of-the-art commercially-available backreflection-enhanced fibre (REF). Its performance was analysed in comparison with a standard SMF, since the only difference between those two fibres is the fact that the REF has weak chirped gratings inscribed inside its core. From our experiments, we realised that when using such REFs with highly-sensitive commonly-used interrogation systems (e.g. φ-OTDR), good care needs to be taken and enhanced-signal associated noises have to be properly considered to exploit the full potential of such fibres. We, accordingly, performed a temperature measurement to corroborate our theoretical model presented in the previous chapter using this REF. Finally, we concluded that due to the high SNR of such fibres, we can obtain very low temperature uncertainties which scale with the same amount of increase in the SNR following an inverse proportionality.

With this chapter, we conclude the work of the first group that dealt with solid silica-core optical fibres. In the coming chapters, we will present the work of the second group that covers the investigation of state-of-the-art hollow-core optical fibres filled with a gas with the ultimate aim of exploring their potential to be employed as distributed optical fibre sensors.

6 Investigation of novel gas-filled hollow-core optical fibres

Over the past 50 years, fibre optics technology has successfully resulted in significant advancements in the fields of optical communications, laser technologies and optical sensing. The continuous thirst for reaching the ultimate performance of the optical fibres, and the ambition to surpass the fundamental loss limit of ~0.15 dB/km in silica fibres has oriented the research towards inventing and fabricating novel types of optical fibres. The current vast growth in the field of hollow-core optical fibres and their rapid integration in lots of research and industrial applications is remarkably impressive. The structure of these fibres highly restricts the interaction of light with silica resulting in the propagation of light mostly in air. Such fibres show great potential and versatility when it comes to telecommunications applications because of their wide transparent window and the hope of possibly breaking the loss limit. Besides, such fibres also provide a suitable platform for light-matter interaction especially when filled with a fluid, for example. They are not subject to high optical power damage as in the case of conventional silica fibres and can provide long interaction lengths which enable efficient wave coupling. Therefore, they can be regarded as perfect candidates for optical non-linearity and sensing applications. The first demonstration showing how the hollow characteristics of such emerging fibres can be taken advantage of by creating a suitable medium within the core of the fibres was presented in [122], where Raman scattering in a hydrogen-filled hollow-core photonic-crystal bandgap fibre (HC-PCF) was measured. Their work indicated that hollow-core optical fibres can be filled with a fluid, for instance, and accordingly generate a viable medium where scattering can occur. In other works [13, 48, 123], Brillouin scattering in gas-filled HC-PCF and at the surrounding of nano-fibers was demonstrated, where a manyfold Brillouin gain amplification over that observed in silica-core fibres was reported.

Even though they proved themselves as good candidates for optical sensing and non-linearity, HC-PCFs have never reached the expectation of offering extremely low back-scattering loss for optical communication, and this is because of the limiting frozen-in surface capillary waves that are excited by the background thermal noise [6]. This is when state-of-the-art hollow-core anti-resonant fibres (HC-ARFs) found their way in, as they showed a loss as low as

0.174 dB/km in both C and L band [7]. In particular, it was recently shown in [124] that for nested anti-resonant nodeless fibres (NANF), the Rayleigh back-scattering is 40 dB lower than that of a standard silica single-mode fibre (SMF). Since such fibres exhibit the same advantages as those provided by HC-PCFs, it is of great interest to investigate the optical non-linearity of such fibres and their capabilities to be used for optical sensing. In a nutshell, the goal of the following two chapters is to investigate the potential of HC-ARFs as a platform for light-matter interaction and for distributed optical fibre sensing.

6.1 Light guiding in hollow-core optical fibres

The guiding of light in optical fibres is always an interesting topic to explore and understand. The guiding mechanism for conventional silica fibres, namely total internal reflection (TIR) has been known for a relatively long time. If the fibre is subjected to modifications such as the imprinting of Bragg gratings or using doping or changing from step index to graded index, etc., the guiding of light is preserved as long as the refractive index of the core is larger than that of the cladding.

In 1991, the idea of trapping light in an optical fibre's hollow core was proposed by Philip Russell. He explained that light guiding can be achieved by creating a cladding made of a periodic wavelength-scale lattice of microscopic holes "photonic crystal" which is encircling
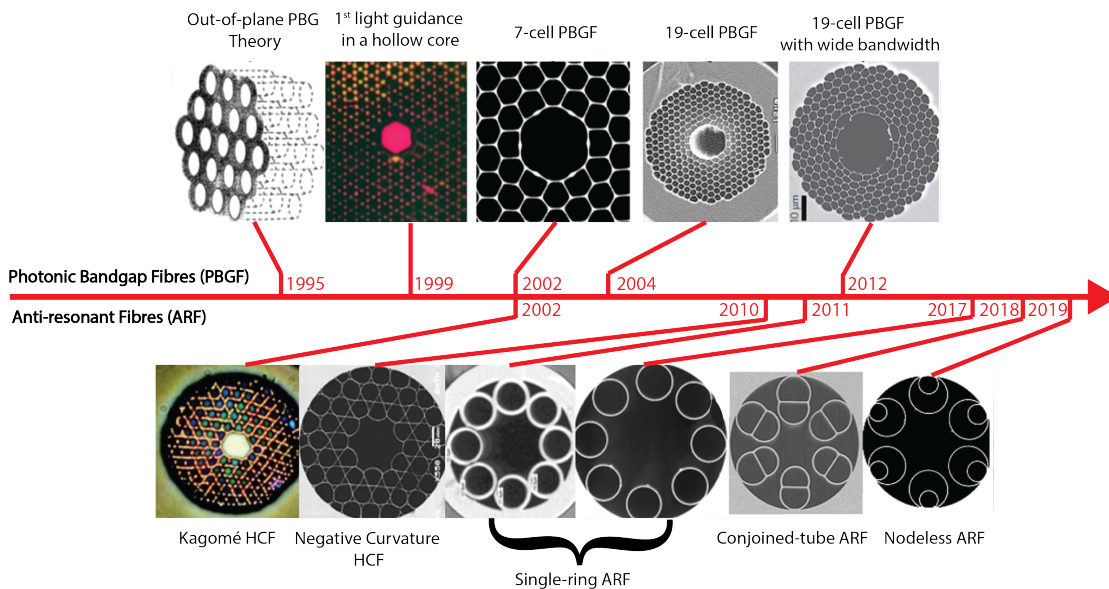

Figure 6.1 – Illustration showing a timeline of the development of hollow-core fibres. In the upper branch of the timeline we can see the evolution of hollow-core fibres whose light guiding is based on the photonic bandgap, and in the lower branch we see the evolution of hollow-core fibres whose light guiding is based on the anti-resonance phenomenon; figure adapted from [125].

a holey fibre core [126], and the light will be simply confined within this central hollow core. Later on in 2002, *Benabid et al.* presented a new type hollow core fibres, namely Kagomé hollow-core fibres (HCF) [122]. The name of this type of fibres originates from the Japanese language, as it is referred to traditional Japanese baskets, called Kagomé, that have some sort of an intertwined pattern from which the structure of the cladding lattice of this HCF is inspired. Even though both types of fibres have hollow cores, their guiding mechanism is different, and this is essentially attributed to the dissimilar cladding structures that the two types have. The timeline for the development of the various hollow-core fibres is illustrated in Fig. 6.1. In the following sections, we will, therefore, discuss the different light guiding mechanisms.

6.1.1 Hollow-core photonic crystal bandgap fibres

The first type of hollow-core optical fibres are hollow-core photonic crystal bandgap fibres (HC-PCFs) and are often also referred to as hollow-core photonic bandgap fibres (HC-PBGFs). Concerning this type of fibres (upper branch of Fig. 6.1), the light propagates in a central hollow core by virtue of the presence of a photonic bandgap in the cladding region which is formed by a periodic lattice array of capillaries. The periodic arrangement of two different dielectrics in the cladding gives rise to a frequency band in which photons are forbidden to propagate, thus remain tightly confined within the central holey core and cannot escape through the cladding. The cross-section of the fibre is typically a honeycomb lattice with a central hollow core. The dimensions of each unit cell of this lattice (e.g. the diameter of the cladding air holes, the thickness of the silica struts, etc.) as well as the number of layers forming the lattice are the parameters which determine the guidance frequency bandwidth and the central frequency supported by such fibres. The typical bandwidth of the guidance window of bandgap HC-PCFs is relatively small (~100-200 nm), and their lowest transmission loss reported thus far reached 1.2 dB/km [6]. This type of fibres have proven to be useful in a wide range of applications like spectroscopy [127–129], gas sensing [130, 131], optical non-linearity and distributed optical sensing [48, 122], etc.

6.1.2 Hollow-core anti-resonant fibres

The second type of hollow-core optical fibres are hollow-core anti-resonant fibres (HC-ARFs). Under this category come a lot of fibres which share the same guiding mechanism. As can be seen in Fig. 6.1, Kagomé HCFs are the very first fibres that emerged from this category. At first glance, the cross-sectional pattern seems to be very similar to the that of bandgap HC-PCFs, however, the structure of the cladding of this fibre does not form a photonic bandgap. Extensive studies were conducted to understand the ambiguity of such fibres and figure out their exact light guiding mechanism [132]. Conclusions were drawn and it was agreed upon that the light is guided by means of the anti-resonant reflection occurring within the thin glass walls surrounding the core [133, 134]. Anti-resonant reflection is achieved based on the principle of thin-film interference. This means that for a waveguide to confine light using anti-resonant reflection, the surrounding should be structured such that a Fabry-Pérot etalon
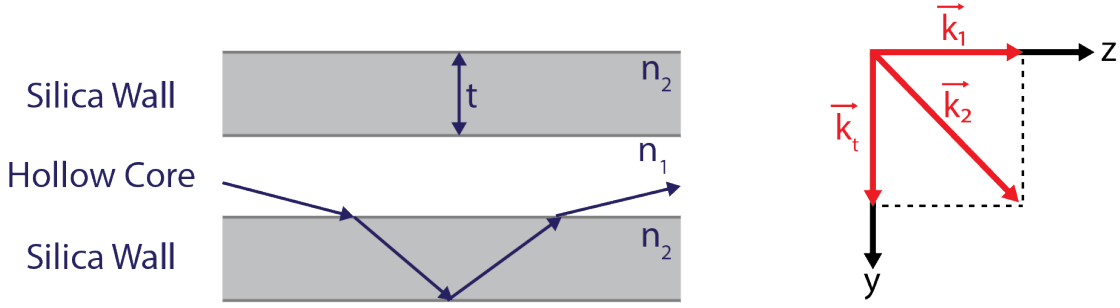
Figure 6.2 – Schematic showing the principle of anti-resonant reflection. Left figure: Simple ray diagram showing the light being guided within the hollow core (with refractive index n_1) and reflected back from the interfacing silica glass wall (with refractive index n_2) of thickness t; Right figure: Simple wavevector diagram for the light that is penetrating through the interfacing silica wall; Figure adapted from [137].

is formed [135, 136]. In the anti-resonant HCFs seen in Fig. 6.1, we observe capillaries in the cladding that have thin glass walls which form the Fabry-Pérot etalon. When the wavelength of the light entering this cavity is close to the resonance wavelength of the Fabry-Pérot, the light interferes with itself constructively, and is allowed to pass through the capillary walls and does not reflect back into the core. However, when the Fabry-Pérot is not at resonance, the entering light undergoes destructive interference, and get backreflected into the central core of the fibre. This is referred to as anti-resonant reflection.

A simplified ray diagram of a ray of light entering the glass wall from the core and being reflected back is shown in the left part of Fig. 6.2. The wavevector diagram showing the ray penetrating through the interfacing silica wall is depicted in the right part of Fig. 6.2. It should be noted that the wavevector diagram for the light that is exiting the silica wall back into the hollow core will be essentially the same as the one depicted in the right part of Fig. 6.2 except for the fact that it will be in the opposite direction. The wavevector in the core (k_1) lies along the fibre axis (z-axis) because the light exits the core and enters the silica walls at a glancing angle. The resonance condition mentioned earlier occurs at specific frequencies for a given wall thickness (t), and the resonance frequencies can be calculated using a formula derived using the wavevector diagram. We start the derivation with the mathematical equation for the resonance condition [137, 138]. When the light in the wall interacts with itself in the transverse direction, it will only interfere constructively with itself if the total phase difference in the transverse direction (along y-axis) between the wave that penetrates through interface into the hollow core and the one that exits the core into the silica wall is a multiple of 2π. Mathematically this can be described as follows:

$$\varphi_r = k_t s = 2\pi m \tag{6.1}$$

where φ_r the phase difference between the entering (into the core) and the exiting (from the core) waves, and s is the total distance travelled by the wave in the transverse direction

which is equal to $s = 2t$, since the wave passes the wall thickness twice, and m is an integer representing the number of interferences. $\vec{k_t}$ is the transverse component of the wavevector in the silica wall. The propagation constant $k_t = \left|\vec{k_t}\right|$ is given by:

$$k_t = \sqrt{k_2^2 - k_1^2} \tag{6.2}$$

where $k_1 = \left|\vec{k_1}\right| = n_1 k_0$ is the propagation constant of the light in the hollow core, and $k_2 = \left|\vec{k_2}\right| = n_2 k_0$ is the propagation constant of the light in the silica glass with $k_0 = \frac{2\pi}{\lambda_0}$ as the propagation constant in vacuum. By substituting these values into Eq. 6.2 and combining it with Eq. 6.1, we end up with the following expression:

$$2t\sqrt{n_2^2 k_0^2 - n_1^2 k_0^2} = 2\pi m \tag{6.3}$$

Using the expression for k_0 mentioned above, Eq. 6.3 can be rearranged as follows [138]:

$$\lambda_m = \frac{2t}{m}\sqrt{n_2^2 - n_1^2} \tag{6.4}$$

where λ_m is the resonant wavelength where the value of m represents the order of the resonance. Eq. 6.4 is the key expression typically utilised during the design of ARFs. It provides the designer with information about the location of all orders of resonant peaks. Ideally, the resonant peaks should be very narrow, but in a real-life scenario they have a rather broader bandwidth due to problems that may arise during the fabrication or inaccuracies in the measurement of the silica wall thicknesses surrounding the hollow fibre core. For fibres with complex patterns and structures like the Kagomé fibres, there may be several resonant peaks present which cannot be calculated by Eq. 6.4. That is why the focus has been oriented towards fabricating less complex patterns and structures that might be easier to predict using the simple models and approximations. Additionally, anti-resonant fibres have a smaller overlap of the optical field with the glass surfaces, in comparison with photonic crystal fibres, which reduces surface scattering. This, thus, explains the evolution timeline for anti-resonant fibres illustrated in Fig. 6.1.

6.2 Hollow-core fibres used in this study

In this section, we will present the hollow-core fibres utilised to perform the experiments in chapter 7. The scanning electron micrograph (SEM) images of the fibres are depicted in Fig. 6.3. The fibres were either obtained through collaborations or were purchased. The characteristics of each of the fibres will be presented below.
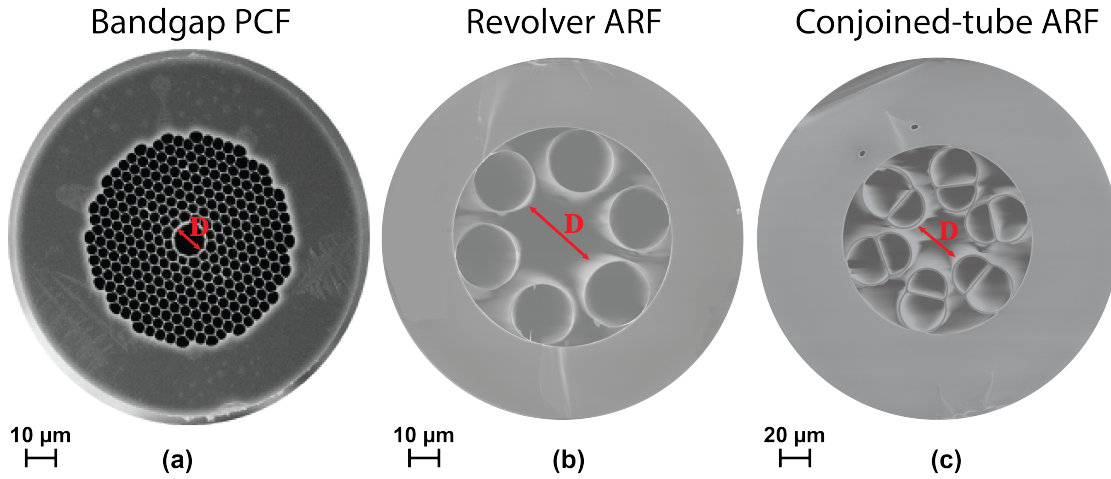
Figure 6.3 – Hollow-core optical fibres utilised in the experiments.

6.2.1 Bandgap photonic-crystal fibre (PCF)

The HC-PCF (HC-1550-02) used in this work is 50 m long and has been purchased from NKT-Photonics. A scanning-electron microscope image of the fibre cross-section is shown in Fig. 6.3 (a). The characteristics of the fibres are as follows [139]:

- **Dimensions:** The fibre has a hollow core which is about 10 μm in diameter D as marked on the scanning electron micrograph (SEM) in Fig. 6.3 (a)) and 79 μm^2 in area.

- **Transmission band:** The fibre has a transmission band between 1490 nm and 1680 nm within which the loss is less than 30 dB/km.

- **Propagation loss:** The fibre loss at 1550 nm is about 16 dB/km.

6.2.2 Revolver anti-resonant fibre (RAF)

The HC-RAF used in this work is 2 m long and has been obtained within a collaboration with Prof. Yingying Wang. A scanning-electron microscope image of the fibre cross-section is shown in Fig. 6.3 (b). The characteristics of the fibres are as follows [140]:

- **Dimensions:** The fibre has a hollow core which is about 35 μm in diameter D as marked on the scanning electron micrograph (SEM) in Fig. 6.3 (b)) and 962 μm^2 in area. The capillaries in the cladding have thin glass walls whose thickness is about ~0.45 μm.

- **Transmission band:** The transmission band of the fibre is from 850 nm to more than 1700 nm.

- **Propagation loss:** The fibre loss at 1550 nm is about 100 dB/km.

6.2.3   Conjoined-tube anti-resonant fibre (CAF)

The HC-CAF used in this work is 21 m long and has been obtained within a collaboration with Prof. Yingying Wang. A scanning-electron microscope image of the fibre cross-section is shown in Fig. 6.3 (c). The characteristics of the fibres are as follows [141]:

- **Dimensions:** The fibre has a hollow core which is about 22 μm in diameter D as marked on the scanning electron micrograph (SEM) in Fig. 6.3 (c)) and 380 μm^2 in area. The capillaries in the cladding have thin glass walls whose thickness is about ~0.71 μm.

- **Transmission band:** The fibre is designed to be used at 1550 nm (lower loss) but has a transmission band from 1302 nm to 1637 nm within which the loss is smaller than 16 dB/km.

- **Propagation loss:** The fibre loss at 1550 nm is less than 5 dB/km.

6.3   Optical and acoustic modes in hollow-core fibres

6.3.1   Optical multi-mode operation

Hollow-core fibres typically guide several modes [142] except for some limited options [143], for instance like those fibres that have small cores [144] or those which have resonant elements in the cladding [145]. The main reason lies in their significantly larger fibre cores which are a consequence of the continuous fabrication attempts to reduce the propagation loss of these fibres. Two types of modes can be distinguished, namely core modes and cladding modes. While some fields may benefit from this feature, for instance by increasing the transmitted capacity through mode division multiplexing (MDM) [146], single-mode operation is generally favoured in lots of other applications like gyroscopes and gas cells. As we will see further in chapter 7, when it comes to optical fibre sensing, at each end of the hollow-core fibre used in the experiments, the light is collected using single-mode fibre pigtails. The coherent superposition of all the fibre modes generates fluctuations in the beam profile and causes the coupling ratio to the single-mode fibre pigtail to also fluctuate. These fluctuations may be observed in the output power in both the time and the spectral domains and can affect measurements performed at low frequencies.

The factor that determines to what extent the fibres can support higher-order optical modes is the ratio between the size of the hollow core and the average size of the hollow capillaries in the cladding, usually denoted by d/D where d is the capillary diameters and D the core diameter. Consequently, the suppression of the higher-order modes can be simply optimised using this ratio d/D. The modal indices for the linearly-polarised modes (LP$_{lm}$ with l and m as the azimuthal and radial orders of the modes) can be approximated by the Marcatili-Schmeltzer expression [147]. The loss of these higher-order modes increases with the mode order, typically by a few times for each subsequent mode group.

A lot of works in the literature have dealt with the problem of higher-order modes and their

suppression. In [148], the authors present guidelines for the design of HC-RAFs and demonstrate very strong higher-order mode suppression within all the low-loss guidance bands of the fibre using a ratio d/D which is approximately equal to 0.68. This then leads to the first higher-order core modes (LP_{11}) to be coupled with the cladding modes and form high-loss super-modes and accordingly results in high confinement loss of the LP_{11} modes. The phase matching between the LP_{11} and the cladding modes offers robust single-mode guidance across the whole transmission window of the LP_{01} modes. In [143], it is shown that HC-RAFs could be engineered in such a way to offer the possibility of a much greater extinction of the higher-order modes, hence a better modal purity. In this case, the HC-RAF is called HC-NANF which stands for nested anti-resonant nodeless fibres. In the same work, it is shown that in the case when the fibres are kept straight, the fundamental mode experiences nearly 100× lower loss when compared to the lowest loss of a higher-order mode. The loss ratio can even be further enhanced when the fibre is bent or specifically engineered to match the application requirements. Concerning the HC-CAF, in [141], it is shown that the fibre can support the propagation of higher order optical modes which get suppressed after a length of about 15 m.

6.3.2 Overlap between optical and acoustic modes

In this section, we will study the optical and acoustic modes in our gas-filled hollow-core fibres, as the overlap between the fundamental optical and acoustic modes indicates the efficiency in the coupling between the light and sound waves. Later, in chapter 7, we will study Brillouin scattering in gas-filled hollow-core fibres, and how the Brillouin gain scales inversely with the acousto-optic effective area which we will study in this section.

The study is conducted by means of a finite element method simulation using the COMSOL Multiphysics software, more specifically the two-dimensional "Electromagnetic waves" and "Pressure acoustics" modules. The silica refractive index $n_{\text{silica}} = 1.44$ and the gas refractive index $n_{N_2} = 1.0002697$ at atmospheric pressure and $n_{N_2} = 1.0093304$ for 35 bar of N_2 were entered into the calculation of the optical modes. The effective refractive index of the fundamental optical mode n_{eff} was calculated to be 1.0088004 at a wavelength of 1.55 µm. At 35 bar of N_2, the gas density $\rho_{N_2} = 29.6$ kg/m^3 (using the ideal gas approximation) and the acoustic velocity $v_a = 358.5$ m/s (as deduced from the Brillouin frequency shift of our measurement) were used to calculate the acoustic mode in the fibre core, considering a sound hard boundary on the hollow tube wall. The acoustic mode profile of the excited modes were calculated for an out-of-plane wavenumber $\beta_{\text{ac}} = 8.107 \times 10^6$ rad/m ($\beta_{\text{ac}} = 2 \times \beta_{\text{op}}$ with $\beta_{\text{op}} = \frac{2\pi n_{\text{eff}}}{\lambda}$ as the propagation constant of the optical mode [8]) at a resonant frequency of 465 MHz, which corresponds to the measured Brillouin frequency shift at 35 bar of N_2 gas. Using the simulation, we calculated the effective area of the fibres from which we deduced the mode-field diameter (MFD). The MFD is a quantity that represents the transverse extent of electromagnetic field intensity of an optical mode within an optical fibre's cross-section. The effective area for nonlinear effects

along with the MFD are expressed as follows [149]:

$$A_{\text{eff}} = \frac{\left(\iint_S \left|\overrightarrow{E_t}\right|^2 \text{dxdy}\right)^2}{\iint_S \left|\overrightarrow{E_t}\right|^4 \text{dxdy}} \longrightarrow \text{MFD} = \frac{2}{\sqrt{\pi}} \sqrt{A_{\text{eff}}} \tag{6.5}$$

where $\overrightarrow{E_t}$ denotes the transverse electric field vector and S represents the entire cross-section of the fibre. The values for the physical core diameter and area along with the MFD and the A_{eff} for the different hollow-core fibres are given in table 6.1.

For the analysis of the acoustic modes, a finite element method simulation was performed, using the acoustic, frequency domain module in the gas and the solid mechanics, frequency domain module for the silica capillaries. We will assume that the silica walls are rigid for the acoustic wave under consideration, as it was shown in [13] that the theoretical solution of the acoustic Helmholtz equation for cylindrical coordinates assuming a rigid silica wall and the simulation are in good agreement. With this simulation, we can compute the acousto-optic effective area A_{ao}, indicating the excitation strength of the acoustic mode under consideration, as given by [150]:

$$A_{\text{ao}} = \left(\frac{\int I_{\text{opt}} \text{d}A}{\int P \cdot I_{\text{opt}} \text{d}A}\right)^2 \cdot \int P^2 \text{d}A \tag{6.6}$$

where I_{opt} is the intensity profile of the optical mode under consideration, P is the pressure profile of the dominant acoustic mode considered in the simulation and $\int \ldots \text{d}A$ designates the two-dimensional integral over the whole fibre cross-section. The acousto-optic effective area along with the acousto-optic overlap $\left(\frac{A_{\text{eff}}}{A_{\text{ao}}}\right)$ values for the different hollow-core fibres are given in table 6.1. We simulate the overlap between the fundamental optical mode and 100 acoustic modes. In Fig. 6.4, we show the fundamental optical modes for all the gas-filled hollow-core fibres used in the experiments and the acoustic modes that have the largest overlap with the fundamental optical mode. From the finite element method simulation, we obtained the fundamental optical mode along with the overlapping fundamental acoustic mode for the

Table 6.1 – Values for the core diameters, the cross-sectional areas, the mode-field diameters, the effective areas, the acousto-optic effective areas, and the acousto-optic overlap $\left(\frac{A_{\text{eff}}}{A_{\text{ao}}}\right)$ for the bandgap PCF, the conjoined-tube ARF (CAF), and the revolver ARF (RAF).

Parameter	Fibre type		
	PCF	CAF	RAF
Core diameter (μm)	10	22	35
Core area (μm^2)	79	380	962
MFD (μm)	8	16	24
A_{eff} (μm^2)	50	197	452
A_{ao} (μm^2)	80	340	905
Acousto-optic overlap	0.63	0.58	0.50
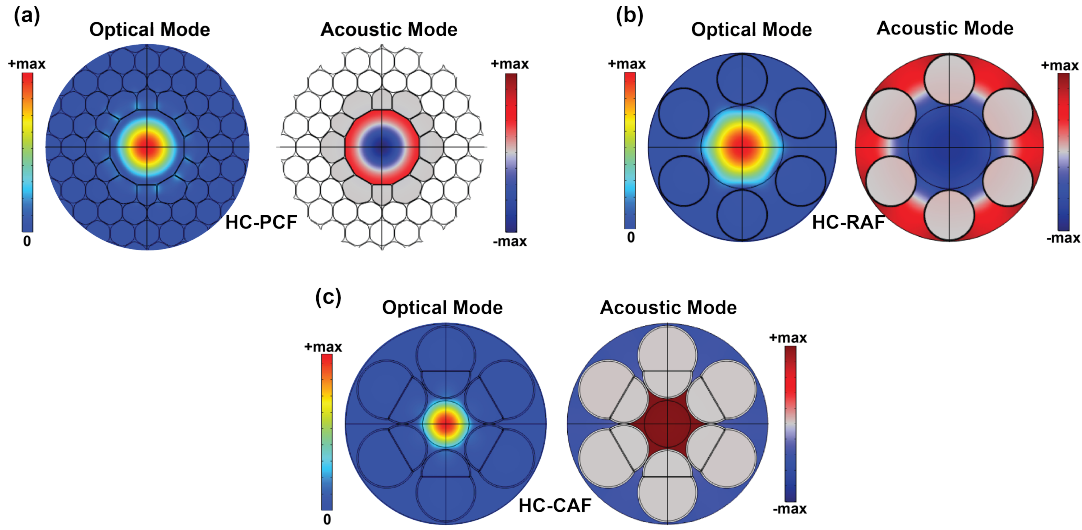
Figure 6.4 – Graph showing the fundamental optical mode along with the fundamental acoustic mode for the fibres utilised in the experiments. The acoustic modes illustrated represent the dominant acoustic mode with the highest acousto-optic overlap. (a) HC-PCF; (b) HC-RAF; and (c) HC-CAF; Note: The circle in the centre of the anti-resonant fibres does not indicate any boundary and is only used for visualisation purposes. The visual representation of the fibres may be slightly misleading, therefore the correct dimensions of the fibres are indicated in table 6.1.

HC-PCF which can be seen in Fig. 6.4 (a). We can see that there is only one acoustic mode within 100 simulated acoustic modes that has a large enough overlap to be considered. Higher order acoustic modes in gas-filled HC-PCF show an acousto-optic overlap effective area that is more than two orders of magnitude larger and their coupling with the fundamental optical mode is accordingly negligible. For the HC-RAF, we obtained the fundamental optical mode and the dominant acoustic mode with the highest effective overlap seen in Fig. 6.4 (b). By dominant acoustic mode we mean the acoustic mode that shows the highest acousto-optic overlap. The structure of a gas-filled RAF allows the excitation of acoustic modes in the gas (gas modes) and in the silica capillaries (capillary modes). The capillary modes would dominate at low gas pressure, and at high gas pressure the dominating modes would be the gas modes [151]. Fig. 6.4 (c) shows the fundamental optical mode and the dominant acoustic mode for the HC-CAF.

6.4   Heat conduction in gas-filled hollow-core fibres

In section 2.3.5, we presented the acoustic attenuation in gas and how it is related to fundamental thermodynamic quantities like the thermal conductivity. Unlike the thermal conductivity κ of silica which is 1.3 W/(m K) at room temperature [152], the thermal conductivity for gases is much lower and is about 25.9×10^{-3} W/(m K) for N_2 and 16.8×10^{-3} W/(m K) for CO_2 as
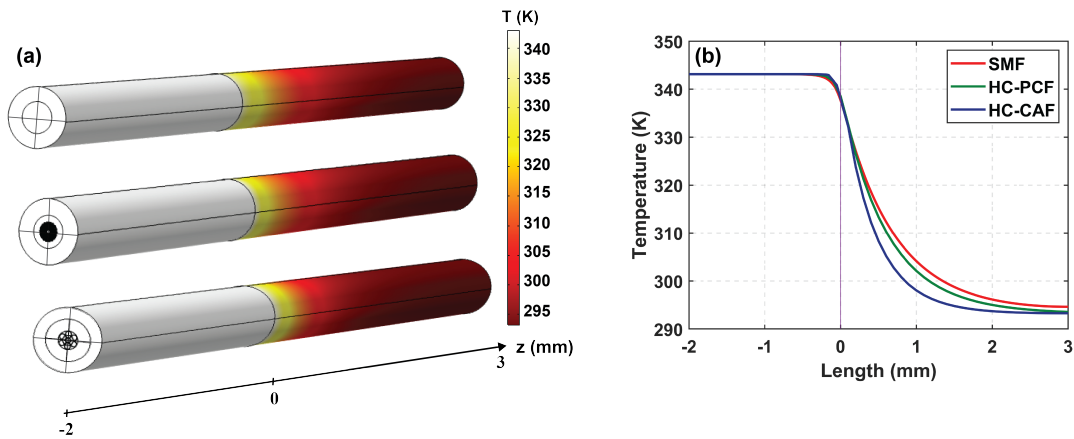
Figure 6.5 – Finite element method simulation to compare the heat conduction of standard SMF, HC-PCF, and HC-CAF. (a) 3-D view of the surface temperature for an SMF (upper fibre), a HC-PCF (middle fibre), and a HC-CAF (lower fibre); (b) Temperature profile in the cores (central axis), along the z-axis of all three fibres. The single-mode fibre and the HC-PCF show similar behaviour, whereas the HC-CAF shows a slightly sharper transition due to the lower thermal conductivity of the gas in comparison to silica. Note: The dimensions of the fibres are not to scale.

indicated further in chapter 7 in tables 7.3 and 7.4, respectively. In principle, the lower thermal conductivity impedes the longitudinal heat propagation from a sharp hot spot to the rest of the fibre and creates favourable conditions for achieving high resolution distributed temperature sensing. A finite element method simulation has been conducted to compare the heat conduction of a standard silica single-mode fibre along with two hollow-core fibres, namely HC-PCF and HC-CAF. A constant 343.15 K of temperature is applied on the surface of the three coated fibres along a length of 2 mm, starting from their left far end as can illustrated in Fig. 6.5 (a). For the three fibres, the coating is taken as a 58.5 m thick acrylate PMMA. For the remaining length of the fibres, their surface is exposed to a 293.15 K convective natural air flow. 35 bar of N_2 gas is applied in the hollow portion of the HC-PCF and the HC-CAF. The results are presented in Fig. 6.5 (b) and show that the benefit is actually of limited extent in the case of the HC-PCF when compared to the silica fibre. There is still a slight difference in the curves, and this is directly attributed to the lower thermal conductivity of the N_2 gas when compared to silica. For the case of the HC-CAF, we can clearly observe a relatively sharper transition when compared to the two other fibres. This can be explained by the fact that the N_2-to-silica area ratio of the fibre cross-section is higher in the case of the HC-CAF than in that of the HC-PCF, since the HC-CAF has relatively lower silica content than the HC-PCF.

6.5   Summary

In this chapter, we present the characteristics of the fibres that will be employed for the experimental demonstrations of the next chapter. With the help of the finite element method

simulation, we calculate the acousto-optic effective overlap areas between the fundamental optical and acoustic modes inside gas-filled hollow-core fibres. The values of the acousto-optic effective overlap areas will be utilised for the theoretical estimation of the Brillouin gain coefficient in the coming chapter. We take advantage of the low heat conduction coefficient in gas and finally simulate the heat conduction in a standard silica fibre and compare it with a HC-PCF and a HC-CAF. From our results, we conclude that due to the higher silica content in HC-PCFs, their behaviour in terms of heat conduction is probably very similar to standard silica fibres. However, in the case of HC-CAF, heat conduction is lower due to the lower silica content inside the fibre.

7 Experimental demonstrations using gas-filled hollow-core fibres

7.1 Gas cell preparation

The first step into starting the experiments using hollow-core optical fibres is the gas cell preparation. It is a very crucial step because it has to be done meticulously to guarantee a hermetically-sealed gas cell with very low loss. Two main factors need to be taken care of, namely the transmission loss and the end-face reflections. We will further explain how the gas cells were assembled for the experiments and provide some tips for the most efficient gas cell making.

7.1.1 The coupling of light and gas

Several techniques have been demonstrated in the literature for the purpose of coupling light and gas into hollow-core fibres. In [153], one end of the HCF was fusion-spliced with an SMF, and the fibre was evacuated and then filled with the desired gas from the remaining open end. Afterwards, the loose end was spliced with another SMF, thereby sealing the gas and creating a compact and durable gas cell. In this case, however, no change of gas is possible and the cell has to be destroyed and re-made to be used for another gas. Other studies [154, 155] showed very low interconnection losses between hollow-core fibres and standard SMFs using gluing instead of splicing to avoid any damage to the fibre's micro-structures. In a different study [156], low-loss micro-machining was performed on HCF to yield a milled channel through which fluid can flow into the HCF. This way low-loss splicing can be achieved and the change of fluid is also possible without destroying the gas cell.

In the following sections, we will present the technique opted for to achieve the coupling of light and gas. It is adapted from previous works [48, 157, 158].

7.1.2 All-fibre gas cell

The gas cell realised in this work is an all-fibre gas cell. The end of the hollow-core fibre is finely cleaved in a flat manner and the SMF end facet is cleaved with an angle. Ideally, the angle should be as large as possible to minimise the Fresnel backreflections as much as possible. However, a way too large cleave angle may also result in difficulty for light coupling. That is why, the angle needs to be adjusted in such a way that the reflections are minimal and the coupling loss is the smallest to ensure high transmission efficiency. Depending on the fibres used, the proper angle needs to be chosen, but in general an angle of about 7° to 8° should yield acceptable performance of the cell in terms of coupling loss and Fresnel reflections [159]. A perfect cleave needs several trials to be yielded, and after that the cleaved fibre ends will be butt-coupled. To have a rough estimation on the possible loss due to mode field mismatch α_{mfm} between the two coupled fibres, the following expression is utilised [160, 161]:

$$\alpha_{\text{mfm}} = -20 \log \left(\frac{2 \omega_{\text{HCF}} \omega_{\text{SMF}}}{\omega_{\text{HCF}}^2 + \omega_{\text{SMF}}^2} \right) \tag{7.1}$$

where ω_{HCF} and ω_{SMF} are the mode field diameters of the hollow-core fibre and the SMF, respectively. It should be noted though that the expression presented in Eq. 7.1 is used to
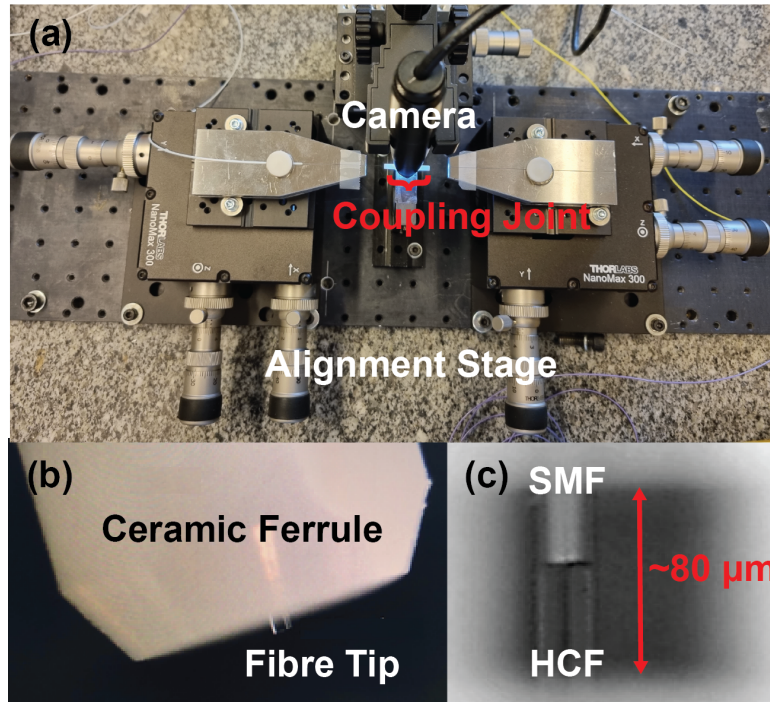
Figure 7.1 – Illustration showing the making of the gas cell; (a) Alignment stage where the butt-coupling is achieved; (b) Fibre inserted in ceramic ferrule used to for the ease of alignment with the fibre tip showing; (c) Ferrule-to-ferrule junction which has a width in the order of µm showing the butt-coupling between the angle-cleaved SMF and the flat-cleaved HCF.

estimate the loss between two flat-cleaved end-facets. When there is an angle, the loss may be slightly higher, but Eq. 7.1 can still be used as a rough estimation.

As can be seen in Fig. 7.1 (a), the two fibres to be butt-coupled are aligned on a translation stage where each fibre end is inserted and glued into a ceramic ferrule which can be observed in Fig. 7.1 (b). The ferrules are tucked in a ceramic sleeve which has a side opening that enables us to properly align the fibres using a camera. This configuration of ferrule-sleeve-ferrule will be further referred to as coupling joint. Fig. 7.1 (c) shows the two fibres being coupled and highlights the size of spacing between the ferrules which is in the order of 10s of µm. The spacing between the fibres is adjusted according to transmission loss measured. The coupling is performed on the two sides of the HCF to be able to measure the transmission loss. The two coupling joints on each side of the HCF are then pulled and placed inside of stainless steel tubes which form the hermetically-sealed gas-cell illustrated in Fig. 7.2. The sealing of the tube ends is achieved using epoxy glue to avoid any gas leakage. This step needs meticulousness to ensure that the glue covers the tubes properly. One way of gluing the tube ends would be fixing the cell vertically, so that the glue can penetrate in the cell using the gravitational force. However, it is recommended to use a rather viscous glue to ensure that the glue does not reach the coupling joint and prevents the gas from entering through the side hole of the sleeve. If after the glue hardens, one observes that there is gas leakage from the cell, it is still possible to fix the leakage by applying small drops of epoxy while the cell is being vacuumed. This way the epoxy glue gets sucked in into the leaking grooves. As can be seen, the cell is made of stainless steel tubes which are connected to each other, three valves, two gas inlets/outlets, and one pressure metre. This configuration helps controlling the gas flow within the cell and achieving high purity of the gas by performing several rounds of vacuuming and purging before reaching the steady-state condition of the gas. Especially when
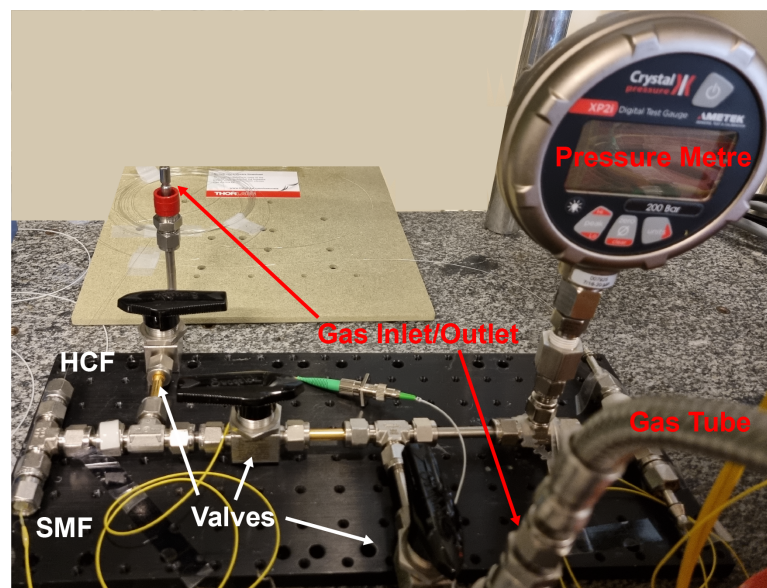
Figure 7.2 – Graphic showing the final look of the gas cell assembly.

using heavier gases such as CO_2 or SF_6 for example, nitrogen purging is necessary to avoid the occurrence of inevitable gas mixing. It is highly crucial to make sure that the gases are as pure as possible because any small impurities can have a dramatic effect on the acoustic attenuation. The pressure metre in the cell is needed to keep track of the gas-cell pressure at all times.

While preparing the gas cell, the transmission loss along with the Fresnel reflections are measured at all times. Depending on the mode field mismatch governed by Eq. 7.1, the coupling loss varies. We prepared several gas cells, and made sure to always attain a maximum reflection of ~ -55 dB. The total insertion loss due to the coupling was measured to be between ~ 8 and ~ 12 dB. It should be noted that in our experiments, only one end is needed to conduct the measurement, but it was necessary to perform the coupling on the two end of the HCF to be able to measure the gas cell loss. The coupling between the fibres can be either done by splicing or by butt-coupling as we do here, which facilitates the use of different gases in the same cell. Depending on the application, one can choose the most suitable technique. It is also possible to splice one end and have a coupling joint in the other end, and accordingly take advantage of the best in both worlds.

7.1.3 Gas filling time

One important parameter to be taken into consideration while filling the cell with gas is the filling time. When the density is sufficiently large (i.e. density at atmospheric pressure), the gas flow in a HCF is in the hydrodynamic regime and the flow can be approximated by the Poiseuille flow of an ideal gas using the following differential equation for a pressure $P(z, t)$ along the z-axis of the fibre [162]:

$$\frac{\partial P}{\partial t} = \frac{D^2}{32\eta_s} \frac{\partial}{\partial z}\left(P \frac{\partial P}{\partial z}\right) \tag{7.2}$$

where D is the fibre core diameter and η_s is the shear viscosity. For a sudden applied pressure, P at the two fibre ends and with a negligible initial pressure which is much smaller than P, the filling time t_f is given by [163]:

$$t_f = \frac{32\eta_s L^2}{P_0 D^2} \tag{7.3}$$

where L is the fibre length. Using this equation, the approximate filling time of N_2 gas with $\eta_s = 18 \times 10^{-6}$ Pa·s inside the core diameters of different HCF are given in Table 7.1 for various lengths. It is worth noting that the values in the table are calculated based on the ideal case that the cores are circular. In reality, however, during the fabrication of the fibres, the shape of the cores may differ and the values in the table may also change accordingly. As apparent from Eq. 7.3, an increase in the shear viscosity results in a longer filling time. This means that for other gases which have lower shear viscosities (e.g. CO_2 has $1.2\times$ lower shear viscosity than N_2 ($\eta_s = 15 \times 10^{-6}$ Pa·s), the filling time will be $1.2\times$ faster. Furthermore, t_f is directly dependent

Table 7.1 – Typical filling times of different hollow-core fibres for various lengths. The gas used is N_2 at 40 bar for a fibre core diameter of $D = 10\,\mu m$ for the bandgap PCF, $D = 22\,\mu m$ for the conjoined-tube ARF (CAF), and $D = 35\,\mu m$ for the revolver ARF (RAF).

Length	Filling time		
	PCF (10 µm)	CAF (22 µm)	RAF (35 µm)
50 m	60 minutes	12 minutes	4.8 minutes
100 m	240 minutes	48 minutes	19 minutes
1 km	16 days	3 days 9 hours	1 day 8 hours
5 km	1 year 51 days	84 days	34 days
10 km	4 years 206 days	337 days	136 days

on L^2 and inversely proportional to D^2 and the pressure P. From the expression, it is obvious that the length and the diameter of the HCF are the dominating parameters which influence the filling time.

In this configuration which is mentioned above, the targeted pressure inside the HCF is the same as that applied to the fibre. To reduce the filling time, however, it is possible to apply higher pressure to yield the targeted pressure in lower time. For this configuration, the right hand-side of Eq. 7.3 can be multiplied by a factor [162], so that the calculated time represents the instant at which the pressure in the whole fibre is equal to the targeted pressure. This indicates that a relatively high applied pressure, which is much higher than the targeted pressure, will yield a much faster filling time. For example, if a pressure of 1000 bar is applied, but it is intended to reach a uniform pressure of 35 bar inside the cell, the filling time of a 10 km HC-PCF will only be a few days as compared to nearly 5 years. The same of course applies to the other fibres, and due to their larger core diameters, the time it will take to uniformly fill them will be even lower. It should be noted, however, that one should account for the time that the gas will take to be uniformly distributed and stabilise in the entire fibre.

When it comes to gas evacuation, Graham's law of effusion can be applied. Effusion describes the process when gas molecules escape through a hole —smaller than their mean free path —into vacuum. The lighter gases pass through the small openings more rapidly (at a higher rate) than the heavier ones, as the rate of effusion is inversely proportional to the square-root of the molar mass M_m, $r_{\mathrm{Eff}} = \frac{1}{\sqrt{M_m}}$. In this case, when the gas cell is vacuumed, heavier molecules will take slightly more time to be entirely evacuated. N_2 ($M_m = 28$ g/mol), for example, will effuse $1.2\times$ faster than CO_2 ($M_m = 44$ g/mol).

7.2 Detection of spontaneous Brillouin scattering

After having prepared the gas cell and filled it with gas, we will now discuss how the measurement of the Brillouin scattering is achieved. As already mentioned earlier, in this thesis, we only use reflectometres for the measurements of the scatterings occurring in the fibres. Reflectometres require solely one end of the fibre for the measurement which is a significant

advantage with respect to other techniques that require the two ends of the fibres. Problems, however, may arise if the back-scattered signals are too weak to be detected. In this section, we will thus explore two commonly-utilised techniques for the detection of Brillouin scattering which only rely on one end of the fibre for the detection of the signals.

7.2.1   Reflected power of spontaneous Brillouin scattering

Firstly, let us calculate the backreflected power coefficient R_B due to Brillouin back-scattering (considering the Stokes process) which is given by [164, 165]:

$$R_B = Y_B e^{G_B/2} \left(I_0 \left(G_B/2 \right) - I_1 \left(G_B/2 \right) \right) \tag{7.4}$$

where I_m are the modified Bessel functions of the first kind of m-th order. The linear gain G_B is described as follows:

$$G_B = g_B P_P L \tag{7.5}$$

with P_P as the input pump power and L as the length of the waveguide under test. The parameter Y_B in Eq. 7.4 is written as:

$$Y_B = \frac{\pi}{2} (\bar{n} + 1) g_B h \nu_P \Delta\nu_B L \tag{7.6}$$

where h is the Planck's constant, ν_P is the frequency of the input pump light, and $\Gamma_B = 2\pi\Delta\nu_B$ is the acoustic damping rate. The mean number of phonons $\bar{n}$ per acoustic mode (with a frequency ν_B) at a temperature T is given by the following expression representing the Bose-Einstein distribution:

$$\bar{n} = \left(e^{\frac{h\nu_B}{k_B T}} - 1 \right)^{-1} \tag{7.7}$$

where k_B is the Boltzmann constant. Since we are dealing with small gains $G_B << 1$, which is the case when the reflected light originates entirely from the scattering of the laser field by spontaneously (i.e. thermally) generated phonons, we can approximate the reflection coefficient to $R_B \approx Y_B$ and the reflected power to:

$$P_{\text{SpBs}} = R_B P_P \approx Y_B P_P = \frac{\pi}{2} (\bar{n} + 1) h \nu_P \Delta\nu_B G_B \tag{7.8}$$

Using Eq. 7.8 and rearranging, while considering the possible losses (coupling and path losses), we finally yield the Brillouin gain measured experimentally. The value of P_{SpBs}, however, needs to be calibrated, and we will show how in section 7.3.

7.2.2   Detection techniques for spontaneous Brillouin scattering

In this section, we explore two experimental techniques commonly employed to evaluate the Brillouin interaction and are utilised for the detection of spontaneous Brillouin scattering (i.e. single-ended measurement). There is, of course, a myriad of experimental methods to measure Brillouin scattering, but here, and as for the rest of the thesis, we only consider single-ended experimental setups.

Direct-detection experimental system

One of the detection techniques consists in shooting a high-power continuous-wave pump light from port 1 of a circulator through port 2 into the waveguide under consideration. The backscattered spontaneous Brillouin signal then passes through port 3 of the circulator and can directly be measured by means of an optical spectrum analyser (OSA). The OSA can also be replaced by using a stage containing an optical filter (to get rid of Rayleigh scattering or any end-facet reflections) followed by a photo-detector (PD) for the detection of the back-scattered light. It should be noted that this experimental implementation also detects signals at DC frequency.

In a direct-detection system, the whole backreflected signal having a power of P_{SpBs} is captured by the photo-detector. The signal-to-noise ratio (SNR) in the electrical domain can be written as [164]:

$$\text{SNR} = \frac{\langle i_s^2(t)\rangle}{\langle i_{\text{th}}^2\rangle} \tag{7.9}$$

where $\langle i_s^2(t)\rangle$ is the mean-square signal current and $\langle i_{\text{th}}^2\rangle$ describes the mean-square current due to the photo-detector's thermal noise which is the dominant noise at low light intensity. These two quantities can be expressed as follows:

$$\langle i_s^2(t)\rangle = R_{\text{PD}}^2\, P_{\text{SpBs}}^2 \qquad\qquad \langle i_{\text{th}}^2\rangle = R_{\text{PD}}^2\, B_{\text{PD}}\, (\text{NEP})^2 \tag{7.10}$$

with R_{PD} as the photo-detector responsivity (in units A/W), NEP as the photo-detector's noise-equivalent power (NEP) and B_{PD} as the detection bandwidth.

Now, let us assume that we have an SNR = 1, and we are interested to find the minimum linear gain possible for this SNR using a direct-detection scheme. By rearranging Eq. 7.8 to solve for the linear gain and substituting the equations from Eq. 7.10, we yield the following equation:

$$G_{\text{min, dd}} = \frac{2\sqrt{B_{\text{PD}}}\,\text{NEP}}{\pi h \nu_P (\bar{n}+1)\Delta\nu_B} \tag{7.11}$$

As can be inferred from Eq. 7.11, the gain G_{min} can theoretically-speaking be as minimum as possible yet still be detected if there is the choice to largely reduce the photo-detector bandwidth. This, however, causes a significant increase in the measurement time. In real-life,

nevertheless, the minimum gain detected using this technique is limited due to the inevitable detection of signals at DC frequency, as the gain will be buried under the low-frequency noise if it is too small.

Homodyne-detection experimental system

In contrast to direct detection, a homodyne-detection system relies on the principle of two signals beating at the photo-detector. In this case, a portion of the pump beats with the backreflected spontaneous Brillouin signal and the detection is performed at the frequency of the Brillouin frequency shift (BFS). In turn, if the BFS is very large, a fast photo-detector will be required which may be an impairing factor when using homodyne detection compared to direct detection which does not have this requirement.

Since in this scheme two signals are beating, namely the spontaneous Brillouin optical signal and a strong local oscillator (LO) (a portion of the pump light), the photo-detector current will then be expressed differently than for direction detection and will take the following form:

$$\langle i_s^2(t) \rangle = R_{PD}^2 \, P_{SpBs} \, P_{LO} \tag{7.12}$$

where P_{LO} is the power of the local oscillator. It ought to be remarked that by using homodyne detection and a low thermal-noise photo-detector, shot-noise-limited measurements can be achieved as a result of the relatively high power of the local oscillator (just below the photo-detector saturation). Accordingly, the shot noise ($\langle i_{sh}^2 \rangle$) will be added to the SNR expression as follows:

$$SNR = \frac{\langle i_s^2(t) \rangle}{\langle i_{th}^2 \rangle + \langle i_{sh}^2 \rangle} \tag{7.13}$$

where $\langle i_{sh}^2 \rangle = 2 \, q \, B_{PD} \, R_{PD} \, P_{LO}$ is the shot noise of the local oscillator with q as the electron charge magnitude. Following a similar procedure as for direct detection, the minimum detectable gain with a SNR equal to one is:

$$G_{min, \, hd} = \frac{2 B_{PD} \, NEP^2}{\pi h \nu_P (\bar{n} + 1) \Delta \nu_B P_{LO}} + \frac{4 q B_{PD}}{\pi R_{PD} (\bar{n} + 1) \Delta \nu_B} \tag{7.14}$$

Using equations 7.11 and 7.14, in table 7.2 we summarise the minimum detectable gains for direct-detection and homodyne-detection systems with a reasonable choice of parameters for two different gases, namely 40 bar of N_2 gas and CO_2 gas. As apparent from the table, with homodyne detection, the detection of gains as weak as $G_{min, \, dd} \approx 10^{-9}$ can be achieved. This is 10 million times better than direct detection. It should be noted, however, that the photo-detector noise-equivalent power at high frequency is usually much higher than that the low-frequency value indicated in the datasheet. Accordingly, and since the minimum gain for homodyne detection shows a square dependence on the noise-equivalent power, larger noise-equivalent power values can result in the raise of the minimum detectable gain by

orders of magnitude. From this analysis, we can conclude that using a homodyne-detection system is quite suitable for us to benefit from the detection of very small gains, as the Brillouin frequency shift of gases is quite low as can be seen in table 7.2, so there is no limitation in terms of photo-detector bandwidth. In the following section, we will present the homodyne experimental setup employed in our Brillouin gain measurements along with the results of the measurement.

Table 7.2 – Minimum gains calculated for direct-detection and homodyne-detection systems for a $B_{PD} = 10$ Hz, an SNR = 1, an NEP = 20×10^{-12} W/$\sqrt{Hz}$ and a $R_{PD} = 1$ A/W for two different gases.

Gas	ν_B (MHz)	$\Delta\nu_B$ (MHz)	$G_{min, dd}$ ($\times 10^{-3}$)	$G_{min, hd}$ ($\times 10^{-10}$)
N_2	465	13	1.3	1.4
CO_2	325	4.1	4	4.6

7.3 Brillouin gain measurement

7.3.1 Gain measurement experimental setup

The experimental setup opted for in the measurements of the Brillouin gain spectra is that corresponding to the homodyne-detection technique mentioned in the previous section. Fig. 7.3 shows the experimental setup where the laser used is a Toptica CTL1550 external-cavity diode laser (ECDL) with a 10 kHz linewidth. The light is then guided into two branches using a 90/10 coupler. 10% of the laser light is amplified by an Erbium-doped fibre amplifier (EDFA) which is followed by a polarisation controller (PC). The light hereafter passes from port 1 of the circulator through port 2 into the HCF under test. The average power measured at the input of the HCF is about 33 dBm. The HCF is filled with gas at different pressures. The backreflected light is then transmitted from port 2 to port 3 and reaches a balanced-detection
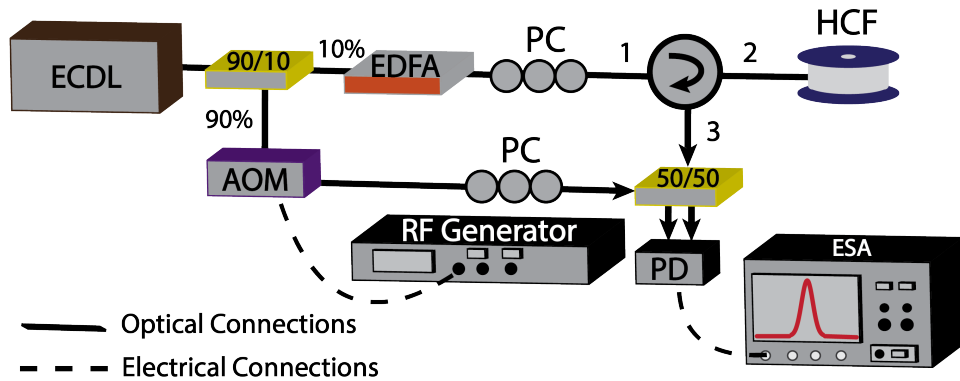
Figure 7.3 – Experimental setup for the measurement of the Brillouin gain spectrum (BGS) (ECDL: External-cavity diode laser, EDFA: Erbium-doped fibre amplifier, PC: Polarisation controller, AOM: Acousto-optic modulator.
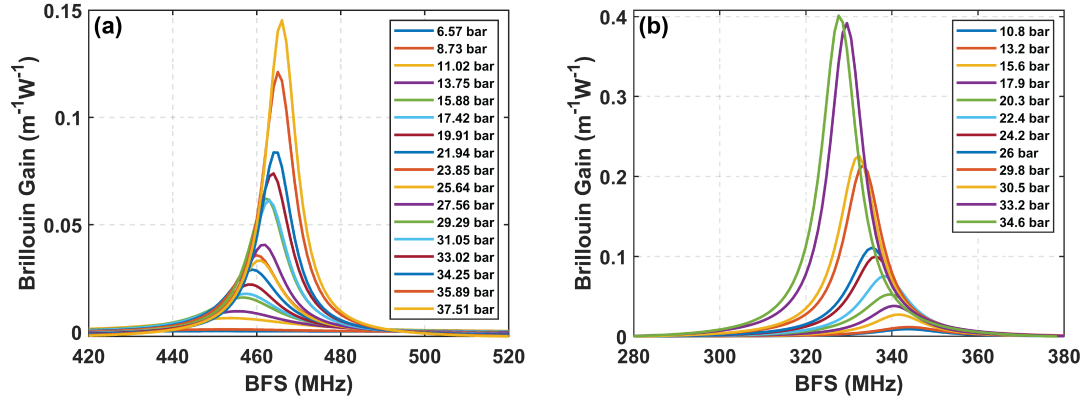
Figure 7.4 – Examples of Brillouin gain spectra fitted by a Lorentzian distribution of two gases at different pressures: (a) N_2 gas and (b) CO_2 gas. Note that the curves are symmetric, and there is no skewing on either side.

photo-detector (PD). The 90% of the light that is guided through the second branch (local oscillator) passes through an acousto-optic modulator (AOM) which is connected to a radio frequency (RF) generator whose amplitude is set to -22.5 dBm and its frequency to 110 MHz. Accordingly, the frequency of the local oscillator is shifted by 110 MHz from the initial centre frequency. This way, the Stokes and anti-Stokes Brillouin components can be distinguished and do not fall on the same frequency in the spectrum. The light then passes through another PC, then arrives at the PD. The average power measured at the PD is about -2 dBm. Heterodyne beating between the two branches occurs at the PD, and the Brillouin gain spectrum (BGS) for the whole fibre (as seen in Fig. 7.4) is acquired by an electrical spectrum analyser (ESA). The settings of the ESA are set to be the following:

- Radio bandwidth (RBW) and Video bandwidth (VBW): 1 MHz

- Frequency span: 1 GHz

- Time averaging: 1000

- Mechanical attenuation: 0 dB

When two signals are coupled by a 50/50 coupler to beat at a balanced detector, the electrical amplitude measured is:

$$E \propto \sqrt{P_1 P_2} \tag{7.15}$$

where P_1 and P_2 are the optical powers of the two signals beating at the photo-detector. Accordingly, the electrical power is equal to:

$$P_E \propto E^2 \propto P_1 P_2 \implies P_E = \alpha_c P_1 P_2 \tag{7.16}$$

where α_c is a conversion coefficient, which should be constant given that the same photo-detector and the same ESA are used. All the settings chosen in the ESA (e.g. RBW, VBW, scan

range, attenuation, sampling points, etc.) should remain the same. From the power spectrum measured by the ESA, we can calculate the overall electrical power P_E by integrating over the frequency range, which is written in the form of a discrete summation as given by the following expression:

$$P_E = \sum P_{E,i} \Delta f = \Delta f \sum P_{E,i} \tag{7.17}$$

where $P_{E,i}$ and Δf are the observed electrical power at each sampling point in the spectrum and the frequency step between two sampling points, respectively. Hence, α_c can be calculated with a calibration process (see section 7.3.2), using a beating signal, whose beating frequency is the same as the Brillouin scattering and the optical powers of the two optical signals P_1 and P_2 are known. By substituting Eq. 7.16 into Eq. 7.17 and solve for α_c, we yield the following expression:

$$\alpha_c = \frac{\Delta f \sum P_{E,i}^{\text{calib}}}{P_1 P_2} \tag{7.18}$$

Once α_c is obtained, the power of the backreflected Brillouin signal can be calculated using the optical power of the local oscillator P_{LO} and the measured electrical power spectrum $P_{E,i}^{\text{SpBs}}$ as follows:

$$P_{\text{SpBs}} = \frac{P_1 P_2 \sum P_{E,i}^{\text{SpBs}}}{P_{LO} \sum P_{E,i}^{\text{calib}}} \tag{7.19}$$

The value of P_{SpBs} is then substituted in Eq. 7.8 to calculate the linear gain G from which the experimental Brillouin gain coefficient g_B is obtained. The experimental as well as the theoretical values of g_B as a function of the gas pressure are presented in section 7.3.3.
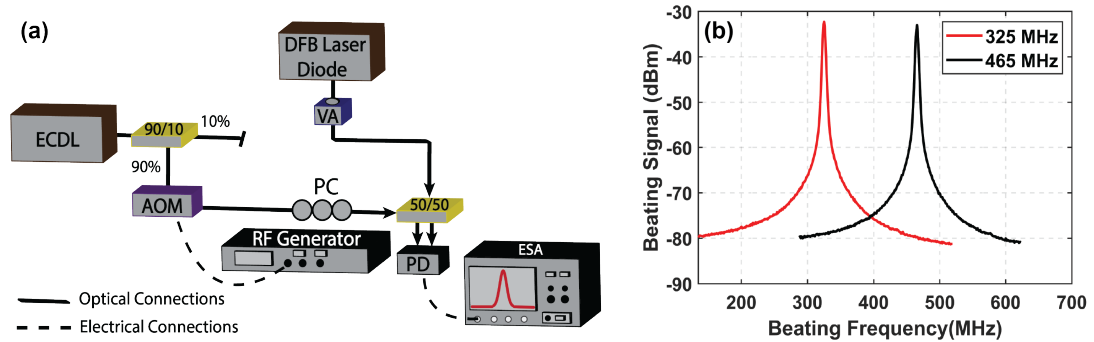
Figure 7.5 – (a) Calibration setup; (b) Calibration spectra for the two different BFS of CO_2 (around 325 MHz) and N_2 (around 465 MHz).

Parameter	Symbol	Value
Molar Mass	M_m	28.014 g/mol
Shear Viscosity	η_s	18 µPa s
Bulk Viscosity	η_b	13 µPa s
Thermal Conductivity	κ_C	25.9×10^{-3} W/(m K)
Heat Capacity (constant pressure)	C_P	1041 J/kg K
Heat Capacity (constant volume)	C_V	743 J/kg K
Derivative of C_P	dC_P/dT	0.0082 J/kg K^2
Derivative of C_V	dC_V/dT	0.0175 J/kg K^2
Second Virial Coefficient	B	-4.7×10^{-6} m^3/mol
Derivative of B	dB/dT	1.93×10^{-7} m^3/K mol
Second Derivative of B	d^2B/dT^2	-1.5×10^{-9} m^3/K^2 mol
Third Virial Coefficient	C	14×10^{-10} m^6/mol^2
Derivative of C	dC/dT	-2.5×10^{-12} m^6/K mol^2

Table 7.3 – Values used for the theoretical calculation using N_2 gas at a constant temperature of $T = 298.15$ K [30, 166–168].

7.3.2 Calibration setup

The Stokes and anti-Stokes powers are calibrated by using the calibration setup depicted in Fig. 7.5 (a). A distributed feedback (DFB) laser diode is used whose signal beats with the signal that is coming from the second branch of the Brillouin gain measurement setup (Fig. 7.3) which has an ECDL as the laser source. The power from the DFB laser is adjusted by means of an attenuator such that the DFB laser power reaching the 50/50 coupler is about -10 dBm. The calibration is carried out by measuring the response of the photo-detector at the frequencies of interest, and accordingly we tune the frequency difference between the DFB laser and the ECDL to be around region of the Stokes beating frequency (465 MHz for N_2 gas and 325 MHz for CO_2 gas). The beating spectra at these two frequency regions are shown in Fig. 7.5 (b). The information about the powers from the calibration setup is used in Eq. 7.19 to calculate the power of the backreflected Brillouin signal.

7.3.3 Results

Using the experimental setup presented in Fig. 7.3, we were able to acquire the Brillouin gain spectra of different gas-filled fibres using N_2 gas and CO_2 gas. The experimental demonstration was conducted using one hollow-core bandgap photonic-crystal fibre (HC-PCF), and two anti-resonant fibres (ARFs) which are the hollow-core conjoined-tube ARF, and the revolver ARF. We will further see in the coming section that the difference in the Brillouin gain values with respect to different fibres is mainly attributed to the dissimilar core dimensions of the fibres.

Figure 7.6 – Graphs showing different parameters as a function of the gas (N_2) pressure: (a) Brillouin gain; (b) Brillouin frequency shift; (c) Brillouin linewidth; and (d) Acoustic velocity.

Nitrogen (N_2) gas

Fig. 7.6 shows the graphs of a number of parameters as functions of the applied gas pressure. As can be seen in Fig. 7.6 (a), the Brillouin gain is increasing with a square dependence with respect to the increase of gas pressure. The circles represent the experimental values obtained during the measurement (refer to section 7.3.1), and the solid lines correspond to the theoretical estimation of the gain using Eq. 2.65. All values used for the theoretical calculation are in included in Table 7.3. From Eq. 2.65, it is apparent that the Brillouin gain is inversely proportional to the acousto-optic effective area of the fibres. A stronger acousto-optic interaction occurs when the light and sound are confined within a smaller area. Accordingly, depending on the core diameter, the gain will vary with respect to the different fibres if they have different core sizes. The graph includes the Brillouin gain of three types of hollow-core fibres, namely HC-PCF, HC-CAF, and HC-RAF. The acousto-optic effective area has been calculated theoretically (in section 6.2) with the aid of the finite element method (FEM) using COMSOL Multiphysics software. Since the PCF has the smallest core diameter ($D = 10\,\mu m$), the acousto-optic effective area is calculated to be $A_{ao} = 80\,\mu m^2$ for N_2 gas. It can be also observed that the Brillouin gain provided by the HC-CAF is higher than that of the HC-RAF. This ~2.75× higher gain is directly attributed to the ~2.66× smaller acousto-optic effective area A_{ao} of the HC-CAF ($A_{ao} = 340\,\mu m^2$) in comparison with that of the HC-RAF which is about $A_{ao} = 905$

Parameter	Symbol	Value
Molar Mass	M_m	44.01 g/mol
Shear Viscosity	η_s	15 µPa s
Bulk Viscosity	η_b	4 µPa s
Thermal Conductivity	κ_C	16.8×10^{-3} W/(m K)
Heat Capacity (constant pressure)	C_P	852.5 J/kg K
Heat Capacity (constant volume)	C_V	659 J/kg K
Derivative of C_P	dC_P/dT	0.99 J/kg K^2
Derivative of C_V	dC_V/dT	0.95 J/kg K^2
Second Virial Coefficient	B	-121.1×10^{-6} m^3/mol
Derivative of B	dB/dT	8.7×10^{-7} m^3/K mol
Second Derivative of B	d^2B/dT^2	-8×10^{-9} m^3/K^2 mol
Third Virial Coefficient	C	45.8×10^{-10} m^6/mol^2
Derivative of C	dC/dT	-17×10^{-12} m^6/K mol^2

Table 7.4 – Values used for the theoretical calculation using CO_2 gas at a constant temperature of $T = 298.15$ K [30, 166, 169].
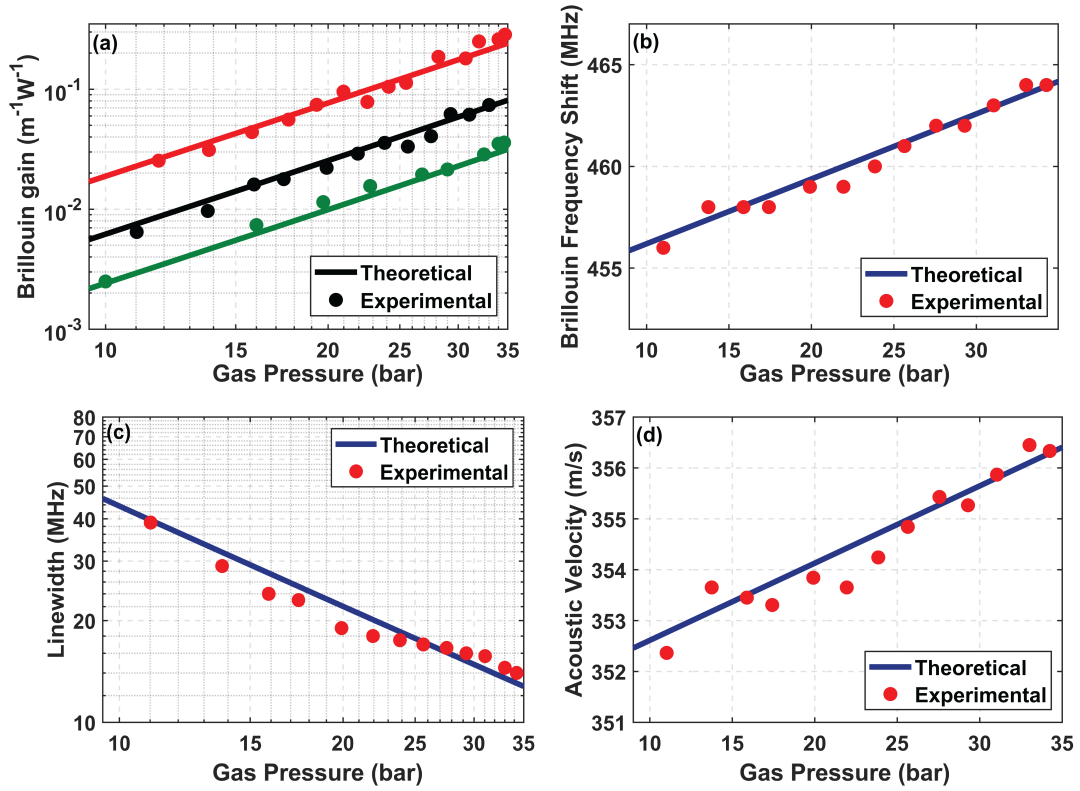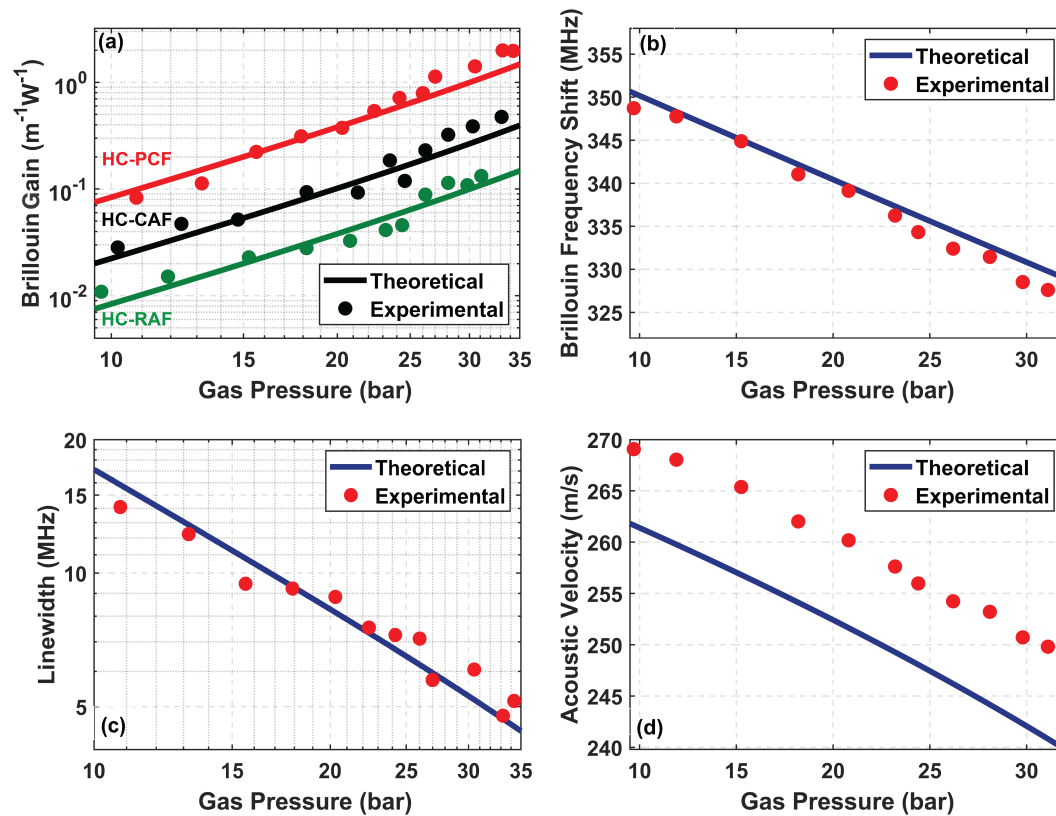

Figure 7.7 – Graphs showing different parameters as a function of the gas (CO_2) pressure: (a) Brillouin gain; (b) Brillouin frequency shift; (c) Brillouin linewidth; and (d) Acoustic velocity.

µm^2.

Carbon Dioxide (CO$_2$) gas

The results for the CO$_2$ gas are shown in Fig. 7.7. It can be observed from Fig. 7.7 (a) that the gains for the different fibres are larger for CO$_2$ when compared to N$_2$. This larger gain is a result of its massive molecular structure in comparison with N$_2$. Theoretically, heavier gases will exhibit higher Brillouin gains, which is caused by the molecules being denser as a result of them occupying a larger area in the medium. Gases like CO$_2$, however, have a rather significant drawback, namely the inevitable absorption lines in the infrared spectral region. This problem is not encountered when gases like N$_2$ with a simpler molecular structure are used. Fig. 7.7 (b) shows the Brillouin frequency shift in the case of CO$_2$ gas, and we can see that it is around 100 MHz smaller than that of N$_2$ gas. The Brillouin linewidth shown in Fig. 7.7 (c) for CO$_2$ gas is about 3× narrower than that of N$_2$ gas. This difference can be explained by the different thermodynamic quantities corresponding to each of the gases which are summarised in tables 7.3 and 7.4 for N$_2$ and CO$_2$ gases, respectively. More details about the acoustic velocity and the graph in Fig. 7.7 (d) will be discussed hereafter.

7.3.4 Discussion

Since the acoustic velocity plays a crucial role in the determination of the Brillouin gain, linewidth, and frequency shift, we would like to shed some light on it and understand how it varies with respect to the medium in which the sound is propagating. Unlike light which is a transverse wave that can propagate without having any medium, sound is a longitudinal wave that needs a medium to travel and moves with a series of compressions and rarefactions. When it comes to sound waves, there is essentially no real particle movement; particles simply vibrate to and fro around their mean position passing the sound energy from particle to particle while oscillating. Since the distance between molecules in solids is very small (solids are more dense compared to liquids and gases), they can collide very quickly, hence transfer energy much faster leading to significantly higher speeds of sound in solid media. This large density of molecules in solids makes the medium fairly rigid (i.e. less compressible), and this higher stiffness results in larger sound speeds. For a standard silica fibre at a wavelength of 1.55 µm, for example, the speed of sound is around 5972 m/s. This value is about an order of magnitude higher than the speed of sound in gases as we can see in figures 7.6 (d) and 7.7 (d) for N$_2$ and CO$_2$ gases, respectively. From these two figures, we can observe that the acoustic velocity of N$_2$ is about 100 m/s larger than that of CO$_2$. We also see that with respect to pressure, the acoustic velocity gets higher with higher gas pressure in the case of N$_2$ gas, whereas it gets lower with higher gas pressure in the case of CO$_2$ gas. This can be explained by the fact that massive molecules (e.g. CO$_2$ molecules) have more inertia to overcome, hence take longer time to respond. For large molecules which have more mass, given a particular volume, if the density becomes higher, molecules find it even more difficult to vibrate. Ergo, the kinetic energy becomes less, and in turn, heavier molecules will have slower sound speeds with respect to increased gas pressure. Lighter molecules, on the other hand, move faster (at a given constant temperature), and since the speed of sound (v_a) in gases is simply proportional

Table 7.5 – Acousto-optic effective area and Brillouin gain values obtained for the three different types of fibres used in the experiments for a pressure of 34.7 bar. The fibres used have the following core diameters: $D = 10\,\mu m$ for the bandgap PCF, $D = 22\,\mu m$ for the conjoined-tube ARF (CAF), $D = 35\,\mu m$ for the revolver ARF (RAF). The typical Brillouin gain for a standard single-mode fibre (SMF) with $D = 8\,\mu m$ is about $0.28\,m^{-1}W^{-1}$.

Parameter	Fibre type		
	PCF (10 µm)	CAF (22 µm)	RAF (35 µm)
Acousto-optic area (μm^2)	80	340	905
		N_2 gas	
Brillouin gain ($m^{-1}W^{-1}$)	0.285	0.079	0.029
		CO_2 gas	
Brillouin gain ($m^{-1}W^{-1}$)	1.44	0.383	0.145

to the speed (on average) of the molecules (v_{rms}) using the following expression: $v_a = \sqrt{\frac{\gamma_h}{3}}\,v_{\mathrm{rms}}$ with γ_h as the specific heat ratio, the sound accordingly travels faster. As per the last term of Eq. 2.68 and following the ideal gas approximation, we can see that the acoustic velocity v_a is a function of the molar mass M_m through an inverse square-root relationship, meaning that sound speeds are slower for heavier molecules. To summarise, at a constant temperature, the acoustic velocity is highly affected by two main contributions, namely the stiffness of the medium and the density (whether due to the size or the number of molecules).

As we can see in figures 7.6 and 7.7, there is a strong agreement between the theoretically-calculated and the experimentally-measured values. A noticeable disparity is, however, observed for the theoretical and experimental acoustic velocity values for CO_2 gas in Fig. 7.7 (d). In [13], the same dissimilarity was highlighted. One of the hypotheses in that work suggested that this difference may be due to the silica portion existent in the PCF fibre used in the experiments. Here, in our work we show that this disparity is still found despite the use of anti-resonant fibres with very low silica content. It means that the cause of this discrepancy is something related to a property of the gas itself and not the fibre used. One possible explanation for this disparity, and especially because it appears for CO_2 gas only and not for N_2 gas, is the fact the bulk viscosity for CO_2 gas and possibly also other heavy gases like SF_6 is frequency-dependent. The bulk viscosity is generally considered to be an elusive parameter and requires continuous investigations. It is associated with the relaxation of the internal degrees of freedom (i.e. rotational and vibrational) of gas molecules. Several works in the literature concluded that the value for the bulk viscosity of CO_2 gas varies significantly from low to high acoustic frequencies [170, 171]. It was shown in [172], that when using N_2 gas, vibrational modes are frozen at room temperature [173] for all cases whether measurements are conducted at lower or higher acoustic frequencies, and accordingly the same value of the bulk viscosity is yielded. This effect, however, is different when CO_2 gas is used. At room temperature at low acoustic frequencies, vibrational and rotational modes are both excited and take part in the energy exchange with translational modes during molecular collisions. In this case, the bulk viscosity values are very large. In the other scenario when dealing with

high acoustic frequencies, vibrational modes are frozen and the values of the bulk viscosity decrease dramatically. It is, therefore, necessary to carefully study this effect and take this frequency-dependence for CO_2 gas into consideration in the theoretical estimation. This result is quite intriguing and thus indicates that Brillouin scattering in gas-filled hollow-core optical fibres can be used as a potential tool to analyse gas properties such as the bulk viscosity under different experimental conditions.

In table 7.5, we summarise the Brillouin gain values obtained for the different hollow-core fibres with respect to the different gases used. The results are taken from measurements at a constant pressure of 34.7 bar and a constant temperature of 298.15 K. As discussed earlier, we can clearly see that the lower the acousto-optic effective area, the larger is the Brillouin gain. There is a trade-off, nonetheless, between the Brillouin gain achieved and the time it takes for the whole fibre to be filled with gas. We have seen in table 7.1 that smaller core-diameter fibres take much longer time to be entirely filled with the gas, especially of course for longer fibres. Therefore, the choice of fibre in this case highly depends on the application, and the decision of, whether one needs very high Brillouin gains with short fibres or rather moderate gains but longer fibres, has to be made.

Another interesting point worth elaborating is the choice of gas. As we see from table 7.5, results show that using CO_2 gas results in larger Brillouin gains, but due to their large size compared to N_2 gas, there is a trade-off, as CO_2 gas has absorption lines in the infrared spectral region which are not a concern when using N_2 gas. There is additionally one more crucial distinction when opting for either of these two gases. When using CO_2 gas, the pressure of the gas cannot be increased indefinitely because at pressures larger than 40 bar, CO_2 gas will change state and liquefy at room temperature. This problem is non-existent when N_2 gas is used, and the pressure can theoretically be increased with no limitation as long as the operating temperature does not reach the liquefaction temperature of N_2 gas which is between 63 and 77.2 K.

7.4 Distributed temperature measurement

Following the gain measurement, we proceed by conducting a distributed temperature measurement, but before delving deeper into the experiment, we shall first understand the temperature and strain sensitivities of the system.

7.4.1 Temperature and strain sensitivities

Temperature sensitivity

We have seen in section 2.3.6 that the acoustic velocity of a gas is temperature-dependent. When it comes to temperature change, there are two contributions which result in the change

of the acoustic velocity, and those can be described as follows:

$$\mathrm{d}v_a = \left(\frac{\partial v_a}{\partial T}\right)_P \mathrm{d}T + \left(\frac{\partial v_a}{\partial P}\right)_T \frac{\partial P}{\partial T}\mathrm{d}T. \tag{7.20}$$

where the first term on the right hand-side corresponds to the first contribution enumerated by 1, and the second term corresponds to the second contribution enumerated by 2 in the listing below:

1. The change in the acoustic velocity due to a temperature variation at constant pressure, $\left(\frac{\partial v_a}{\partial T}\right)_P$, and this contribution is determined using the virial coefficients.
2. The change in the acoustic velocity due to a pressure variation that propagates through the whole fibre, and this contribution is an unintentional inevitable consequence of a change in the average temperature along the fibre.

As can be intuitively realised, the second contribution is not really desired, and this is simply because it represents a non-local effect. This means that unrelated positions far away from the hot spot may be unintentionally affected, and this would cause a bias in the temperature measurement. It is, therefore, necessary to estimate the error which this bias results in. If we assume that the increase in the pressure P due to a temperature change follows the ideal gas law, and given that the pressure is the same everywhere, the local density in the fibre is written as follows:

$$\rho = \frac{PM_m}{RT(z)} \tag{7.21}$$

where M_m is the molar mass, R is the gas constant, and $T(z)$ is the temperature profile along the fibre distance z. Since the total mass M of the gas is conserved, we have the following expression:

$$\int_0^L \rho\mathrm{d}z = \frac{M}{A} \tag{7.22}$$

with A as the hollow area of the fibre. If we assume having a hot spot of length l_h at a constant temperature of $T_0 + \Delta T$ while the remaining length of the fibre is at a constant temperature of T_0, then by substituting Eq. 7.21 into Eq. 7.22 and equating the integral, we yield the equation below:

$$P = P_0 \frac{L(T_0 + \Delta T)}{T_0 L + \Delta T(L - l_h)} \tag{7.23}$$

We then differentiate Eq. 7.23 with respect to ΔT and get following expression:

$$\frac{\partial P}{\partial(\Delta T)} = P_0 \frac{l_h L T_0}{(T_0 L + \Delta T(L - l_h))^2} \approx \frac{P_0 l_h}{T_0 L} \tag{7.24}$$

For N_2 at different pressures, we found a change in the Brillouin frequency shift of 0.32 MHz/bar (see Fig. 7.6 (b). Accordingly, for $P_0 = 35$ bar, $T_0 = 298.15$ K, $L = 50$ m, $l_h = 1$ m, we obtain a Brillouin frequency shift bias of 0.75 kHz/K, which can be considered to be an acceptable

value, as the desired contribution, from the first term of Eq. 7.20, is in the order of MHz as will be presented later on in this chapter. However, in a different case, where $l_h = 49$ m, the remaining 1 m of the fibre will experience a bias in the Brillouin frequency shift of 36.81 kHz/K.

For CO_2 at different pressures, the change in the Brillouin frequency shift of -1.1 MHz/bar (see Fig. 7.7 (b). In turn, for $P_0 = 35$ bar, $T_0 = 298.15$ K, $L = 50$ m, $l_h = 1$ m, we obtain a Brillouin frequency shift bias of -2.58 kHz/K. When $l_h = 49$ m, the bias in the Brillouin frequency shift is -126.55 kHz/K, which is quite significant and may lead to a large error in the temperature measurement.

Strain sensitivity

When strain is applied along a gas-filled hollow-core fibre, the gas automatically adapts to the available volume and has accordingly negligible sensitivity to the strain of the surrounding structure. Since the Brillouin scattering interaction only occurs within the gas medium, the whole system can thus be considered to be almost completely strain-insensitive. More intuitively, if we assume a longitudinal hypothetical strain that is applied on the fibre, the following negligible effects are the consequences:

- The effective refractive index of the optical mode will be modified due to the Poisson effect causing the distortion of the cladding structure as well as the photo-elastic effect leading to the change of the refractive index of the silica capillaries.

- The silica capillaries will shrink in size, whereas the fibre length will increase, leading to a change in the volume available for the gas along the fibre.

The quantification of these effects for a longitudinal strain ϵ applied on a 3-D slice of a HC-PCF has been presented in [13] using a finite element method simulation, and the deformations were analysed to estimate the corresponding change in the effective refractive index n_{eff}. To calculate the local change in the BFS due to a longitudinal strain along an optical fibre when it subjected to a longitudinal strain ϵ, the following expression is utilised:

$$\frac{\mathrm{d}\nu_B}{\mathrm{d}\epsilon} = \frac{\nu_B}{n_{\text{eff}}}\frac{\partial n_{\text{eff}}}{\partial \epsilon} + \frac{\nu_B}{\nu_a}\frac{\partial \nu_a}{\partial \epsilon} \tag{7.25}$$

The first term in Eq. 7.25 can be straightforwardly estimated given the change in the effective refractive index with respect to the strain applied is acquired from the simulation. In this case, let us assume an applied longitudinal strain of 2% on a 35-bar N_2-filled hollow-core fibre whose BFS is $\nu_B = 465$ MHz, and we take the same value given in [13] for $\frac{\partial n_{\text{eff}}}{\partial \epsilon} = -1.7 \times 10^{-3}$, the term will be calculated to yield:

$$\frac{\nu_B}{n_{\text{eff}}}\frac{\partial n_{\text{eff}}}{\partial \epsilon} = -791 \text{ kHz}/\epsilon \times 2\% = -15.8 \text{ kHz} \tag{7.26}$$

This value is obtained for one particular cladding structure, namely photonic-crystals. However, the value will probably differ for other structures, and the strain sensitivity with respect
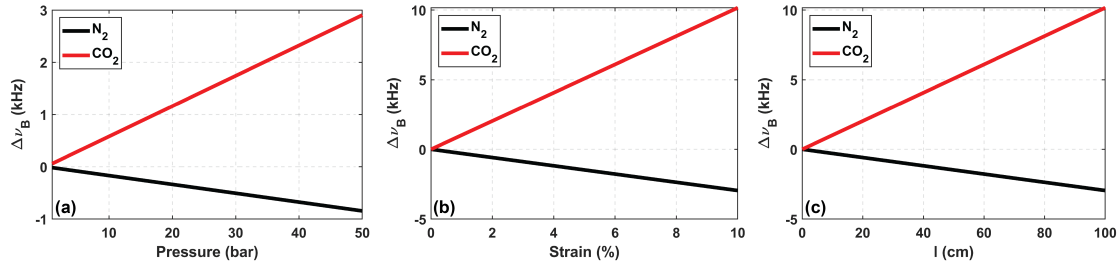
Figure 7.8 – Graphs showing the change in the BFS with respect due different parameters for two gases (N_2 and CO_2); (a) varied pressure at a constant applied strain of 2% and a constant l of 20 cm; (b) varied applied strain at a constant pressure of 35 bar and a constant l of 20 cm; and (c) varied l at a constant pressure of 35 bar and a constant applied strain of 2%.

to the refractive index change may be even smaller.

The second term deals with the change in the acoustic velocity. Since in this situation, the temperature is constant and, the only source of change in the acoustic velocity will result from a variation in the gas pressure. Accordingly, we write the following expression to estimate the change in gas pressure occurring due to the applied strain:

$$\frac{\Delta P}{P} = -\frac{\Delta V}{V} = -\epsilon_z \left(\frac{l}{L}\right)\left(1 - 2\nu_p\right) \tag{7.27}$$

where $\frac{\Delta P}{P}$ and $\frac{\Delta V}{V}$ represent the changes in pressure and volume with respect to their original values, respectively. It should be mentioned that the opposite signs of $\frac{\Delta P}{P}$ and $\frac{\Delta V}{V}$ indicate that a decrease in the volume is induced by an increase in the pressure and vice versa. $\epsilon_z = \frac{\delta l}{L}$ is the applied longitudinal strain with L as the total length of the fibre, and δl as the length of the elongation resulting from the applied strain. l is the portion of the fibre over which the strain is applied, and ν_p is the Poisson's ratio which is typically equal to 0.17 for silica glass. Accordingly, if we consider a hollow-core fibre of 50 m length filled with 35-bar N_2 gas, and subject a portion of it, around l =20 cm, by 2% strain ($\delta l = \epsilon_z L = 1$ m), the total pressure change would be calculated to be: $\Delta P = -1.85$ mbar. As the pressure-dependent Brillouin frequency has been found to be of ~ 0.32 MHz/bar for N_2 (see Fig. 7.6 (b)), the total BFS change due to the gas pressure variation would be $\Delta P \times 0.32$ MHz/bar $= -0.59$ kHz. Finally, the total strain sensitivity in this case will be given as: $\frac{d\nu_B}{d\epsilon} = -15.8$ kHz $- 0.59$ kHz $= -16.39$ kHz. If we utilise CO_2 instead of N_2 in the previous example, the strain sensitivity will be different, as in this case the sensitivity of the BFS with respect to change of pressure is ~-1.1 MHz (as seen in Fig. 7.7 b). Consequently, the total BFS change due to the gas pressure variation would be $\Delta P \times -1.1$ MHz/bar $= 2.03$ kHz, and finally the total strain sensitivity will become: $\frac{d\nu_B}{d\epsilon} = -15.8$ kHz $+2.03$ kHz $= -13.77$ kHz. As can be inferred, the values of the strain sensitivities are relatively small and can be considered almost negligible, given that the temperature sensitivity, as will be shown later, is in the order of MHz. In Fig. 7.8, we can see a compilation of graphs showing the change in the BFS as a function of varied pressure at a constant applied strain of 2% and a constant l of 20 cm (Fig. 7.8 (a)), varied applied strain at a constant pressure

of 35 bar and a constant *l* of 20 cm (Fig. 7.8 (b)); and varied *l* at a constant pressure of 35 bar and a constant applied strain of 2% (Fig. 7.8 (c)). The figures show the behaviour of the two different gases at different conditions. By choosing the proper gas and gas pressure, it is possible to conduct temperature measurements which are partially or even completely strain-insensitive as demonstrated experimentally in the study by *Yang et. al* [48] using a hollow-core bandgap photonic-crystal fibre. The same concept applies to anti-resonant fibres as well since they contain even less silica content than hollow-core PCFs, meaning that the sensitivity may be mostly dominated by the contribution of the gas only. This means that the cross-sensitivity between strain and temperature, which has been a long-time problem for the optical fibre sensing community, can be mitigated using this interesting platform based on the utilisation of hollow-core fibres.

7.4.2 Experimental setup

The temperature measurement is performed using Brillouin optical correlation-domain (also referred to as coherence-domain) reflectometry (BOCDR). The working principle is described in detail in [50] and [51]. It is a technique which can reach high spatial resolutions and only requires a single access to the fibre under test.

As shown in Fig. 7.9, the light from the DFB laser is split into two branches by means of a 90/10 coupler, where 10% of the light is amplified by an Erbium-doped fibre amplifier (EDFA) followed by a polarisation controller (PC). A circulator is then used so that the light propagates from port 1 to port 2 into the fibre under test (21 m long) with a hot spot (2 m), gets backreflected and passes through port 3 where it reaches a 50/50 coupler. The light in the 90% branch passes through a 1.6 km delay fibre, a PC and is combined with the spontaneous Brillouin backscattering using the 50/50 coupler to beat at a 1 GHz photo-detector (PD). The light is frequency modulated by tuning the current of the laser and the heterodyne beating at the PD results in a correlation peak when the scattering light is in-phase with the reference
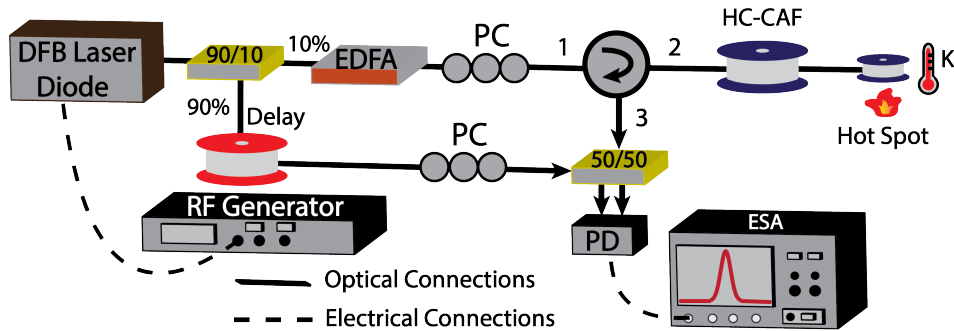

Figure 7.9 – BOCDR experimental setup used for the temperature measurement: DFB: Distributed feedback laser, EDFA: Erbium-doped fibre amplifier, PC: Polarisation controller, ESA: Electrical spectrum analyser.

light.When the two beating signals are in phase, the BGS can be measured, whereas when they are out-of-phase, there will be no correlation peak and the BGS cannot be measured. Hence, the position of the correlation peak may travel along the fibre when the laser modulation frequency is altered. The BGS is then acquired by an electrical spectrum analyser (ESA) for further analysis. Unlike in the experimental setup presented in [50], in our setup presented in Fig. 7.9, only one EDFA was required and no optical filtering was needed since no Rayleigh scattering was observed during the experiment. Additionally, since the Brillouin frequency shift (BFS) is in the MHz range for the gas, no large bandwidth PD was necessary.

The light source used is a distributed feedback laser with a linewidth measured to be around 3 MHz at a centre frequency at 1550 nm whose frequency is directly modulated using a sinusoid generated by a radio-frequency (RF) generator. There are two fundamental parameters of a BOCDR system which determine the overall performance of the sensor, and they are governed by the two expressions mentioned earlier in section 2.4.2 which we repeat here for convenience:

$$D_m = \frac{v_{\mathrm{group}}}{2f_m} \qquad (7.28) \qquad R_{\mathrm{sp}} = \frac{v_{\mathrm{group}}\Delta v_B}{2\pi f_m \Delta f} \qquad (7.29)$$

where v_{group} is the group velocity. We can see from equations 7.28 and 7.29 that the measurement distance and the spatial resolution are functions of the modulation frequency and the modulation amplitude. The modulation frequency (f_m) is chosen to be 5.99 MHz and the modulation amplitude (Δf) is selected as 200 MHz which corresponds to 70 mV on the RF generator, resulting in a spatial resolution of ~55 cm for a measurement distance that covered the full 21 meters of our fibre under test. It should be also noted that the modulation amplitude is also limited by the BFS, and it has to be chosen in such a way that it is smaller than half of the BFS. This is because if it is larger than this proper value, the BGS might buried inside reflections from the coupling end faces. Since the BFS in our case is around 465 MHz, a good enough margin would be around 200 MHz which is our choice.

To achieve that the correlation peak is moving along the fibre (21 m), the modulation frequency was tuned within a range of 35 kHz from 5.971 MHz to 6.006 MHz. For the temperature measurement, we only tuned within a range of 16 kHz (corresponding to 10 m of the fibre) from 5.985 MHz to 6.001 MHz which is a range around the hot spot. At the hot spot, we placed ~2 m of the fibre on a hot plate and a thermocouple was used to measure the temperature which was varied over a range of 12 K. The pressure in the gas cell during the temperature measurements was chosen to be around 35 bar.

7.4.3 Temperature measurement results

The results of the temperature measurement are presented in Fig. 7.10. The longitudinal distribution of the Brillouin frequency shift with respect to a distance of 10 m along the HC-CAF is illustrated for varying temperatures. From the figure, we can clearly see that the hot
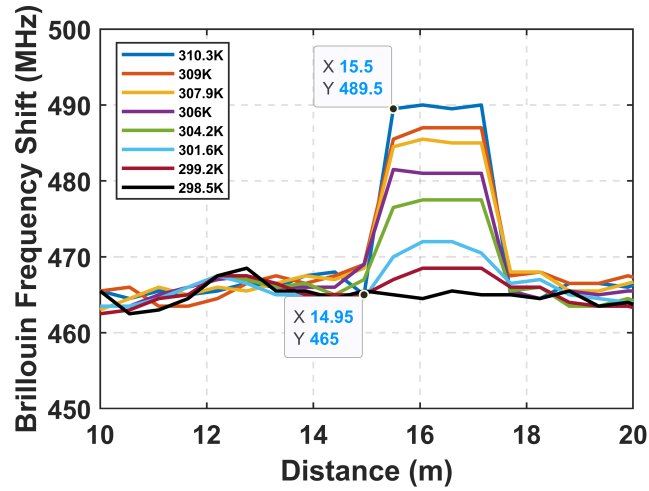
Figure 7.10 – Graph showing the Brillouin frequency shift at different temperatures as a function of distance.
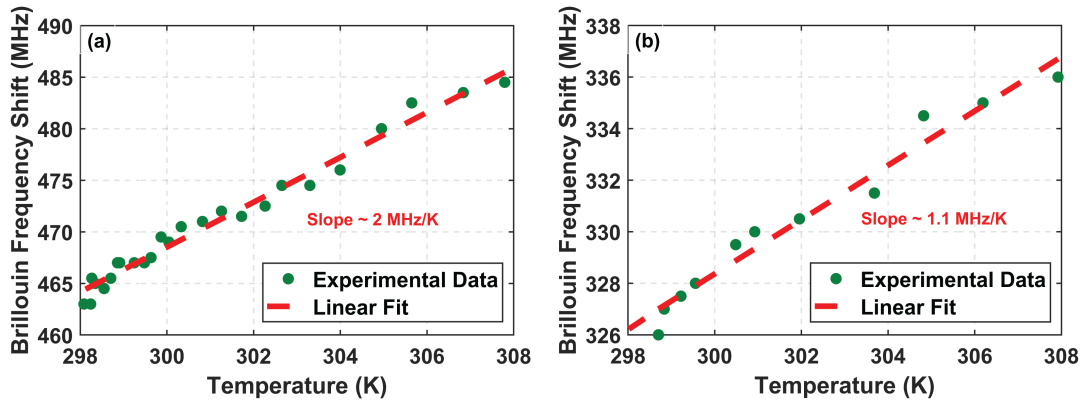
Figure 7.11 – Graphs showing gas sensitivities: (a) Nitrogen gas; (b) Carbon Dioxide gas.

spot is about 2 m in length. The spatial resolution is indicated as the length between the two points marked on the graph which is calculated as 55 cm. Concerning the slightly different positions causing more abrupt transitions; this simply is a consequence of the uncertainty in the determination of the central frequency of the Brillouin gain spectra in the presence of noise. Already from this graph we can infer the sensitivity and can see that it is around 2 MHz/K. This sensitivity is obtained for the case of utilising N_2 gas as the scattering medium. The sensitivity was measured also when CO_2 gas was used as the medium, and it was around 1.1 MHz/K. The graphs showing the sensitivities for the two gases are depicted in Fig. 7.11 where the BFS is shown as a function of the different temperatures. The experimental data is fitted linearly with a correlation factor of 0.99. It is worth noting that the sensitivity of the gases to temperature changes remains mostly the same at different applied pressures as long as the gas maintains its state of matter. In the case of gases like CO_2, distributed sensing can only be conducted within specific ranges of pressures at which the gas is not close to liquefaction.

115

Measurement frequency shift uncertainty

A rigorous model for the measurement uncertainty for Brillouin-based sensors has been presented in [89], and the expression governing the uncertainty is given by:

$$\sigma_B = \frac{1}{\text{SNR}} \sqrt{\frac{3}{4} \delta_B \Delta v_B} \tag{7.30}$$

where δ_B is the frequency sampling step, and Δv_B is the Brillouin linewidth. In the current experimental conditions, the SNR was calculated using Eq. 7.13 and was estimated to be around 3 dB. δ_B and Δv_B were obtained from the Brillouin gain spectra in the case of N_2 gas and are given as 0.5 MHz and 13 MHz, respectively. For CO_2 gas, Δv_B is given as 3 MHz. Accordingly, the frequency shift uncertainty is computed to be around 1.1 MHz for N_2 gas and around 0.51 MHz for CO_2 gas. Using the different sensitivities of N_2 and CO_2 gases, the temperature uncertainties yielded are 0.54 K and 0.47 K, respectively.

7.4.4   Discussion

An interesting result obtained from the temperature measurement is the fact that the temperature sensitivity of the two gases used in the experiments varied with respect to the gas. This variation may be linked to the different masses of the gases. In fact, N_2 gas is about ~1.6× lighter than CO_2 gas, and the sensitivity obtained for N_2 gas is about ~1.8× larger than that of CO_2 gas. This indicates that even lighter gases like methane for instance may show even higher sensitivities. The sensitivity of the gas is again linked to the acoustic velocity which can be considered the key parameter controlling the sensitivities of temperature and strain in a Brillouin-based sensor based on gas-filled HCFs. Using Eq. 7.24, we can estimate the bias that may be contributed due to pressure change in the gas medium as a result of the sudden temperature change at the hot spot, and the calculation indicates that the sensor bias in the case of N_2 gas is about 3.58 kHz/K and for CO_2 it is about -12.29 kHz/K which can be considered to be relatively negligible in both cases with respect to the overall temperature sensitivity which is in the order of MHz/K.

Since our experiments contained a comparison between N_2 and CO_2 gases, we kept the pressure well below the state at which CO_2 gas liquefies. Accordingly, the spatial resolution and the temperature uncertainty were limited by the linewidth of the Brillouin gain spectrum. In the case of N_2 gas, however, there is no limitation in terms of how much pressure can be applied, and accordingly the linewidth can be further reduced with the increase of pressure, and in turn also the spatial resolution as well as the temperature uncertainty of the measurement. The same applies to other lighter gas like Methane as an example. Even though such gases exhibit lower Brillouin gains, they can potentially have very high temperature sensitivities compared to heavier gases which exhibit larger Brillouin gains. The smaller gains can anyway be also compensated by applying higher pressure, since these gases show no limitations in terms of state changes.

As we can clearly understand from these results, this platform is very agile and can be adapted to different types of gases. It can be applied to various applications, and depending on the type of study, the suitable gas, gas pressure, gas temperature, etc. can be chosen.

8 Conclusions and perspectives

8.1 Thesis main contributions

In this thesis, we highlight the great capabilities of some novel speciality fibres that have the potential to contribute to technological advancements in the field of distributed optical fibre sensing. We, accordingly, demonstrate the use of several interrogation techniques to investigate different scattering mechanisms and scattering media. The thesis is, therefore, split into two groups of chapters depending on the scattering mechanisms and the scattering media used.

Reflection-enhanced optical fibre sensors

The first group of chapters presents a comprehensive study on utilising reflection-enhanced optical fibres (REF) based on fibre Bragg gratings to generate a larger directional backreflection. Fibre Bragg gratings are essentially very similar to the inevitable density fluctuations, also referred to as Rayleigh scattering centres, which are generated in a standard silica single-mode fibre (SMF) during the fibre drawing process. The main difference is that ultra-weak fibre Bragg gratings result in a directional reflection, and accordingly achieve a significant enhancement of the backreflected signal without an increased loss of the same proportion.

The backreflected signal of a grating is measured in the same way as that of a back-scattered Rayleigh signal. In turn, we utilised one of the currently emerging techniques which offers extremely high sensitivity to external quantities, namely phase-sensitive optical time-domain reflectometry (φ-OTDR). We performed a comparative analysis between the REF and an SMF, and we formulated a theoretical expression that relates the most fundamental parameters of Rayleigh-based systems when using cross-correlation for the frequency shift estimation, which are the frequency shift uncertainty of the measurement along with the signal-to-noise ratio (SNR) and the spatial resolution. The expression was validated experimentally, and we clearly demonstrated the inverse relationship between the measurement frequency shift uncertainty and the SNR, as well as the inverse square dependence of the measurement frequency shift

uncertainty on the spatial resolution. This result can indeed be considered to establish a figure-of-merit for Rayleigh-based systems which rely on the cross-correlation operation for the estimation of the frequency shift.

A temperature measurement was finally conducted to point out the effect of the increased SNR of the REF with respect to the temperature uncertainty of the measurement. We showed that despite the modifications of the core of this special fibre, the sensitivity is the same as that of a standard SMF. However, the temperature uncertainty in the measurement is 6× smaller than that of a standard SMF which is a direct consequence of the 6× enhanced SNR.

We also tackled the problem of enhanced-signal associated noises, and how they can be detrimental if not treated carefully. To that effect, we provided some guidelines on how to employ such reflection-enhanced fibres to exploit their potential to maximum effect. We highlighted that input powers, the number of time-averaged traces, and the measurement time may have a severe impact on the performance of REFs if not chosen as per the guidelines presented earlier. Even though such a fibre shows an 8 dB enhancement over the Rayleigh scattering level, this enhancement may not necessarily translate into a full SNR enhancement under improper experimental conditions, which reduces the benefit of such type of fibres. However, as we indicated in our work, using these fibres with careful adjustment of the experimental conditions will yield measurements with much lower temperature uncertainties (0.5 mK) with respect to temperature uncertainties provided by standard SMFs (3 mK).

Gas-filled hollow-core optical fibre sensors

In the second group of chapters, we switched the focus to gas-filled hollow-core optical fibres (HCFs). One particular kind of HCFs, namely anti-resonant HCFs, is rapidly emerging owing to their significantly lower propagation loss as well as their quasi-zero dispersion and nonlinearities. Their benefits extend over a plethora of applications which are not only limited to data transmission and communications. Such fibres are capable of providing a suitable platform for light-matter interaction especially when filled with a fluid, for example. They have a higher optical power damage threshold when compared to conventional silica fibres and can provide long interaction lengths which enable efficient wave coupling.

We, accordingly, obtained several hollow-core fibres through purchases and collaborations, and demonstrated for the first time a Brillouin gain measurement in gas-filled anti-resonant HCFs. The Brillouin gain spectrum was measured using a simple Brillouin reflectometer, and the spectra were calibrated by means of an additional setup. We clearly highlighted the square dependence of the Brillouin gain with respect to the gas pressure and corroborated the theory by experimental results using gas-filled anti-resonant HCFs. Additionally, we performed a finite element method simulation from which we obtained the acousto-optic effective overlap areas (A_{ao}) for all the fibres utilised in the experiments, and showed experimentally how the Brillouin gain is inversely related to A_{ao}.

Basing on already-established theory, we provided some insights on the filling times of gas with respect to the different fibre core areas, and pointed out that smaller cores require significantly longer gas filling times. Due to the flexibility of our gas cell built to perform all the experiments, we were able to change the gases in the cell, and accordingly presented results for two different gases, namely N_2 gas and CO_2 gas. The experiments with the different gases pointed out their dissimilar characteristics in terms of Brillouin gain and linewidth as well as the acoustic velocity and accordingly the Brillouin frequency shift. We elaborated on how the choice of gas is merely dependent on the users' applications and explained the benefits and limitations of the two gases used.

The final experiment was conducted to demonstrate the great potential of anti-resonant HCFs to be utilised for fully-distributed temperature sensing. A Brillouin optical correlation-domain reflectometer is used as the experimental setup with which a sub-meter spatial resolution is achieved for a sensing length of 21 m. We showed that with the choice of gas, we can alter the sensitivity of the system, and presented a 2 MHz/K sensitivity for N_2 gas, whereas for CO_2, the sensitivity is 1.1 MHz/K. Temperature uncertainties of 0.54 K and 0.97 K were yielded for N_2 gas and CO_2 gas, respectively.

8.2 Future work and perspectives

Now that we have summarised the main results achieved in this thesis, it is important to point out how the work can be further extended and hopefully lead to more fruitful works. Since throughout the thesis we have divided the work according to the scattering mechanisms and media, we will proceed in the same manner and indicate the future work of each topic separately. In the end, we will conclude with final overall perspectives.

Reflection-enhanced optical fibre sensors

Reflection-enhanced fibres will presumably receive increased attention for Rayleigh-based distributed sensing in the near future owing to their relatively low propagation loss and the directional enhanced backreflection they provide. With the enhanced SNR provided by the REFs along with the theoretical model presented in this thesis, the frequency shift uncertainty of any measurement relying on cross-correlation for the frequency shift determination can be easily predicted just by knowing the SNR and the spatial resolution of the system. This, in turn, will save a lot of time spent performing and repeating experiments, and will aid in the optimisation of the system in terms of the number of time-averaged traces, the scanning range, the scanning step, along with others.

Despite the advantages provided by the theoretical model, it ought to be remarked that it should still be adjusted for measurement cases where large errors are present. Large errors can be absolutely detrimental to the measurement and the current model may not provide accurate results in that case. It can also be extended to a model which uses the least-mean-square

operation instead of the cross-correlation operation for the frequency shift determination. The least-mean-square approach has proven its capabilities to drastically minimise the probability of large errors, and establishing a theoretical model based on it can probably be more comprehensive and may be valid in all situations.

Even though we have been quite focused on developing theoretical models to predict the behaviour of the experiment, there is still an ongoing issue that cannot really be solved by the models. It is the fact that the current experimental measurements are relative to reference measurements and are not absolute. Absolute measurements are desired in many applications which need the information to be quickly available and where a real-time measurement is a requirement. In this case, one may think of machine learning as a tool to address this matter. Each manufactured fibre can be characterised by a neural network tailored specifically to that particular fibre. The characterisation can be initially achieved by training on a large data set to develop a well-performing neural network. Then, transfer learning can be applied to adapt the model to other fibres; in this case much smaller data sets would be needed. End users can then benefit from readily-characterised fibres using machine learning and can accordingly conduct reference-free measurements which will save them a significant amount of time. While several works in the literature have already tackled this problem, this field is still under investigation and development and further improvement is undoubtedly needed. Achieving absolute distributed sensing and using reflection-enhanced fibres will be very beneficial to a myriad of fields such as distributed acoustic sensing which is currently heavily employed for the early detection of seismic activities.

Gas-filled hollow-core optical fibre sensors

The technology based on gas-filled hollow-core optical fibres is very promising and has great potential to be integrated in a wide range of applications. We predict that the work in this field will advance pretty rapidly especially with the continuous effort in the fabrication of hollow-core fibres to reach a propagation loss comparable or even smaller than silica fibres. In our work, we filled the hollow-core fibres with two gases, namely N_2 gas (light gas) and CO_2 gas (heavy gas). It will also be interesting to fill the fibres with other types of gases, even mixtures, and observe their sensitivities for distributed temperature measurements. We predict that significantly high sensitivities may be reached if the proper gas is utilised. Other than gases, there are liquids, plasma, or other potential fillings that may be interesting to be investigated and explored further.

An interesting direction where improvement is necessary is the preparation of the gas cell. The whole cell-making process can definitely be properly automated to yield the best performances of the platform. Making the cell air-tight to make sure that no leakage occurs is relatively tricky, and by automatising the fabrication process, the cell can be packaged and made into a product to facilitate its use for research and potentially maybe industrial purposes.

Just recently, a work by our group presented the measurement of an intense Brillouin gain

from the evanescent field at the surrounding of nano-fibre based on the same technology used in this thesis. The nano-fibre was placed in a pressurised CO_2-filled gas cell, which indicates that this platform can be extended to study other types of media surrounding the nano-fibre. Different liquids and solvents can be characterised and their viscoelastic properties can be quantified using this technology which, with some changes, may also be potentially applied to applications in spectroscopy and microscopy.

Our work on hollow-core fibres has been solely oriented towards the measurement of Brillouin scattering, as it is the most prominent scattering process at high gas densities. Another exciting idea would be the investigation of Rayleigh scattering at very low pressures with different types of gases, more specifically heavy gases, whose mean-free path is relatively large. It has been already demonstrated in the literature that Rayleigh scattering in hollow-core anti-resonant fibres filled with air at atmospheric pressure is 40 dB lower than that of silica fibres. In this case, however, the gas is in the hydrodynamic regime because already at atmospheric pressure the gas exhibits high density and the mean-free path between the molecules may be really small. Therefore, for this study, the pressure should be in the millibar range, i.e. molecular regime of the gas. This though may be a bit challenging due to a number of concerns like the vacuum requirements, the sensitivity of the interrogation technique and the end-facet reflections. The facet reflections may be highly suppressed if the fibres are spliced with the SMF pigtails rather than relying on butt-coupling. As for hollow-core fibres which have a larger silica content like hollow-core bandgap photonic-crystal fibre, with Rayleigh scattering, even at higher pressures, we can measure the time it takes the gas to stabilise inside the fibre, which is not so easy to know if the gas does not have absorption lines as an indication. CO_2 gas, for example, has absorption lines within the wavelength range of operation in our experiments, but for N_2 gas, there are not. This means that one needs to roughly estimate the time it takes for the gas to entirely stabilise in the fibre, which can be potentially determined using Rayleigh scattering traces.

Overall perspectives

It is quite fascinating to observe the great capabilities of the novel optical fibres employed in this thesis. In the field of distributed fibre sensing, there are various degrees of freedom which do not only include the choice of fibre, but also other parameters such as the scattering medium, the scattering mechanism, and the sensing technique. To make a well-informed decision between the different parameters, one must thoroughly explore each of their strengths and limitations. Our studies highlight how a combination of these parameters can be optimally chosen for application-specific solutions.

The most prominent natural scattering process occurring in silica fibres is Rayleigh scattering. Sensors based on Rayleigh scattering are known to be several orders of magnitude more sensitive than their counterparts. Before conducting our experiments, it was unclear whether the reflection-enhanced fibre used exhibits the same sensitivity as a standard single-mode

fibre, which we later confirmed to be the same. Even though reflection-enhanced fibres require an additional fabrication step, they show very similar characteristics with respect to standard single-mode fibres, but can offer additional considerable advantages. Based on our results, sensors based on reflection-enhanced fibres —when exploited efficiently —can measure ultra-small changes of external quantities. Such sensors may be very valuable for applications which require the detection of minute temperature changes like high-voltage power lines to prevent any overheating of the cables. Additionally, they can be very beneficial for the detection of natural hazards as early warning tools.

Despite the fact that solid-core fibres have been and are still heavily used in a plethora of applications, hollow-core fibres are rapidly paving their way as promising candidates for telecommunications applications as well as in the fields of lasing, sensing, along with others. Within the category of hollow-core fibres, one has an even wider choice of fibres as a result of the continuous quest for the fibres with the lowest possible propagation loss. The guiding mechanism of photonic crystal fibres makes the overlap the optical field with the silica glass relatively large ($\sim$0.1-1%), unlike in the case of anti-resonant HCFs ($\sim$0.01%). Accordingly, Rayleigh and surface scatterings in anti-resonant fibres are extremely small and may be difficult to be detected with conventional interrogation techniques.

On the one hand, anti-resonant fibres seem to be more promising for telecommunications applications, as they have already shown exceptionally low propagation loss. On the other hand, they might not necessarily be the preferred option if they are to be filled with any substance (such as pressurised air) to perform studies on nonlinearity, lasing, and sensing using inelastic scattering processes like Brillouin and Raman scatterings. This is because of their large core dimensions which will result in smaller gains. In our experiments, we decided to go for the measurement of Brillouin scattering in gas-filled hollow-core fibres because Brillouin scattering is the most prominent scattering process in gases of rather higher density (1 atm of gas pressure).

Anti-resonant fibres have relatively large core diameters, and in the case of Brillouin scattering for instance, one yields lower Brillouin gains as a pure consequence of the larger acousto-optic overlap effective area due to the large core effective area. Hollow-core photonic crystal fibres in this case may be more desired, as their use would result in significantly large Brillouin gains. Yet again, since anti-resonant fibres have lower silica content than photonic-crystal fibres, they may be even less sensitive to strain changes, which is crucial to eliminate the cross-sensitivity between strain and temperature occurring in silica fibres. If anti-resonant fibres are designed and fabricated with very small core dimensions while still exhibiting low propagation loss and containing low silica content, they would be considered to be very promising candidates. However, our results also showed that the smaller the core dimensions are, the longer time it takes for the hollow-core fibres to be filled with gas. Based on our studies, the most preferred and optimal option would be an anti-resonant fibre with core dimensions which are not too small or too large as in the case of the fibre that we used in our distributed temperature measurement demonstration.

In all of our experiments, we opted for experimental setups which only require a single-ended access to the fibres, so that any possible faults in the middle of the fibre do not interrupt the whole measurement. Before conducting the measurement of Brillouin scattering for the first time in an anti-resonant fibre, it was unclear to determine at which gas pressure it will be possible to detect and observe a Brillouin gain spectrum. Our results indicated that already at 6 bar of pressure in a 2 m long anti-resonant with a large core diameter, we were able to acquire a clear Brillouin gain spectrum, and with a smaller core the detection will be at an even lower pressure. This indicates, that for such studies of nonlinearity and sensing, there is no real need for sophisticated setups which require access to the two ends of the fibres under test. In other applications, however, like Brillouin gas lasing for example, the need for the two ends of the fibres under consideration is justified because they are required to create the lasing cavity.

An interesting quality of hollow-core fibres when compared to solid-core fibres is their flexibility in terms of the scattering medium. The variability of the medium enables an additional degree of freedom which is the alteration of the scattering medium. We have seen in our study that due to the different properties of gases, a sensor may exhibit different characteristics according to the gas used. This advantage over solid-core fibres may be very valuable for specific types of applications where comparative studies of different substances are carried out under the same exact conditions by making sure that the environment of the substance remains the same throughout the experiments.

The presented studies in this thesis provide a unique perspective on utilising the simplicity in existing tools with precise adjustments and exploiting them to maximum effect to reach outstanding performances. Our work helps the scientific community by elucidating the nature of such speciality fibres to be employed for more advanced distributed optical fibre sensing applications and to contribute to the advancement and progress of other fields as well.

A Measurement frequency shift uncertainty derivation

Similar to Radar applications, a phase-sensitive optical time-domain reflectometry (φ-OTDR) measurement can be considered as a time-delay estimation (TDE) problem. In both fields "Radar" and "Distributed Optical Fibre Sensing (DOFS)", the observer is interested to extract the delays/shifts in the signals that get backreflected and detected by the receiver. The concept is basically the same except for the fact that in TDE we directly use the time-domain traces to extract the delay between the signals, but in the case of DOFS, the signals used for the shift extraction are artificially-constructed and are not the direct time-domain traces. In this case, it is not the time delay that is being retrieved, but it is actually the frequency shift between the signals. This shift then indicates the amount of perturbation that the fibre is subjected to.

To calculate this delay/shift, a measurement is performed consecutively, and successive signals will be acquired by the receiver and can be compared to a reference signal (with no delay/shift) by means of different statistical estimators such as "cross-correlation".

The challenge encountered when dealing with the information received at the detectors is the fact that the signals are mixed with some unwanted noise that makes it difficult to extract the maximum wanted information from these signals. For instance, if a signal experiences a specific delay/shift τ_0, and is captured by the receiver, an inevitable unwanted random noise n will accompany the wanted signal. This means that the true value of τ is impossible to attain, and will result in the acquisition of some signal y, which is the mixture of both the wanted information and the noise n. Since the aim of the observer is to gain the most information about the delay/shift τ from y despite the presence of n, this mathematical problem can be modelled with the use of probability theory. The theory of probability distributions is usually a helpful approach to be utilised when random effects which can be measured numerically, such as n in this case, take place.

The following derivation was presented for the fields of radar and sonar [109, 111], and with slight modifications, it can be adapted to model the measurement uncertainty of Rayleigh-based sensors which rely on cross-correlation in the estimation of the frequency shift between two signals as shown in chapter 4.

Appendix A. Measurement frequency shift uncertainty derivation

The waveform that is transmitted and reflected back to be captured by the receiver can be simply written as follows:

$$y(x) = u(x - \tau_0) + n(x) \tag{A.1}$$

where $y(x)$ is the received signal, $n(x)$ is considered as a random Gaussian white noise voltage, and $u(x)$ is the original signal with no τ_0 which is the true delay/shift between the reference and the measurement signals. It should be noted that $u(x)$ is considered to be the reference signal which is already known and acquired before the measurement is conducted. Throughout the derivation τ_0 will denote the true value of the delay/shift and τ will represent all the values that τ_0 can take.

To achieve the goal of knowing the true value τ_0 given y, Bayes' theorem of inverse probability will be applied:

$$p_y(\tau) = \frac{p(\tau)p_\tau(y)}{p(y)} \tag{A.2}$$

where $p_y(\tau)$ is the posterior probability, $p(\tau)$ is the prior probability, $p_\tau(y)$ is the likelihood function, and $p(y)$ is the marginal likelihood function. Since $p(y)$ is independent of τ, it will be absorbed in k which is the normalising constant of the distribution that will be introduced in the following equation:

$$p_y(\tau) = k\, p(\tau)p_\tau(y) \tag{A.3}$$

It is important to explain Eq.(A.3) as neatly as possible so that its relevance to our current problem is clearly understood by the reader. We have already explained what each of the probabilities mean in probability theory, but what do they actually represent physically?

The essence of this whole problem lies in finding out the posterior probability $p_y(\tau)$ which is a distribution to explore the probability of attaining τ given the signal $y(x)$. This probability, as it is clear from Eq.(A.3), relies on the prior probability (which gives prior statistical information about the delay/shift), and the likelihood function (which should indicate the statistical properties of the noise in the system).

The prior probability $p(\tau)$ simply means that before conducting any measurement, we already have some prior knowledge about the delay/shift that the signal will experience. It is important to elaborate the previous statement with an example to have a better visualisation of the problem, and for this reason we will explain further with the help of the "Frequency-scanned φ-OTDR" interrogation system. When such a system is utilised for the experiment, the laser frequency is scanned over a preset frequency-scan range. This range is selected in such a way that it is at least 10-times larger than the amount of expected external perturbation so that the correlation window is large enough to yield accurate peak determination. This means that we kind of have an idea about the range of delay/shift which the signal might undergo, which is why we can assume that τ_0 must simply take any value within this predefined frequency

range. Consequently, the prior probability of τ is uniform over the scan range, since all values which τ can take are equally-probable.

As already mentioned earlier, the determination of the true value of τ is not as simple as it should be, and it is all because of the existence of the inevitable additive white Gaussian noise. This is where the likelihood function comes into play.

The likelihood function $p_\tau(y)$ can be simply be taken as a Gaussian distribution in y and can be formulated as:

$$p_\tau(y) = K \exp\left[-\frac{1}{2}\left(\frac{y(x) - u(x-\tau)}{N} \right)^2 \right] \tag{A.4}$$

where K is the normalising constant of the distribution, N is the mean squared value of the noise n. By substituting (A.4) into (A.3), the posterior distribution takes the form:

$$p_y(\tau) = k\, p(\tau) \exp\left[-\frac{1}{2}\left(\frac{y(x) - u(x-\tau)}{N} \right)^2 \right] \tag{A.5}$$

Eq.(A.5) can be extended more realistically by indicating that n is a random function that is formed over the range X (be it a time interval or a frequency range or just any arbitrary range) over which the signal voltage u is existing. Accordingly, the extended version of Eq.(A.5) is given by:

$$p_y(\tau) = k\, p(\tau) \exp\left(-\frac{1}{N} \int_0^X (y(x) - u(x-\tau))^2 dx \right) \tag{A.6}$$

By solving the quadratic equation and simplifying Eq.(A.6) (the term of $y(x)^2$ is absorbed in k, as it is independent of τ), Eq.(A.7) is yielded:

$$p_y(\tau) = k\, p(\tau) \exp\left(-\frac{1}{N} \int_0^X u^2(x-\tau) dx \right) \exp\left(\frac{2}{N} \int_0^X y(x) u(x-\tau) dx \right) \tag{A.7}$$

The term in the second exponential of Eq.(A.7) is of particular significance because it includes the multiplication $y(x)u(x-\tau)$ integrated over X. It should be noted that the use of X is for the generality of the problem, since it can alter according to the application. For instance, it can be a time interval T or a frequency range F or any arbitrary unit. The expression represents the cross-correlation function to measure the similarity between y and all the possible waveforms of u. As indicated earlier, $u(x)$ is the reference signal acquired before the experiment to be used for the similarity comparison with later acquired measurements. This term $u(x-\tau)$ simply means that $u(x)$ will be theoretically lagged to find out the value of τ which is the closest to τ_0. This shows that if all the message states τ are equally probable, and if all the corresponding signals $u(x-\tau)$ have equal energy, the message state with the highest probability of occurrence is the one which results in the maximum similarity, i.e., largest cross-correlation.

The rest of the expressions in Eq.(A.7) will not have any effect on the estimation, since they do not involve y. Accordingly, only the term of interest will be used further in the derivation, and

will be named as $q(\tau)$ presented by the following expression:

$$c(\tau) = \frac{2}{N} \int_0^X y(x) u(x - \tau) dx \qquad \text{(A.8)}$$

Correspondingly, the posterior probability will take the following form:

$$p_y(\tau) = k\, p(\tau) \exp(c(\tau)) \qquad \text{(A.9)}$$

Further in the derivation, the signal $c(\tau)$ will be divided into its signal $l(\tau)$ and noise $h(\tau)$ components, and their effect on $p_y(\tau)$ will be evaluated separately. Of course, this perspective is only applied for purely analytical purposes, since in reality the received signal cannot be split into its noise and signal components. It will be observed, however, that $l(\tau)$ alone is sufficient enough to determine the true value of τ as well as the accuracy of finding it.

In that case, $c(\tau)$ is written as:

$$c(\tau) = l(\tau) + h(\tau) \qquad \text{(A.10)}$$

where $l(\tau)$ and $h(\tau)$ are the signal and noise functions, respectively, and are expressed by the following equations:

$$l(\tau) = \frac{2}{N} \int_0^X u(x - \tau_0) u(x - \tau) dx \qquad \text{(A.11)}$$

$$h(\tau) = \frac{2}{N} \int_0^X n(x) u(x - \tau) dx \qquad \text{(A.12)}$$

The maximum value of $l(\tau)$ occurs at τ_0 and is given by:

$$l(\tau_0) = M_e = \frac{2E}{N} \qquad \text{(A.13)}$$

where M_e is the peak power electrical signal-to-noise ratio (SNR) with N as the mean squared value of the noise, and E as the integrated square, or total energy of the signal described as:

$$E = \int |u(x)|^2 dx = \int |U(f)|^2 df \qquad \text{(A.14)}$$

Using Taylor's series [I], $l(\tau)$ can be expanded about τ_0 as follows:

$$l(\tau) = l(\tau_0) + \frac{l'(\tau_0)}{1!}(\tau - \tau_0) + \frac{l''(\tau_0)}{2!}(\tau - \tau_0)^2 + \dots$$

$$l(\tau_0) = \frac{2E}{N} = M_e$$

$$l'(\tau_0) = \frac{2}{N}\int u(x)\frac{du(x)}{dx}dx = \frac{2}{N}(2\pi i)^2 \int f U(f)^2 df = 0$$

(A.15)

$$l''(\tau_0) = \frac{2}{N}\int u(x)\frac{d^2 u(x)}{dx}dx = \frac{2}{N}(2\pi i)^2 \int f^2 U(f)^2 df$$

$l'(\tau_0)$ and $l''(\tau_0)$ are solved using the differentiation property of the Fourier transform and the Parseval's theorem [II]. Using Eq.(A.14) in Eq.(A.15), $l''(\tau_0)$ can be expressed by this equation:

$$l''(\tau_0) = \frac{2}{N}(2\pi i)^2 E \int \frac{f^2 |U(f)|^2 df}{|U(f)|^2 df} = M_e (4\pi^2) \int \frac{f^2 |U(f)|^2 df}{|U(f)|^2 df}$$

(A.16)

where

$$\beta^2 = (4\pi^2)\frac{\int f^2 |U(f)|^2 df}{\int |U(f)|^2 df}$$

(A.17)

is the normalised second moment (variance) of $|U|^2$ about zero. Here $U(f)$ is the Fourier transform of $u(x)$.

Finally, $l(\tau)$ will take the following form:

$$l(\tau) = M_e(1 - \frac{1}{2}\beta^2(\tau - \tau_0)^2 + \dots)$$

(A.18)

The accuracy with which τ can be determined is measured by the width of the peak of $p_y(\tau)$, which occurs in the vicinity of τ_0.

Since $h(\tau)$ should be extremely small at $\tau = \tau_0$, an approximation can be made and the contribution of $l(\tau_0)$ alone will be considered, thereby varying the posterior distribution

---

[I]The higher order terms are negligible, thus will be dropped, since the values that τ can take are very close to τ_0, meaning that $\tau - \tau_0$ will become much smaller with higher exponents.

[II]

$$\int g(x)\frac{d^n}{dx^n}g(x)dx = (2\pi i)^n \int G(f) f G(f) df$$

where $G(f)$ is the Fourier transform of $g(x)$

Appendix A. Measurement frequency shift uncertainty derivation

to become:

$$p_y(\tau) = k\, p(\tau) \exp(l(\tau)) \tag{A.19}$$

Considering that $p(\tau)$ is slowly varying and can be taken as a constant, the posterior probability can be approximated as follows:

$$p_y(\tau) \propto \exp\left(-\frac{1}{2} M_e \beta^2 (\tau - \tau_0)^2\right) \tag{A.20}$$

The variance of the distribution is then given by:

$$\sigma_\tau^2 = \frac{1}{\beta^2 M_e} \tag{A.21}$$

Finally, the accuracy with which the true value of τ can be determined, is given by the standard deviation:

$$\sigma_\tau = \frac{1}{\beta\sqrt{M_e}} = \frac{1}{\beta M_o} \tag{A.22}$$

where the parameter β represents the standard deviation of the power density of the signal and M_o represents the SNR in the optical domain calculated using the optical power. It should be noted that the optical power of the signal is equivalent to the square root of the electrical power.

B List of publications

Journal articles

- **Malak Galal**, Li Zhang, Fan Yang, Shoufei Gao, Yingying Wang and Luc Thévenaz. "Brillouin Gain Measurement and Distributed Temperature Sensing in Gas-filled Hollow-core Anti-resonant Fibres." **(in preparation, with the plan to submit to Optica)**

- **Malak Galal**, Suneetha Sebastian, and Luc Thévenaz. "Enhanced Signal-associated Noise in a φ-OTDR System." IEEE Access (2022): 44974-44981.

- **Malak Galal**, Suneetha Sebastian, Zhisheng Yang, Li Zhang, Simon Zaslawski, and Luc Thévenaz. "On the Measurement Accuracy of Coherent Rayleigh-based Distributed Sensors." Optics Express (2021): 42538-42552.

- Li Zhang, Zhisheng Yang, Nachum Gorbatov, Roy Davidi,**Malak Galal**, Luc Thévenaz, and Moshe Tur. "Distributed and Dynamic Strain Sensing with High Spatial Resolution and Large Measurable Strain Range." Optics Letters (2020): 5020-5023.

Conference papers

- Oral presentation: **Malak Galal**, Li Zhang, Shoufei Gao, Yingying Wang, and Luc Thévenaz. "Distributed Temperature Sensing Using Gas-filled Conjoined-tube Anti-resonant Fiber." In International Conference on Optical Fiber Sensors, Optica, 2022.

- Poster Presentation: Yuting Yang, **Malak Galal**, Suneetha Sebastian, Li Zhang and Luc Thévenaz. "Analytical Prediction on the Final Noise in a φ-OTDR System." In International Conference on Optical Fiber Sensors, Optica, 2022.

- Poster presentation: **Malak Galal**, Li Zhang, Fan Yang, Suneetha Sebastian, Shoufei Gao, Yingying Wang, and Luc Thévenaz. "Spontaneous Brillouin Scattering in Gas-filled Anti-resonant Fibre." In Frontiers in Optics, pp. JTh5A-110. Optical Society of America, 2021.

- Oral presentation: **Malak Galal**, Suneetha Sebastian, Zhisheng Yang, and Luc Thévenaz. "Determination of the Measurement Accuracy of a Phase-sensitive OTDR." In Optical Sensors, pp. SM5A-5. Optical Society of America, 2021.

- Oral presentation: **Malak Galal**, Suneetha Sebastian, Li Zhang, and Luc Thévenaz. "Distributed Temperature Sensing Based on φ-OTDR Using Back-reflection-enhanced Fiber." In CLEO: Science and Innovations, pp. STu1A-3. Optical Society of America, 2021.

Bibliography

[1] K. C. Kao and G. A. Hockham, "Dielectric-fibre surface waveguides for optical fre-quencies", *Proceedings of the Institution of Electrical Engineers*, IET, vol. 113, 1966, pp. 1151–1158.

[2] M. Borner, Electro-optical transmission system utilizing lasers, US Patent 3,845,293, Oct. 1974.

[3] G. Keiser, Optical fiber communications. McGraw-Hill New York, 2000, vol. 2.

[4] T. G. Giallorenzi, J. A. Bucaro, A. Dandridge, G. H. Sigel, J. H. Cole, S. C. Rashleigh, and R. G. Priest, "Optical fiber sensor technology", "IEEE transactions on microwave theory and techniques", vol. 30, no. 4, 1982.

[5] Z. Zhan, M. Cantono, V. Kamalov, A. Mecozzi, R. Müller, S. Yin, and J. C. Castellanos, "Optical polarization–based seismic and water wave sensing on transoceanic cables", "Science", vol. 371, no. 6532, 2021.

[6] P. Roberts, F. Couny, H. Sabert, B. Mangan, D. Williams, L. Farr, M. Mason, A. Tomlinson, T. Birks, J. Knight, *et al.*, "Ultimate low loss of hollow-core photonic crystal fibres", "Optics express", vol. 13, no. 1, 2005.

[7] G. T. Jasion *et al.*, "0.174 dB/km hollow core double nested antiresonant nodeless fiber (DNANF)", *Optical Fiber Communication Conference*, Optica, 2022, Th4C.7.

[8] G. P. Agrawal, "Nonlinear fiber optics", *Nonlinear Science at the Dawn of the 21st Century*, Springer, 2000, pp. 195–211.

[9] B. Saleh and M. Teich, Fundamentals of Photonics, 3rd Edition. Feb. 2019.

[10] D. Fleisch, A student's guide to Maxwell's equations. Cambridge University Press, 2008.

[11] R. W. Boyd, Nonlinear optics. Academic press, 2020.

[12] J. Peatross and M. Ware, Physics of light and optics. Brigham Young University, Depart-ment of Physics Brigham, 2011.

[13] F. Gyger, "Brillouin scattering in gas-filled hollow-core fibres", PhD thesis, École poly-technique fédérale de Lausanne (EPFL), Lausanne, Feb. 2020.

[14] L. Thevenaz, Advanced fiber optics: concepts and technology. EPFL press, 2011.

Bibliography

[15] M. I. Mishchenko, "Far-field approximation in electromagnetic scattering", "Journal of Quantitative Spectroscopy and Radiative Transfer", vol. 100, no. 1-3, 2006.

[16] A. Masoudi and T. P. Newson, "Contributed review: distributed optical fibre dynamic strain sensing", "Review of scientific instruments", vol. 87, no. 1, 2016.

[17] A. Hartog, An Introduction to Distributed Optical Fibre Sensors. CRC Press, Apr. 2017.

[18] T. Parker, M. Farhadiroushan, V. Handerek, and e. A. Rogers, "Temperature and strain dependence of the power level and frequency of spontaneous Brillouin scattering in optical fibers", "Optics letters", vol. 22, no. 11, 1997.

[19] J. Dakin, D. Pratt, G. Bibby, and J. Ross, "Temperature distribution measurement using Raman ratio thermometry", *Fiber Optic and Laser Sensors III*, International Society for Optics and Photonics, vol. 566, 1986, pp. 249–256.

[20] D. A. Long, The Raman effect: a unified treatment of the theory of Raman scattering by molecules. Wiley, 2002.

[21] G. A. Brown, A. Hartog, *et al.*, "Optical fiber sensors in upstream oil & gas", "Journal of petroleum technology", vol. 54, no. 11, 2002.

[22] S. W. Tyler, J. S. Selker, M. B. Hausner, C. E. Hatch, T. Torgersen, C. E. Thodal, and S. G. Schladow, "Environmental temperature sensing using Raman spectra dts fiber-optic methods", "Water Resources Research", vol. 45, no. 4, 2009.

[23] J. M. López-Higuera, L. R. Cobo, A. Q. Incera, and A. Cobo, "Fiber optic sensors in structural health monitoring", "Journal of lightwave technology", vol. 29, no. 4, 2011.

[24] M. Cole, W. Loh, R. Laming, M. Zervas, and S. Barcelos, "Moving fibre/phase mask-scanning beam technique for enhanced flexibility in producing fibre gratings with a uniform phase mask", "Electronics Letters", vol. 31, no. 17, 1995.

[25] K. M. Davis, K. Miura, N. Sugimoto, and K. Hirao, "Writing waveguides in glass with a femtosecond laser", "Optics letters", vol. 21, no. 21, 1996.

[26] W. W. Morey, G. Meltz, and W. H. Glenn, "Fiber optic bragg grating sensors", *Fiber optic and laser sensors VII*, SpIE, vol. 1169, 1990, pp. 98–107.

[27] X. Zhang, Z. Wu, and B. Zhang, "Strain dependence of fiber bragg grating sensors at low temperature", "Optical Engineering", vol. 45, no. 5, 2006.

[28] M. Barnoski and S. Jensen, "Fiber waveguides: a novel technique for investigating attenuation characteristics", "Applied optics", vol. 15, no. 9, 1976.

[29] H. Kallmann, Thermodynamic properties of real gases for use in high pressure problems. National Technical Information Service, 1950.

[30] J. Sengers, M. Klein, and J. S. Gallagher, "Pressure-volume-temperature relationships of gases virial coefficients", NATIONAL BUREAU OF STANDARDS WASHINGTON DC HEAT DIV, Tech. Rep., 1971.

[31] B. Cowan, Topics in statistical mechanics. World Scientific, 2021.

[32] F. Schreiber, F. Zanini, and F. Roosen-Runge, "Virial expansion–a brief introduction", "available at: www. soft-matter. uni-tuebingen. de/teaching/Tutorial_Virial_Expansion. pdf (accessed 5 June 2018)", 2011.

[33] J. Dymond, K. Marsh, R. Wilhoit, *et al.*, Virial coefficients of pure gases and mixtures. Springer Landord-Bornstein, 2003, vol. 21.

[34] J. Huot and T. Bose, "Experimental determination of the dielectric virial coefficients of atomic gases as a function of temperature", "The Journal of chemical physics", vol. 95, no. 4, 1991.

[35] A. Michels, W. De Graaff, and C. Ten Seldam, "Virial coefficients of hydrogen and deuterium at temperatures between- 175° c and+ 150° c. conclusions from the second virial coefficient with regards to the intermolecular potential", "Physica", vol. 26, no. 6, 1960.

[36] G. Di Staso, "Hybrid discretizations of the boltzmann equation for the dilute gas flow regime", 2018.

[37] M. O. Vieitez, E.-J. van Duijn, W. Ubachs, B. Witschas, A. Meijer, A. De Wijn, N. Dam, and W. van de Water, "Coherent and spontaneous Rayleigh-Brillouin scattering in atomic and molecular gases and gas mixtures", "Physical Review A", vol. 82, no. 4, 2010.

[38] B. Witschas, M. O. Vieitez, E.-J. van Duijn, O. Reitebuch, W. van de Water, and W. Ubachs, "Spontaneous Rayleigh–Brillouin scattering of ultraviolet light in nitrogen, dry air, and moist air", "Applied optics", vol. 49, no. 22, 2010.

[39] W. Ubachs, E. van Duijn, M. Vieitez, W. Van de Water, N. Dam, J. Ter Meulen, A. Meijer, J. De Kloe, A. Stoffelen, and E. Aben, "A spontaneous Rayleigh-Brillouin scattering experiment for the characterization of atmospheric lidar backscatter", "ESA Contract Final Report", 2009.

[40] C. Boley, R. C. Desai, and G. Tenti, "Kinetic models and Brillouin scattering in a molecular gas", "Canadian Journal of Physics", vol. 50, no. 18, 1972.

[41] G. Tenti, C. Boley, and R. C. Desai, "On the kinetic model description of Rayleigh–Brillouin scattering from molecular gases", "Canadian Journal of Physics", vol. 52, no. 4, 1974.

[42] C. Yang, T. Wu, J. Shang, X. Zhang, R. Hu, and X. He, "The effect of pressure on spontaneous Rayleigh–Brillouin scattering spectrum in nitrogen", "Journal of Modern Optics", vol. 65, no. 8, 2018.

[43] A. Bucholtz, "Rayleigh-scattering calculations for the terrestrial atmosphere", "Applied Optics", vol. 34, no. 15, 1995.

[44] H. Kragh, "The lorenz-lorentz formula: origin and early history", "Substantia", vol. 2, no. 2, 2018.

[45] B. J. Berne and R. Pecora, Dynamic light scattering: with applications to chemistry, biology, and physics. Courier Corporation, 2000.

[46] Z. Gu and W. Ubachs, "Temperature-dependent bulk viscosity of nitrogen gas determined from spontaneous rayleigh–Brillouin scattering", "Optics letters", vol. 38, no. 7, 2013.

[47] B. Sharma and R. Kumar, "Estimation of bulk viscosity of dilute gases using a nonequilibrium molecular dynamics approach", "Phys. Rev. E", vol. 100, 1 2019.

[48] F. Yang, F. Gyger, and L. Thévenaz, "Intense Brillouin amplification in gas using hollow-core waveguides", "Nature photonics", vol. 14, no. 11, 2020.

[49] J. Pastor-Graells, H. F. Martins, A. Garcia-Ruiz, S. Martin-Lopez, and M. Gonzalez-Herraez, "Single-shot distributed temperature and strain tracking using direct detection phase-sensitive otdr with chirped pulses", "Optics express", vol. 24, no. 12, 2016.

[50] Y. Mizuno, W. Zou, Z. He, and K. Hotate, "Proposal of Brillouin optical correlation-domain reflectometry (BOCDR)", "Optics express", vol. 16, no. 16, 2008.

[51] O. Matsuoka, M. Kishi, and K. Hotate, "Brillouin optical correlation domain reflectometry with double frequency modulation and phase modulation", *23rd International Conference on Optical Fibre Sensors*, International Society for Optics and Photonics, vol. 9157, 2014, 91576G.

[52] R. Cohen, Y. London, Y. Antman, and A. Zadok, "Brillouin optical correlation domain analysis with 4 millimeter resolution based on amplified spontaneous emission", "Optics express", vol. 22, no. 10, 2014.

[53] Y. Mizuno, H. Lee, and K. Nakamura, "Recent advances in Brillouin optical correlation-domain reflectometry", "Applied Sciences", vol. 8, no. 10, 2018.

[54] K. Hotate, "Recent achievements in BOCDA/BOCDR", *SENSORS, 2014 IEEE*, IEEE, 2014, pp. 142–145.

[55] Y. Mizuno, Z. He, and K. Hotate, "Measurement range enlargement in Brillouin optical correlation-domain reflectometry based on temporal gating scheme", "Optics Express", vol. 17, no. 11, 2009.

[56] L. Thévenaz, "Next generation of optical fibre sensors: new concepts and perspectives", *23rd International Conference on Optical Fibre Sensors*, International Society for Optics and Photonics, vol. 9157, 2014.

[57] A. Beisenova, A. Issatayeva, S. Korganbayev, C. Molardi, W. Blanc, and D. Tosi, "Simultaneous distributed sensing on multiple mgo-doped high scattering fibers by means of scattering-level multiplexing", "Journal of Lightwave Technology", vol. 37, no. 13, 2019.

[58] S. Loranger, M. Gagné, V. Lambin-Iezzi, and R. Kashyap, "Rayleigh scatter based order of magnitude increase in distributed temperature and strain sensing by simple uv exposure of optical fibre", "Scientific reports", vol. 5, 2015.

[59] F. Monet, S. Loranger, V. Lambin-Iezzi, A. Drouin, S. Kadoury, and R. Kashyap, "The rogue: a novel, noise-generated random grating", "Optics express", vol. 27, no. 10, 2019.

[60] M. Gagné, S. Loranger, J. Lapointe, and R. Kashyap, "Fabrication of high quality, ultra-long fiber bragg gratings: up to 2 million periods in phase", "Optics express", vol. 22, no. 1, 2014.

[61] L. Thévenaz, S. Chin, J. Sancho, and S. Sales, "Novel technique for distributed fibre sensing based on faint long gratings (flogs)", *23rd International Conference on Optical Fibre Sensors*, International Society for Optics and Photonics, vol. 9157, 2014, 91576W.

[62] R. Kashyap, Fiber bragg gratings. Academic press, 2009.

[63] W.-P. Huang, "Coupled-mode theory for optical waveguides: an overview", "J. Opt. Soc. Am. A", vol. 11, no. 3, 1994.

[64] A. Yariv, "Coupled-mode theory for guided-wave optics", "IEEE Journal of Quantum Electronics", vol. 9, no. 9, 1973.

[65] H. F. Taylor and A. Yariv, "Guided wave optics", "Proceedings of the IEEE", vol. 62, no. 8, 1974.

[66] A. Yariv and M. Nakamura, "Periodic structures for integrated optics", "IEEE journal of quantum electronics", vol. 13, no. 4, 1977.

[67] J.-C. Beugnot, M. Tur, S. F. Mafang, and L. Thévenaz, "Distributed Brillouin sensing with sub-meter spatial resolution: modeling and processing", "Optics express", vol. 19, no. 8, 2011.

[68] C. Runge, "Über die numerische auflösung von differentialgleichungen", "Mathematische Annalen", vol. 46, no. 2, 1895.

[69] E. Süli and D. F. Mayers, An introduction to numerical analysis. Cambridge university press, 2003.

[70] O. Shapira and B. Fischer, "Localization of light in a random-grating array in a single-mode fiber", "JOSA B", vol. 22, no. 12, 2005.

[71] J. D. Hart, C. R. Williams, and G. A. Cranch, "Range limitations of optical frequency domain reflectometry with all-grating fiber for distributed strain and temperature sensing", "Optics Express", vol. 29, no. 26, 2021.

[72] Y. Lai, K. Zhou, K. Sugden, and I. Bennion, "Point-by-point inscription of first-order fiber bragg grating for c-band applications", "Optics express", vol. 15, no. 26, 2007.

[73] P. S. Westbrook, K. S. Feder, R. M. Ortiz, T. Kremp, E. M. Monberg, H. Wu, D. A. Simoff, and S. Shenk, "Kilometer length, low loss enhanced back scattering fiber for distributed sensing", *2017 25th Optical Fiber Sensors Conference (OFS)*, IEEE, 2017, pp. 1–5.

[74] P. S. Westbrook, T. Kremp, K. S. Feder, W. Ko, E. M. Monberg, H. Wu, D. A. Simoff, and R. M. Ortiz, "Improving distributed sensing with continuous gratings in single and multi-core fibers", *Optical Fiber Communication Conference*, Optical Society of America, 2018, W1K.1. [Online]. Available: http://www.osapublishing.org/abstract.cfm?URI=OFC-2018-W1K.1.

[75] Acoustisens optical sensor fiber, ITU-T G.652.D, Rev. D, OFS Optics, 2019. [Online]. Available: https://fiber-optic-catalog.ofsoptics.com/documents/pdf/AcoustiSens-web.pdf.

[76] L. Thévenaz and M. Soto, "The making of a good Brillouin distributed fiber sensor", *Fiber-Based Technologies and Applications*, Optical Society of America, 2014, FTh4D–1.

[77] G. Milione, P. N. Ji, E. Ip, and T. Wang, Method to increase the signal to noise ratio of distributed acoustic sensing by spatial averaging, US Patent 10,345,138, Jul. 2019.

[78] W. Chen, J. Jiang, K. Liu, S. Wang, Z. Ma, Z. Ding, T. Xu, and T. Liu, "Coherent OTDR using flexible all-digital orthogonal phase code pulse for distributed sensing", "IEEE Access", vol. 8, 2020.

[79] Z. Wang, B. Zhang, J. Xiong, Y. Fu, S. Lin, J. Jiang, Y. Chen, Y. Wu, Q. Meng, and Y. Rao, "Distributed acoustic sensing based on pulse-coding phase-sensitive OTDR", "IEEE Internet of Things Journal", vol. 6, no. 4, 2018.

[80] Z. Wang, J. Zeng, J. Li, M. Fan, H. Wu, F. Peng, L. Zhang, Y. Zhou, and Y. Rao, "Ultra-long phase-sensitive OTDR with hybrid distributed amplification", "Optics letters", vol. 39, no. 20, 2014.

[81] H. F. Martins, S. Martin-Lopez, P. Corredera, J. D. Ania-Castañon, O. Frazão, and M. Gonzalez-Herraez, "Distributed vibration sensing over 125 km with enhanced SNR using phi-OTDR over a URFL cavity", "Journal of Lightwave Technology", vol. 33, no. 12, 2015. [Online]. Available: http://opg.optica.org/jlt/abstract.cfm?URI=jlt-33-12-2628.

[82] T. Zhu, X. Xiao, Q. He, and D. Diao, "Enhancement of SNR and spatial resolution in φ-OTDR system by using two-dimensional edge detection method", "Journal of Lightwave Technology", vol. 31, no. 17, 2013.

[83] H. He, L. Shao, H. Li, W. Pan, B. Luo, X. Zou, and L. Yan, "SNR enhancement in phase-sensitive OTDR with adaptive 2-d bilateral filtering algorithm", "IEEE Photonics Journal", vol. 9, no. 3, 2017.

[84] Y. Xu, P. Lu, S. Gao, D. Xiang, S. Mihailov, and X. Bao, "Optical fiber random grating-based multiparameter sensor", "Optics letters", vol. 40, no. 23, 2015.

[85] P. S. Westbrook, T. Kremp, K. S. Feder, W. Ko, E. M. Monberg, H. Wu, D. A. Simoff, T. F. Taunay, and R. M. Ortiz, "Continuous multicore optical fiber grating arrays for distributed sensing applications", "Journal of Lightwave Technology", vol. 35, no. 6, 2017.

[86] A. Beisenova, A. Issatayeva, S. Sovetov, S. Korganbayev, M. Jelbuldina, Z. Ashikbayeva, W. Blanc, E. Schena, S. Sales, C. Molardi, and D. Tosi, "Multi-fiber distributed thermal profiling of minimally invasive thermal ablation with scattering-level multiplexing in mgo-doped fibers", "Biomedical optics express", vol. 10, no. 3, 2019.

[87] L. Zhang, L. D. Costa, Z. Yang, M. A. Soto, M. Gonzalez-Herráez, and L. Thévenaz, "Analysis and reduction of large errors in Rayleigh-based distributed sensor", "Journal of Lightwave Technology", vol. 37, no. 18, 2019.

[88] J. Pastor-Graells, L. R. Cortés, M. R. Fernández-Ruiz, H. F. Martins, J. Azaña, S. Martin-Lopez, and M. Gonzalez-Herraez, "SNR enhancement in high-resolution phase-sensitive OTDR systems using chirped pulse amplification concepts", "Opt. Lett.", vol. 42, no. 9, May 2017. [Online]. Available: http://ol.osa.org/abstract.cfm?URI=ol-42-9-1728.

[89] M. A. Soto and L. Thévenaz, "Modeling and evaluating the performance of Brillouin distributed optical fiber sensors", "Optics express", vol. 21, no. 25, 2013.

[90] L. Zhou, F. Wang, X. Wang, Y. Pan, Z. Sun, J. Hua, and X. Zhang, "Distributed strain and vibration sensing system based on phase-sensitive OTDR", "IEEE Photonics Technology Letters", vol. 27, no. 17, 2015.

[91] D. Wang, J. Zou, Y. Wang, B. Jin, Q. Bai, X. Liu, and Y. Liu, "Distributed optical fiber low-frequency vibration detecting using cross-correlation spectrum analysis", "Journal of Lightwave Technology", vol. 38, no. 23, 2020.

[92] K. Markiewicz, J. Kaczorowski, Z. Yang, L. Szostkiewicz, A. Dominguez-Lopez, K. Wilczynski, M. Napierala, T. Nasilowski, and L. Thévenaz, "Frequency scanned phase sensitive optical time-domain reflectometry interrogation in multimode optical fibers", "APL Photonics", vol. 5, no. 3, 2020.

[93] C. Knapp and G. Carter, "The generalized correlation method for estimation of time delay", "IEEE Transactions on Acoustics, Speech, and Signal Processing", vol. 24, no. 4, 1976.

[94] M. Azaria and D. Hertz, "Time delay estimation by generalized cross correlation methods", "IEEE Transactions on Acoustics, Speech, and Signal Processing", vol. 32, no. 2, 1984.

[95] G. Carter, "Time delay estimation for passive sonar signal processing", "IEEE Transactions on Acoustics, Speech, and Signal Processing", vol. 29, no. 3, 1981.

[96] M. Froggatt and J. Moore, "High-spatial-resolution distributed strain measurement in optical fiber with Rayleigh scatter", "Applied optics", vol. 37, no. 10, 1998.

[97] M. Galal, S. Sebastian, Z. Yang, L. Zhang, S. Zaslawski, and L. Thévenaz, "On the measurement accuracy of coherent rayleigh-based distributed sensors", "Optics Express", vol. 29, no. 26, 2021.

[98] Y. Koyamada, M. Imahama, K. Kubota, and K. Hogari, "Fiber-optic distributed strain and temperature sensing with very high measurand resolution over long range using coherent OTDR", "Journal of Lightwave Technology", vol. 27, no. 9, 2009. [Online]. Available: http://opg.optica.org/jlt/abstract.cfm?URI=jlt-27-9-1142.

[99] X. Lu, M. A. Soto, and L. Thévenaz, "Optimal detection bandwidth for phase-sensitive optical time-domain reflectometry", *Sixth European Workshop on Optical Fibre Sensors*, International Society for Optics and Photonics, vol. 9916, 2016, 99162N.

[100] H. Gabai and A. Eyal, "On the sensitivity of distributed acoustic sensing", "Optics letters", vol. 41, no. 24, 2016.

[101] J. W. Goodman, Statistical optics. John Wiley & Sons, 2015.

[102] P. Healey, "Statistics of Rayleigh backscatter from a single-mode fiber", "IEEE transactions on communications", vol. 35, no. 2, 1987.

[103] A. Masoudi and T. P. Newson, "Analysis of distributed optical fibre acoustic sensors through numerical modelling", "Optics express", vol. 25, no. 25, 2017.

[104] A. Alekseev, V. Vdovenko, B. Gorshkov, V. Potapov, and D. Simikin, "A phase-sensitive optical time-domain reflectometer with dual-pulse diverse frequency probe signal", "Laser Physics", vol. 25, no. 6, 2015.

[105] P. Gysel and R. K. Staubli, "Spectral properties of Rayleigh backscattered light from single-mode fibers caused by a modulated probe signal", "Journal of lightwave technology", vol. 8, no. 12, 1990.

[106] J. Rothstein, Probability and information theory, with applications to radar. PM Woodward. McGraw-Hill, New York; Pergamon Press, London, 1953. 128 pp. Illus. 4.50, 1954.

[107] A. Quazi, "An overview on the time delay estimate in active and passive systems for target localization", "IEEE Transactions on Acoustics, Speech, and Signal Processing", vol. 29, no. 3, 1981.

[108] C. W. Helstrom, Statistical theory of signal detection: international series of monographs in electronics and instrumentation. Elsevier, 2013, vol. 9, pp. 274–278.

[109] P. M. Woodward, Probability and information theory: with applications to radar. Pergamon, 1953, pp. 100–105.

[110] I. Cespedes, J. Ophir, and S. K. Alam, "The combined effect of signal decorrelation and random noise on the variance of time delay estimation", "IEEE transactions on ultrasonics, ferroelectrics, and frequency control", vol. 44, no. 1, 1997.

[111] P. Woodward, "Theory of radar information", "Transactions of the IRE Professional Group on Information Theory", vol. 1, no. 1, 1953.

[112] X. Lu, M. A. Soto, L. Zhang, and L. Thévenaz, "Spectral properties of the signal in phase-sensitive optical time-domain reflectometry with direct detection", "Journal of Lightwave Technology", vol. 38, no. 6, 2020. [Online]. Available: http://opg.optica.org/jlt/abstract.cfm?URI=jlt-38-6-1513.

[113] L. Costa, H. F. Martins, S. Martın-López, M. R. Fernández-Ruiz, and M. González-Herráez, "Fully distributed optical fiber strain sensor with 10^{-12} $\epsilon/\sqrt{Hz}$ sensitivity", "Journal of Lightwave Technology", vol. 37, no. 18, 2019.

[114] L. Zhang, Z. Yang, N. Gorbatov, R. Davidi, M. Galal, L. Thévenaz, and M. Tur, "Distributed and dynamic strain sensing with high spatial resolution and large measurable strain range", "Optics Letters", vol. 45, no. 18, 2020.

[115] M. Galal, S. Sebastian, and L. Thévenaz, "Enhanced signal-associated noise in a φ-OTDR system", "IEEE Access", vol. 10, 2022.

[116] X. Lu and K. Krebber, "Characterizing detection noise in phase-sensitive optical time domain reflectometry", "Optics Express", vol. 29, no. 12, 2021.

[117] X. Angulo-Vinuesa, A. Dominguez-Lopez, A. Lopez-Gil, J. D. Ania-Castañón, S. Martin-Lopez, and M. Gonzalez-Herraez, "Limits of BOTDA range extension techniques", "IEEE Sensors Journal", vol. 16, no. 10, 2015.

[118] S. Wang, Z. Yang, M. A. Soto, and L. Thévenaz, "Study on the signal-to-noise ratio of Brillouin optical-time domain analyzers", "Optics Express", vol. 28, no. 14, 2020.

[119] M. Alem, M. A. Soto, and L. Thévenaz, "Analytical model and experimental verification of the critical power for modulation instability in optical fibers", "Optics express", vol. 23, no. 23, 2015.

[120] L. Zhang, L. D. Costa, Z. Yang, M. A. Soto, M. González-Herráez, and L. Thévenaz, "Analysis and reduction of large errors in Rayleigh-based distributed sensor", "Journal of Lightwave Technology", vol. 37, no. 18, 2019.

[121] M. Galal, S. Sebastian, L. Zhang, and L. Thévenaz, "Distributed temperature sensing based on φ-OTDR using back-reflection-enhanced fiber", *CLEO: Science and Innovations*, Optical Society of America, 2021, STu1A–3.

[122] F. Benabid, J. C. Knight, G. Antonopoulos, and P. S. J. Russell, "Stimulated Raman scattering in hydrogen-filled hollow-core photonic crystal fiber", "Science", vol. 298, no. 5592, 2002.

[123] F. Yang, F. Gyger, A. Godet, J. Chrétien, L. Zhang, M. Pang, J.-C. Beugnot, and L. Thévenaz, "Large evanescently-induced Brillouin scattering at the surrounding of a nanofibre", "Nature Communications", vol. 13, no. 1, 2022.

[124] V. Michaud-Belleau, E. N. Fokoua, T. Bradley, J. R. Hayes, Y. Chen, F. Poletti, D. J. Richardson, J. Genest, and R. Slavık, "Backscattering in antiresonant hollow-core fibers: over 40 db lower than in standard optical fibers", "Optica", vol. 8, no. 2, 2021.

[125] W. Ding, Y.-Y. Wang, S.-F. Gao, M.-L. Wang, and P. Wang, "Recent progress in low-loss hollow-core anti-resonant fibers and their applications", "IEEE Journal of Selected Topics in Quantum Electronics", vol. 26, no. 4, 2019.

[126] P. Russell, "Photonic crystal fibers", "Science", vol. 299, no. 5605, 2003.

[127] A. M. Cubillas, J. Hald, and J. C. Petersen, "High resolution spectroscopy of ammonia in a hollow-core fiber", "Optics express", vol. 16, no. 6, 2008.

[128] P. Ghenuche, S. Rammler, N. Y. Joly, M. Scharrer, M. Frosz, J. Wenger, P. S. J. Russell, and H. Rigneault, "Kagome hollow-core photonic crystal fiber probe for Raman spectroscopy", "Optics letters", vol. 37, no. 21, 2012.

[129] A. M. Cubillas, S. Unterkofler, T. G. Euser, B. J. Etzold, A. C. Jones, P. J. Sadler, P. Wasserscheid, and P. S. J. Russell, "Photonic crystal fibres for chemical sensing and photochemistry", "Chemical Society Reviews", vol. 42, no. 22, 2013.

[130] T. Ritari, J. Tuominen, H. Ludvigsen, J. Petersen, T. Sørensen, T. P. Hansen, and H. R. Simonsen, "Gas sensing using air-guiding photonic bandgap fibers", "Optics Express", vol. 12, no. 17, 2004.

Bibliography

[131] A. Cubillas, M. Silva-Lopez, J. Lazaro, O. Conde, M. Petrovich, and J. Lopez-Higuera, "Methane detection at 1670-nm band using a hollow-core photonic bandgap fiber and a multiline algorithm", "Optics Express", vol. 15, no. 26, 2007.

[132] G. Pearce, G. Wiederhecker, C. G. Poulton, S. Burger, and P. S. J. Russell, "Models for guidance in kagome-structured hollow-core photonic crystal fibres", "Optics express", vol. 15, no. 20, 2007.

[133] F. Gérôme, R. Jamier, J.-L. Auguste, G. Humbert, and J.-M. Blondy, "Simplified hollow-core photonic crystal fiber", "Optics letters", vol. 35, no. 8, 2010.

[134] S. Février, B. Beaudou, and P. Viale, "Understanding origin of loss in large pitch hollow-core photonic crystal fibers and their design simplification", "Optics Express", vol. 18, no. 5, 2010.

[135] M. Duguay, Y. Kokubun, T. L. Koch, and L. Pfeiffer, "Antiresonant reflecting optical waveguides in SiO_2-Si multilayer structures", "Applied Physics Letters", vol. 49, no. 1, 1986.

[136] J.-L. Archambault, R. J. Black, S. Lacroix, and J. Bures, "Loss calculations for antiresonant waveguides", "Journal of Lightwave Technology", vol. 11, no. 3, 1993.

[137] N. N. Edavalath, "Design and fabrication of effectively single mode hollow-core single-ring photonic crystal fibres", PhD thesis, Friedrich-Alexander-Universität Erlangen-Nürnberg (FAU), 2018.

[138] N. Litchinitser, A. Abeeluck, C. Headley, and B. Eggleton, "Antiresonant reflecting photonic crystal optical waveguides", "Optics letters", vol. 27, no. 18, 2002.

[139] Hollow-core bandgap photonic-crystal fiber, HC-1550-02, NKT Photonics, 2019. [Online]. Available: https://www.nktphotonics.com/products/optical-fibers-and-modules/hollow-core-photonic-crystal-fibers/.

[140] S.-F. Gao, Y.-Y. Wang, X.-L. Liu, W. Ding, and P. Wang, "Bending loss characterization in nodeless hollow-core anti-resonant fiber", "Optics express", vol. 24, no. 13, 2016.

[141] S.-f. Gao, Y.-y. Wang, W. Ding, D.-l. Jiang, S. Gu, X. Zhang, and P. Wang, "Hollow-core conjoined-tube negative-curvature fibre with ultralow loss", "Nature communications", vol. 9, no. 1, 2018.

[142] F. Yang, W. Jin, Y. Cao, H. L. Ho, and Y. Wang, "Towards high sensitivity gas detection with hollow-core photonic bandgap fibers", "Optics Express", vol. 22, no. 20, 2014.

[143] F. Poletti, "Nested antiresonant nodeless hollow core fiber", "Optics express", vol. 22, no. 20, 2014.

[144] M. Petrovich, F. Poletti, A. Van Brakel, and D. Richardson, "Robustly single mode hollow core photonic bandgap fiber", "Optics Express", vol. 16, no. 6, 2008.

[145] J. M. Fini, J. W. Nicholson, R. S. Windeler, E. M. Monberg, L. Meng, B. Mangan, A. DeSantolo, and F. V. DiMarcello, "Low-loss hollow-core fibers with improved single-modedness", "Optics express", vol. 21, no. 5, 2013.

[146] V. A. Sleiffer, Y. Jung, N. K. Baddela, J. Surof, M. Kuschnerov, V. Veljanovski, J. R. Hayes, N. V. Wheeler, E. R. N. Fokoua, J. P. Wooler, *et al.*, "High capacity mode-division multiplexed optical transmission in a novel 37-cell hollow-core photonic bandgap fiber", "Journal of lightwave technology", vol. 32, no. 4, 2013.

[147] E. A. Marcatili and R. Schmeltzer, "Hollow metallic and dielectric waveguides for long distance optical transmission and lasers", "Bell System Technical Journal", vol. 43, no. 4, 1964.

[148] P. Uebel, M. C. Günendi, M. H. Frosz, G. Ahmed, N. N. Edavalath, J.-M. Ménard, and P. S. J. Russell, "Broadband robustly single-mode hollow-core pcf by resonant filtering of higher-order modes", "Optics letters", vol. 41, no. 9, 2016.

[149] M. Koshiba and K. Saitoh, "Structural dependence of effective area and mode field diameter for holey fibers", "Optics Express", vol. 11, no. 15, 2003.

[150] A. Kobyakov, M. Sauer, and D. Chowdhury, "Stimulated Brillouin scattering in optical fibers", "Advances in Optics and Photonics", vol. 2, no. 1, 2010.

[151] Y. Zhao, Y. Qi, H. L. Ho, S. Gao, Y. Wang, and W. Jin, "Photoacoustic Brillouin spectroscopy of gas-filled anti-resonant hollow-core optical fibers", "Optica", vol. 8, no. 4, 2021.

[152] O. Sergeev, A. Shashkov, and A. Umanskii, "Thermophysical properties of quartz glass", "Journal of engineering physics", vol. 43, no. 6, 1982.

[153] F. Benabid, F. Couny, J. Knight, T. Birks, and P. S. J. Russell, "Compact, stable and efficient all-fibre gas cells using hollow-core photonic crystal fibres", "Nature", vol. 434, no. 7032, 2005.

[154] M. Komanec, D. Suslov, S. Zvanovec, Y. Chen, T. Bradley, S. R. Sandoghchi, E. N. Fokoua, G. Jasion, M. Petrovich, F. Poletti, *et al.*, "Low-loss and low-back-reflection hollow-core to standard fiber interconnection", "IEEE Photonics Technology Letters", vol. 31, no. 10, 2019.

[155] D. Suslov, M. Komanec, E. R. Numkam Fokoua, D. Dousek, A. Zhong, S. Zvánovec, T. D. Bradley, F. Poletti, D. J. Richardson, and R. Slavík, "Low loss and high performance interconnection between standard single-mode fiber and antiresonant hollow-core fiber", "Scientific Reports", vol. 11, no. 1, 2021.

[156] A. I. Adamu, Y. Wang, R. A. Correa, O. Bang, and C. Markos, "Low-loss micro-machining of anti-resonant hollow-core fiber with focused ion beam for optofluidic application", "Optical Materials Express", vol. 11, no. 2, 2021.

[157] Y. Lin, W. Jin, F. Yang, Y. Tan, and H. L. Ho, "Performance optimization of hollow-core fiber photothermal gas sensors", "Optics Letters", vol. 42, no. 22, 2017.

[158] F. Chen, S. Jiang, W. Jin, H. Bao, H. L. Ho, C. Wang, and S. Gao, "Ethane detection with mid-infrared hollow-core fiber photothermal spectroscopy", "Optics Express", vol. 28, no. 25, 2020.

Bibliography

[159]   F. Couny, F. Benabid, and P. Light, "Reduction of fresnel back-reflection at splice interface between hollow core pcf and single-mode fiber", "IEEE Photonics Technology Letters", vol. 19, no. 13, 2007.

[160]   J. H. Chong and M. Rao, "Development of a system for laser splicing photonic crystal fiber", "Optics Express", vol. 11, no. 12, 2003.

[161]   L. Xiao, M. Demokan, W. Jin, Y. Wang, and C.-L. Zhao, "Fusion splicing photonic crystal fibers and conventional single-mode fibers: microhole collapse effect", "Journal of lightwave technology", vol. 25, no. 11, 2007. [Online]. Available: http://opg.optica.org/jlt/abstract.cfm?URI=jlt-25-11-3563.

[162]   J. Henningsen and J. Hald, "Dynamics of gas flow in hollow core photonic bandgap fibers", "Applied Optics", vol. 47, no. 15, 2008.

[163]   R. Wynne and B. Barabadi, "Gas-filling dynamics of a hollow-core photonic bandgap fiber for nonvacuum conditions", "Applied Optics", vol. 54, no. 7, 2015.

[164]   R. W. Boyd, K. Rzążewski, and P. Narum, "Noise initiation of stimulated Brillouin scattering", "Physical Review A", vol. 42, 9 Nov. 1990.

[165]   S. Le Floch and P. Cambon, "Theoretical evaluation of the Brillouin threshold and the steady-state Brillouin equations in standard single-mode optical fibers", "JOSA A", vol. 20, no. 6, 2003.

[166]   W. M. Haynes, D. R. Lide, and T. J. Bruno, CRC handbook of chemistry and physics. CRC press, 2016.

[167]   A. Michels and R. Gibson, "The measurement of the viscosity of gases at high pressures.—the viscosity of nitrogen to 1000 atms", "Proceedings of the Royal Society of London. Series A, Containing Papers of a Mathematical and Physical Character", vol. 134, no. 823, 1931.

[168]   G. Prangsma, A. Alberga, and J. Beenakker, "Ultrasonic determination of the volume viscosity of n2, co, ch4 and cd4 between 77 and 300 k", "Physica", vol. 64, no. 2, 1973.

[169]   A. F. Estrada-Alexanders, O. Guzmán, and B. Pérez-Vidal, "High-precision virial coefficients of argon and carbon dioxide from integration of speed of sound data in the pressure–temperature domain", "Molecular Physics", vol. 110, no. 11-12, 2012.

[170]   X. Pan, M. N. Shneider, and R. B. Miles, "Power spectrum of coherent rayleigh-brillouin scattering in carbon dioxide", "Physical Review A", vol. 71, no. 4, 2005.

[171]   Z. Gu, W. Ubachs, and W. van de Water, "Rayleigh–brillouin scattering of carbon dioxide", "Optics Letters", vol. 39, no. 11, 2014.

[172]   Y. Wang, W. Ubachs, and W. Van De Water, "Bulk viscosity of co2 from rayleigh-brillouin light scattering spectroscopy at 532 nm", "The Journal of Chemical Physics", vol. 150, no. 15, 2019.

[173]   G. Emanuel, "Bulk viscosity of a dilute polyatomic gas", "Physics of Fluids A: Fluid Dynamics", vol. 2, no. 12, 1990.

Malak Galal

@ malak.galal@epfl.ch   ☎ +41 78 266 77 73   in linkedin.com/in/malak-galal-5545625a

@ m.galal93@gmail.com   📍 1007 Lausanne, Switzerland

Education

September 2012 - July 2017
Bachelor of Science in Electronics Engineering
German University in Cairo (GUC), Egypt
GPA (German System): 1.79

Bachelor Thesis
 IMS Chips, Stuttgart, Germany
"Numerical Modeling of Normally-Off GaN High Electron Mobility Transistors Using a Trenched Gate"

June 2012
German Abitur
Deutsche Schule der Borromäerinnen in Kairo
GPA (German System): 1.7

Computer Skills

Strong knowledge: Matlab, LabVIEW, Silvaco, Comsol Multiphysics, Cadence Virtuoso, PSpice

Good knowledge: ADS, Xilinx ISE, L-Edit, C++, Java, Python

Language Skills

Arabic: Mother Tongue
English: Fluent (Written and Spoken)
German: Fluent (Written and Spoken)
French: Very good (Written and Spoken)

Extracurricular Activities

2021-2022:

- PhD students' representative in the doctoral school and the faculty council
- Laboratory safety delegate

2019-2020: PhD students' representative in Marie Sklodowska-Curie Actions (ITN-FINESSE)
Winter 2015: Scriptwriter in the physics team at the student organization Nawwar
Community Work: Assistant in the camp "Stiftung Feriengestaltung für Kinder Schweiz" in Switzerland
Sports: Tennis, basketball, running

Professional Experience

July 2018 - Present
Doctoral Assistant at the Group for Fibre Optics
École Polytechnique Fédérale de Lausanne (EPFL), Switzerland

- Developed and experimentally corroborated a theoretical model for the measurement accuracy of Rayleigh-based distributed fibre sensors.
- Demonstrated the use of specialty fibres to serve distributed fibre sensing (Reflection-enhanced fibres and hollow-core fibres).
- Implemented experimental interrogation setups based on Rayleigh and Brillouin scatterings, and dealt with RF devices as well as optical equipment.
- Member of the organising committee of the 26th international conference on Optical Fibre Sensors (OFS-26).
- Teaching assistant in several courses (e.g. Introduction to Photonics.)

March – August 2016
Research Assistant at IMS Chips
Universität Stuttgart, Germany

Investigated a novel concept using a trenched gate to achieve the normally-off operation of aluminum gallium nitride/gallium nitride (AlGaN/GaN) high-electron-mobility transistors (HEMTs) by conducting numerical simulations using Silvaco.

Selected Publications

M. Galal et al. "On the measurement accuracy of coherent Rayleigh-based distributed sensors." Optics Express 29.26 (2021): 42538-42552.

M. Galal et al. "Spontaneous Brillouin Scattering in Gas-filled Anti-resonant Fibre." Frontiers in Optics. Optical Society of America, 2021.

Honors and Awards

December 2021: Best 180s-flash-presentation award (EPFL)
2018-2020: Merit-based scholarship from Marie Sklodowska-Curie Actions (ITN-FINESSE) for PhD at EPFL
November 2016: Best poster award nomination
2012-2017: Merit-based scholarship for B.Sc. at GUC